The Coyote - an Advanced Pilot Training Aircraft

AIAA Graduate Team Aircraft Competition 2017-2018

May 2018

LIÈGE université

The Beep Beep Hunting Club

	AIAA number	Signature
Raphaël Dubois	918763	
Thibault Laurent	919210	
Bao Long Le Van	908407	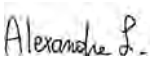
Nayan Levaux	908300	
Guillaume Noiset	908299	
Axel Piret	908234	
Arthur Scheffer	919169	
Vincent Schmitz	908516	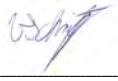

Team Advisors

Grigorios Dimitriadis

Ludovic Noels

Contents

List of Figures

List of Tables

Nomenclature

The variables used in this report are listed and briefly described here below. For the sake of conciseness, they will not be defined again when they first appear in the report.

Abbreviations

$MTOW$	Maximum take-off weight	[lb] or [kg]
$mTOW$	Minimum take-off weight	[lb] or [kg]
ZFW	Zero fuel weight	[lb] or [kg]
A.o.A.	Angle of attack	
a.c.	Aerodynamic centre	
APU	Auxillary power unit	
BCA	Best cruise altitude	[ft]
BCM	Best cruise Mach	[-]
C.o.G.	Centre of gravity	
HUD	Heads-up display	
ICNIA	Integrated communication, navigation, and identification avionics	
KIAS	Knots indicated airspeed	[nmi/h]
M.A.C.	Mean aerodynamic chord	
MFDs	Multi-function displays	
MSL	Mean sea level	[ft]
OBIGGS	Onboard inert gas generation system	
OBOGS	Onboard oxygen generation system	
AR	Aspect ratio	
SFC	Specific fuel consumption	[lb/(h·lbf)] or [g/(s·kN)]

Symbols

α_0	Zero-lift angle of attack	[rad]
$\bar{\bar{c}}$	Wing mean aerodynamic chord	[ft] or [m]
$\bar{c}_w$	Mean chord of the wing	[ft] or [m]
$\Delta C_{Lw_{max}}$	Increment of maximum Wing lift coefficient	[-]
$\dot{\psi}$	Turn rate	[deg/s]
Γ_T	Dihedral angle of the tail	[°] or [rad]
λ_T	Tail taper ratio	[-]
$\Lambda_{T,LE}$	Sweep angle of the tail at leading edge	[°] or [rad]
$\Lambda_{w,LE}$	Sweep angle of the wing at leading edge	[degrees]
AR_T	Tail aspect ratio	[-]
b_w	Wing span	[ft] or [m]
C_f	Friction coefficient	
C_m	Aircraft overall pitch moment coefficient	[-]
$C_{D0,w}$	Wing parasite drag coefficient	[-]
C_{LT,α_N}	Tail lift coefficient slope measured in the plane normal to each plane panel	[rad^{-1}]

C_{LT,α_t}	Tail lift coefficient slope measured in plane symmetry	[rad^{-1}]
C_{LT}	Tail lift coefficient	[-]
$C_{Lw,\alpha}$	Wing lift curve slope	[rad^{-}1]
C_{Lw}	Wings lift coefficient	[-]
C_{m0}	Wings pitch moment coefficient at quarter chord	[-]
$C_{m\text{fus}}$	Fuselage pitch moment coefficient	[-]
C_{mT}	Tail pitch moment coefficient at quarter chord	[-]
C_{YT,β_t}	Tail lateral-force coefficient slope measured normal to plane of symmetry	[rad^{-1}]
FF	Form factor	
h	Position of the C.o.G. expressed as a fraction of the M.A.C.	[-]
h_0	Position of the a.c. expressed as a fraction of the M.A.C.	[-]
h_n	Position of the controls fixed neutral point expressed as a fraction of the M.A.C.	[-]
K_n	Controls fixed stability margin	[%]
l_T	Moment arm of the tail (longitudinal distance between the C.o.G. and the a.c. of the tail)	[ft] or [m]
M_{ac}	Pitching moment around the a.c.	[Nm]
Q	Interference factor	
R	Level turning radius	[ft]
S	Wings planform area	[ft^2] or [m^2]
S_T	Tail planform area	[ft^2] or [m^2]
V_0	Free stream velocity	[knots]
V_T	Tail volume ratio	[-]
V_{stall}	Stall speed	[m/s]
V_{TD}	Touchdown velocity	[m/s]
V_{TO}	Takeoff velocity	[m/s]
W_0	Aircraft design gross weight	[lb]
W_{crew}	Crew weight	[lb]
W_e	Aircraft empty weight	[lb]
W_f	Weight of fuel	[lb]
$W_{payload}$	Payload weight	[lb]
$x_{ac,w}$	Longitudinal position of the a.c. of the wings	[ft] or [m]
x_{cg}	Longitudinal position of the centre of gravity	[ft] or [m]
C_{l_α}	Airfoil lift coefficient slope	[rad^{-1}]
C_{Lw_α}	Wing lift coefficient slope	[rad^{-1}]
$\text{C}_{Lw_{max}}$	Maximum Wing lift coefficient	[-]
M	Mach number	[-]
t/c	Thickness to chord ratio	[-]

1 Introduction

Driven by the upcoming retirement of the T-38C fleet, the US Air Force issued a request for proposal in late December 2016 for an Advanced Pilot Training Aircraft. This two-seated trainer is expected to take over the training responsibilities of both the T-38 and the two seated version of the F-16. In addition, this renewal is an opportunity to answer the growing needs for trainer aircraft to support modern fighters such as the F-22.

This context is an exciting opportunity for graduate students in Aerospace Engineering to muster their recently learned skills in aeronautics in a attempt to answer this request for proposal with a design of their own. This report presents the details of the design and the performance assessment of the Coyote, a V-tail training fighter.
A brief description of the mission and of the design objectives will first be presented in section 2. Then, the main features of the configuration selected for the Coyote will be introduced and compared to alternatives in section 3. After that, the design choices and methods will be described in details. In the early stage of the design, the main components will be designed thanks to an extensive use of empirical and statistical methods. In later stages, more advanced tools may be used to investigate some aspects of the design (mainly the aerodynamics and the details of the structure) with a higher accuracy. The cost of the aircraft will also be evaluated. Then, the performance of the Coyote will be assessed and compliance with the objectives will be checked. At last, a few trade-off studies will be presented to ensure the actual design is optimal.

2 Mission description & design objectives

A schematic overview of the design mission is provided in Fig. 1. It contains several cruise segments at BCM and BCA, a simulated refuel and a manoeuvre segment.

The Coyote should comply with the performance objectives denoted in Tab. 1. These are the main measures of merit of the design and should be considered as targets during the design.
Note that the 20-minute long sustained 9g manoeuvres requirement is subject to interpretation. This would lead to an excessively heavy and costly trainer, and the cost objective could probably not be met. As a comparison, even the F-16 cannot sustain 9g continuously at combat weight and altitude. It is however reasonable to assume that, if 6g may be maintained in a continuous manner during the entire manoeuvre segment, 9g manoeuvres may readily be achieved, but with a deceleration of the aircraft (during a pull-up for example). Following this consideration, 6g continuous manoeuvres are

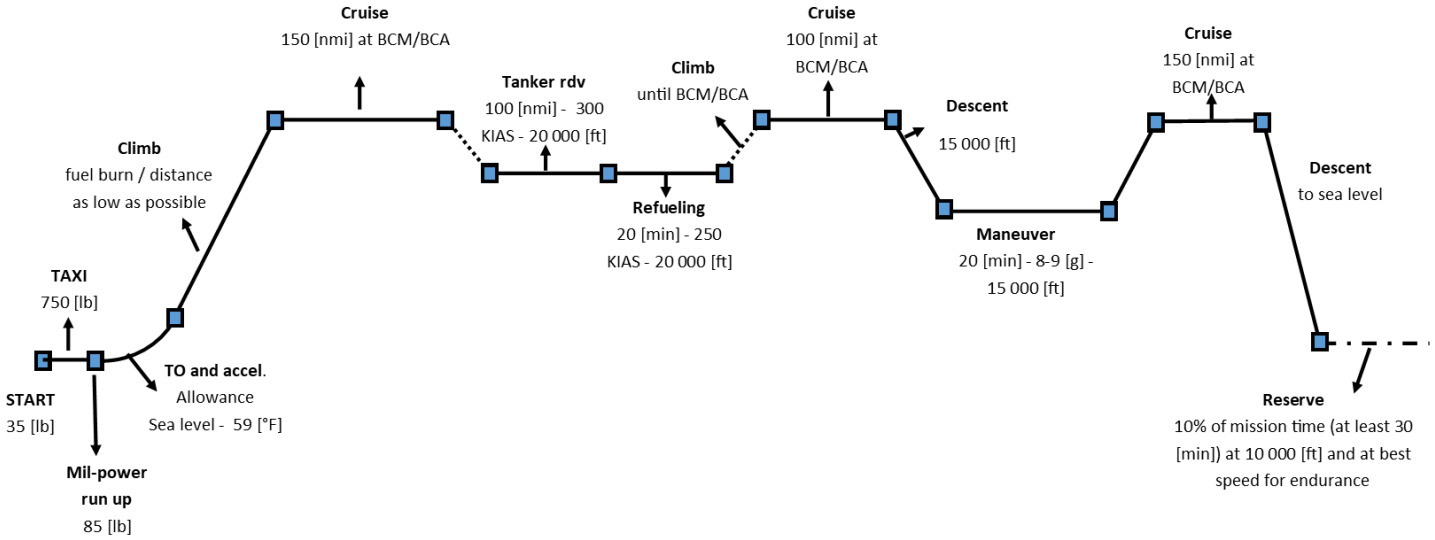

Figure 1: Schematic description of the design mission divided into consistent segments. The altitude is measured from the MSL.

set as the actual design objective.

Criteria	Requirement threshold	Requirement Objective
Sustained g at 15 000 [ft] MSL	8	9
Ceiling	40 000 [ft]	50 000 [ft]
Minimum Runway Length	8000 [ft]	6000 [ft]
Payload (Expendable)	500 [lbs]	1 000 [lbs]
Range (Unrefueled)	1000 [nmi]	1500 [nmi]
Cruise Speed	0.7M	0.8M
Dash Speed	0.95M	1.2M

Table 1: Design Performance Requirements.

3 Choice of configuration

The first phase of the design is to select a configuration for the trainer. By configuration is meant the three following features: the number of engines, the wing planform and the empenneage arrangement. Each design choice will be supported by a qualitative justification.

3.1 Number of engines

Trainers and fighters exhibit at most two engines. The two-engine configuration benefits from several advantages.

First, the failure of one engine is naturally less dramatic than in the case of a single engine configuration. Indeed, the second engine is still operational and an emergency landing at the closest runway has higher chances of success.
Second, there seems to be a larger variety of thrust class among smaller engines than among the powerful engines required for the single engine configuration. The total thrust of a two-engine trainer could thus probably be tailored more adequately to the needs of the mission.
Thirdly, a two-engine configuration would allow to position the engines under the wings (cf. Aermacchi M-346, Kawaski T-4 or Dassault Alpha-jet as examples), yielding a C.o.G. much closer to the nose than in the single engine configuration, which is attractive in terms of stability.

It is not easy to guess the impact of the number of engines on some other characteristics such as the total weight of the propulsion system, the fuel consumption or the drag induced by the fitting of the engines inside the fuselage.
It is reasonable however to assume that engines of similar technological level have comparable thrust to weight ratio and SFC. The total mass of the propulsion system and the fuel consumption should thus not differ significantly between a single or a two-engine configuration.
In the-two engine configuration, the engines are smaller but must be integrated side by side inside the fuselage. It would yield a reduction in the fuselage height but an increase in width compared to the single-engine configuration. It is thus not easy to decide on the impact on drag of the number of engines.

There remains the aspects of cost and maintenance. Without access to quantitative pieces of information, the discussion presented here is based mainly on intuition and good sense.
The cost of engine manufacturing is probably associated to the very accurate forming processes and to the assembly of the numerous components more than to the raw materials. It would seem reasonable to state that, for an equivalent total thrust, a single engine is cheaper to manufacture than two smaller ones.
Following the same line of thought, the maintenance of a single large engine is probably cheaper than that of two smaller engines (double the number of components to check and potentially replace).
For this training jet fighter, it has been decided that low manufacturing and maintenance cost prevail on performance, and the single engine configuration is retained. The engine is thus fitted inside the aft fuselage.

3.2 Wing planform

There are three common wing planform for trainers and fighters: sweptback, trapezoidal and delta. Many other configurations exist (forward sweep, closed wings, asymmetrical, blended wing body, etc.) but are far less common. Implementing such configurations would yield excessive certification costs.

On the one hand, the delta wing configuration presents the following advantages. First, the root chord is longer, meaning that thicker spars may be fitted inside the wings for the same thickness ratio, ensuring a strong and stiff wing. Second, the wing area of a delta configuration is generally larger, yielding low wing loading. Thirdly, the large thickness and the large wing area imply that a significant amount of volume may be dedicated to fuel storage and retracted landing gears. Then, the development of leading edge vortices at high A.o.A. and low speed produces additional lift, and leading edge extensions are not required. At last, delta wings do not necessitate a tail.
It suffers however from some drawbacks. To start with, the large wing area induces a higher viscous drag. Then, delta wings generally have a small aspect ratio, yielding a large lift induced drag at subsonic speed. Additionally, they exhibit bad characteristics in deep stall. At last, the delta wing configuration often necessitates the implementation of a canard.

On the other hand, trapezoidal wings are very similar to sweptback wings, but generally exhibit a smaller wing area, yielding less viscous drag. Both the trapezoidal and sweptback wings benefit from better performance at transonic speed and easier use of flaps. However, they both stall at smaller angles of attack, and necessitate the use of root leading edge extensions.

A sweptback wing configuration is selected for this trainer because of its better behaviour at transonic speeds. Indeed, the Coyote is likely to encounter transonic flows during the mission, and must be able to dash to 1.2 M.
In addition, a mid mounted wing configuration is selected for the Coyote. This choice yields a neutrally stable aircraft in roll, which is convenient for the good but not extreme manoeuvrability requirements of a trainer. It also provides a better field of view for the student and the instructor above their shoulders.

3.3 Empennage arrangement

Most trainers and fighters exhibit a conventional cruciform tail, with either a single large fin or two smaller twin fins. The T-tail (F-104 Starfighter) and the V-tail (Fougha CM-170 Magister) configurations also exist, but are less common.

The main advantage of the T-tail is that it is positioned well outside the disturbed flow in the wake of the wing and of the fuselage, yielding a more predictable behaviour of the tail, and a better pitch control. It is however prone to the dangerous deep stall if the aircraft flies at high A.o.A. Since high A.o.A. flight is necessary to perform high-g manoeuvres, this configuration is discarded.
The V-tail configuration should theoretically reduce the wetted area of the tail (two surfaces instead of three for the conventional arrangement) but extensive NACA research ([15]) has concluded that, to obtain the same stability and control as other tails, the V surfaces have to be upsized to nearly the same total area as would be required for separate horizontal and vertical surfaces. This configuration presents nonetheless the following advantages:

- Less interference drag because V-tail has fewer fuselage-tail junctures (vortices created at intersection of surfaces),
- Less tendency toward rudder lock,
- Higher location of tail surfaces, which tends to reduce elevator deflection required for take-off and landing, and to reduce possibilities of tail buffeting from the wing and canopy wakes in high-speed flight (not in the wake of the fuselage at high A.o.A. but can find themselves in the wake of the LEX),
- Fewer tail surfaces to manufacture.

However, the V-tail has the following drawbacks:

- Possible interaction of elevator and rudder control forces,
- Possible interaction of elevator and rudder trimming when tabs are at fairly large deflections,
- More complicated operating mechanism (adverse roll-yaw coupling),
- Greater loads on tail and fuselage, which tends to increase the structural weight.

In the end, the audacious V-tail configuration is selected for its potential reduction in viscous drag, and to differentiate the Coyote from the other trainers of the market.

It must be kept in mind that the aircraft should be able to fly at supersonic speeds. Thus, an all-movable tail has to be used in such flight conditions to deal with Mach tuck and buzz.
Unfortunatley, an all-movable tail is not suitable for a V-tail in subsonic flight because it loses yaw stability. Then, a switching mechanism from ruddervators to all-movable tail must be activated when transitioning from subsonic to supersonic. The tail should be fixed with only the ruddervators movable

in subsonic flight while the ruddervators should be locked with an all-movable tail in supersonic flight. As a consequence, a good locking system is required.

3.4 Cruise altitude

The altitude of $35,000$ [ft] is wel known for yielding the best $(Thrust - Drag)$ and the lowest SFC (because the static temperature stops decreasing beyond this altitude) [6]. It is thus selected for cruise.

4 Methodology

In order to carry out the highly iterative sizing of the different components of the aircraft, statistical and empirical relations will be used extensively at first. For each components, the design methods and choices are presented and discussed in details.
Once the design of the main components is completed, specific analyses may be carried out. More advanced tools may then be used to study the aerodynamics, the structure, the handling qualities and the overall performance of the trainer.

The design phase stands out by its highly iterative character. Some quantities are fixed directly by the mission requirements or by design choices, but many other (weight, wing and tail lift, fuel weight, required thrust, etc.) form an iterative loop that cannot be solved in one go. It is thus necessary to clearly define the methodology used to address this iterative aspect.
The methodology followed here is described by Raymer in [16], chapter 2. It is briefly outlined here below and in Fig. 2. The mission description and requirements developed in section 2 together with the choice of configuration detailed in section 3 and the state of the art in terms of airfoils and propulsion form the input of the design process.
The actual design process begins with empty weight W_e and take-off weight W_{to} estimates computation from statistics compiled in section 5.1. These estimates depends naturally on the geometry of the wing, tail and fuselage, on the weight of the selected engine and on the volume of fuel. This is where the iterative character of the design resides. Once the total lift force the wing must generate is known for the current design, it may be sized in section 5.3. Once again, empirical relations may be used to relate the wing lift coefficient to that of the airfoil. A simplified drag polar is then used to compute drag estimates, allowing to determine the necessary thrust to complete the mission. This figure allows to select the engine and to compute an estimate of the fuel consumption of each mission segment in section 5.5. The next step is to design the fuselage, as detailed in section 5.6. The nose and cockpit sections may be considered fixed, and are not part of the iterative loop. The middle and aft sections

must provide the necessary volume to house the engine, the fuel and the landing gears, on top of the pieces of equipment listed in the request for proposal. The fuel tanks layout must also be selected at this step. Then, the position of the C.o.G. of the trainer may be approximated as well as its excursion when fuel is consumed in section 5.7. The V-tail surfaces are then sized to reach manoeuvrability characteristics targets in section 5.8. After that, static stability margins may be approximated and the wing is positioned along the fuselage to ensure the former lie within the admissible interval as shown in section 8.

Naturally, it is unlikely that W_e and W_{to} of the current design matches those of the previous iteration (which have been used as inputs to the current iteration). It is thus necessary to iterate with the new weight estimates until convergence is reached. Then, two preliminary criteria are used to determine if the current design has a chance to comply with the objectives: is the trainer able to achieve 6 g continuously during the complete manoeuvres segment? Are the longitudinal static stability margins within the admissible interval at all time? If it does not pass the preliminary test, the design must be changed and the iterative loop continues. If it does pass the preliminary test, the performance of the current design are evaluated in section 10. If it does not comply with the requirements listed in Tab. 1, the design must be modified and iterated upon again. If it does comply, the design is then frozen. A cost analysis is then detailed in section 12, and a trade-off study is carried out in section 11.

Drawings and data summaries of the final iteration of Coyote may at last be outputted (cf. appendix), finalising the design.

5 Components design

5.1 Statistical survey

The design loop must be initiated with guesstimates for W_e and W_{to}. Selecting appropriate guesstimates may significantly reduce the number of iterations required to converge to a fully compliant design. It is thus interesting to perform a quick statistical survey of existing trainers around the globe. In addition, it may as well provide insight about mean values of AR and wing area to guide the selection of these parameters for the Coyote. Mean thrust (military) to weight (W_e) ratio and wing loading (level flight at MTOW) were also compiled to allow for comparison once the design of the Coyote is completed.

One may observe that the standard deviation for W_e, the MTOW, the thrust to weight ratio and the wing loading amounts to about 30 % of the mean values, highlighting the large variety of designs, even among the sub-class of trainers.

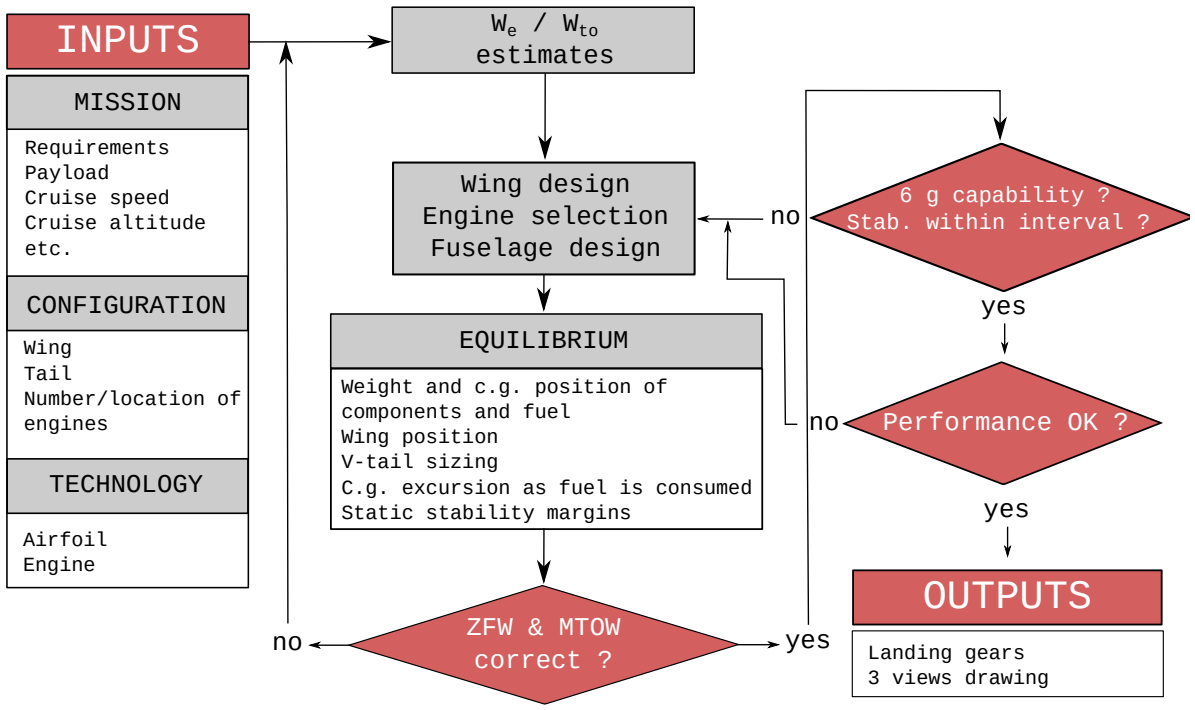

Figure 2: Overview of the design method. Adapted from [11].

	W_e [lb]	MTOW [lb]	S [ft^2]	AR [-]	$\frac{W_f}{W_e}$ [-]	$\frac{T_{mil}}{W_e}$ [-]	L/S [lb/ft^2]
M-346 Master	10,163	20,940	253	4.0		1.24	82.7
KAI T-50 Golden Eagle	14,264	27,120	255	3.8		0.83	106.3
Kawasaki T-4	8,355	16,530	226	4.7		0.86	73.1
Yakovlev Yak-130	10,141	22,680	253	4.1		1.09	89.6
Hongdu JL-8	5,924	9,550	183	5.5		0.61	52.2
T-45 Goshawk	9,833	14,080	191	5.0		0.62	73.9
BAE Systems Hawk	9,877	20,060	180	5.9		0.66	111.6
Northrop T-38 Talon	7,209	12,090	170	3.8		0.57	71.1
Dassault/Dornier Alpha Jet	3515	16,530	188	4.7		0.77	87.8
Aermacchi MB-339	7,749	10,800	208	6.1	0.36	0.59	52.0
Saab 105	6,281	10,220	175	5.5		0.93	58.2
Sako G-2 Galeb	5,776	9,480	209	6.9	0.30	0.47	45.3
Mean	8,530	15,840	207.6	5.0	0.33	0.77	75.3
Standard deviation	2,824	5,820	31.96	1.0		0.23	21.3

Table 2: Statistical survey of some existing trainers. Compiled from Wikipedia.

5.2 Weight estimates

It has been highlighted in the methodology section that a first guesstimate of W_{to}, the total weight of the aircraft at take-off, must be selected. This guesstimate will allow subsequent weight iterations to converge more rapidly. One could simply select the average MTOW of the statistical survey presented in section 5.1 as W_{to} guesstimate. This is however impossible to know the respective participations of the fuel and of the payload to this average MTOW. In addition, the MTOW is likely larger that the take-off weight for a standard training mission. Taking advantage that the weight of the crew is specified and that the weight of the payload is set in the design objectives to 1000 $[lb]$, it is interesting to define the gross weight of the trainer as:

$$W_{to} = W_e + W_f + W_{crew} + W_{payload} \tag{5.1}$$

$$= W_e \left(1 + \frac{W_f}{W_e}\right) + W_{crew} + W_{paylaod}. \tag{5.2}$$

Using the mean values in Tab. 2 for the empty weight and the fuel to empty weight ratio as inputs to this equation yields the weight guesstimate:

$$W_{to} = 12,870 \ [lb]. \tag{5.3}$$

This initial estimate may then be inputted to empirical relations (provided by Raymer in [16], chapter 15) to evaluate the weight of individual components such as the wing, the fuselage, the V-tail, etc. for the current design. The dependency of these weight estimates with the geometric parameters of the design are highlighted here below for the main contributors to the total weight.

- Wing : design gross weight, ultimate load factor, wing geometry and area, control surface area;
- Fuselage : design gross weight, ultimate load factor, structural length, width and depth;
- V-tail : fin area, ultimate load factor, design gross weight, tail geometry and area;

In addition, a detailed list of pieces of equipment and their respective weight is provided in the request for proposal. These may be directly included in the weight estimate.
Two additional components participate significantly to W_{to}: the weight of the engine and of the fuel. The former is readily available in manufacturers data sheets. The latter however must be estimated for the current design by evaluating the fuel consumption of each mission segment. These two aspects will be addressed in section 5.5. Note that although empirical relations are used for the early iterations of the design, the weight may be estimated at later stages of the design directly on a CAD model (once

the details of the internal structure have been designed). The final weight estimates are displayed in Fig. 3 with the empirical approximations and in Fig. 4 with the direct extraction from the CAD model. As general comments, first note that the weight of fuel amounts to about 35 % of the gross weight, which is not that different than the two figures available in the survey Tab. 2. Then, the engine, the wing and the fuselage all correspond to a significant fraction of the gross weight.

Second, notice that the design converged to a much heavier aircraft than the trainers listed in Tab. 2. In terms of weight, the Coyote is actually close to small fighter jets such as the F-16 (the loaded weight of the F-16 Block 50 amounts 26,500 [lb] [4]). This probably comes from the fact that this design is an advanced training aircraft, and must exhibit high g manoeuvres capabilities.

Compared to the empirical estimates, the weights extracted from the CAD model is actually fairly close. It may be observed that the weight of the wing and the fuselage have decreased. It may be explained by the use of lighter materials (aluminium and titanium alloys) than ones employed for older fighters. Regarding the group *others*, it takes now a larger part of the chart since it encompasses more components than the corresponding group of Fig. 3. Indeed, weight of the fuel tanks and of the canopy have been added.

Once the weight estimates computation is completed, estimating the lift force the wing must generate during level flight is straightforward, allowing to size of the wing.

5.2.1 Final results

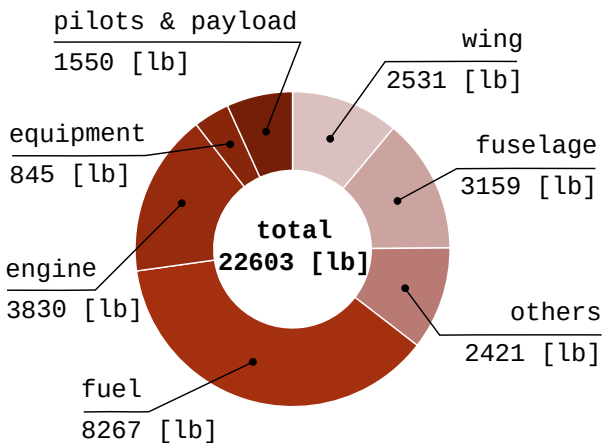

Figure 3: Empirical estimates of the weight contributions.

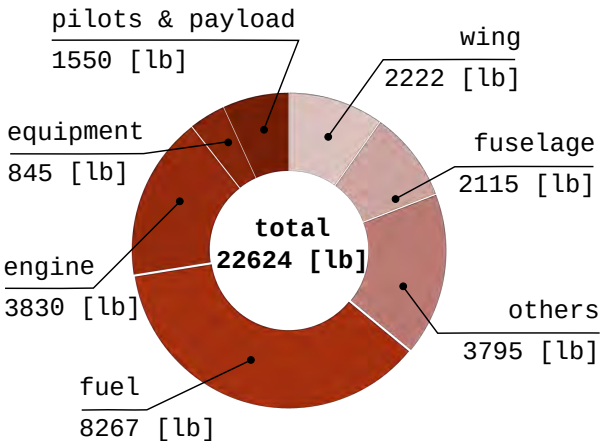

Figure 4: Estimates of the weight contributions from the CAD model.

5.3 Wing design

The purpose of this step is to design the wing such that it generates a sufficiently large lift force to maintain the aircraft in flight. Lift force is generally discussed in terms of non dimensional lift

coefficients. It is common to design the wing for cruise since it makes up most part of the design mission, even for a trainer. The most demanding cruise phase for the wing is naturally at the very beginning of the mission, for a weight that is considered to be W_{to} here. Assuming that only the wing and the tail contribute to the overall lift force applied on the aircraft, a vertical force balance allows to write, for level flight:

$$\begin{aligned} C_{L,plane} = \frac{W_{to}}{\frac{1}{2}\rho V_0^2 S} &= C_{L,w} + \frac{S_T}{S} C_{L,T} \\ \Rightarrow C_{L,w} &= \frac{W_{to}}{\frac{1}{2}\rho V_0^2 S} - \frac{S_T}{S} C_{L,T}. \end{aligned} \tag{5.4}$$

In this equation, the lift coefficient of the tail is determined by enforcing equilibrium in pitch. This aspect is treated in section 5.8, and $C_{L,T}$ together with S_T are assumed known for the current design in the methodology described below (it is set to 0 for the first iteration).

The methodology adopted here is first to select the geometric parameters of the wing. This selection is guided by statistical data compiled from existing trainers and fighters in [16], chapter 4, or by the survey compiled in Tab. 2.

5.3.1 Aspect ratio

Large AR wings benefit from less intense 3D effects since the flow seen by the wing is then mostly two dimensional. Mainly, this has the effect to reduce the lift induced drag. Enlarging the AR however implies increasing the bending moment experienced by the structure at the wing root. This is why AR are limited to smaller values when high g manoeuvres capabilities are required. The statistics provided in Tab. 2 indicates a mean value of 5 for the 12 trainers included in the survey. Since the maximum design load factor is high (9g), a slightly smaller value is selected here: 4.5.

5.3.2 Sweep angle

Introducing a sweep angle is necessary to delay the formation of shocks and/or to reduce their strength in transonic and supersonic conditions. A general rule is to select the wing sweep angle at leading edge $\Lambda_{w,LE}$ aft of the smallest Mach cone angle, that is for $M_{max} = 1.2$:

$$\theta_{cone} = \arcsin \frac{1}{M_{max}} = 56.4 \text{ [deg]}, \tag{5.5}$$

measured from the longitudinal direction ([16], page 54). Sweep angles are generally measured from the spanwise direction, such that the selected angle:

$$\Lambda_{w,LE} = 35 \text{ [deg]} \tag{5.6}$$

is indeed inside the Mach cone.

5.3.3 Taper ratio

Taper is introduced to minimise the lift induced drag by approaching an elliptical lift distribution. For straight wings, a taper of 0.35 yields the smallest induced drag. Most swept wings exhibit a taper ratio between 0.2 and 0.3 ([16], chapter 4). The ratio selected here is: $\lambda_w = 0.3$.

5.3.4 Thickness ratio

The thickness ratio t/c for aircraft experiencing transonic flow conditions must be selected small, delaying the development of shocks and minimising the associated wave drag. Fig. A.14 from [16] in the appendix provides guidelines to select the thickness ratio for a given maximum Mach number, based on historical trends. The trend line indicates a thickness ratio of about 5 % for $M_{max} = 1.2$. This value has however to be confronted with the availability of experimental measurements for the selected airfoil. The selected thickness ratio is 6 %. However, there is no guarantee that test data with this specific thickness ratio may be found.

5.3.5 Airfoil selection

Raymer advises to select an airfoil from the 64-A 6 digits family as starting points for high-speed wings in [16], chapter 4. These were designed to achieve higher proportions of laminar flow, minimising drag. A small camber is desirable to improve the lift generation whilst maintaining drag as small as possible. After research for experimental tests data, the 6 % thickness ratio NACA 64-206 is selected, with extensive experimental testing compiled in [3] (tests data about a 5 % t/c equivalent could not be found). Section lift coefficient tests data are displayed in Fig. 5 (left).

5.3.6 Geometric and aerodynamic twist

A negative twist (wash-out) may be introduced to avoid tip stall and the associated sudden loss in roll control. The same airfoil is used at the tip and at the root for the simplicity of the design and manufacturing. The aerodynamic twist is thus zero. The wing tip should however be twisted geometrically. Tip twist angles are generally chosen between 0 and -5 [deg]. A moderate value of -2 [deg] is selected here.

5.3.7 Lift coefficient and wing area

Now that the geometric parameters of the wing have been selected, the reference area may be computed. In the methodology followed here, the wing lift coefficient is selected such that the lift to drag ratio of the aircraft is optimal during cruise. To this end, a quadratic drag polar model may be used

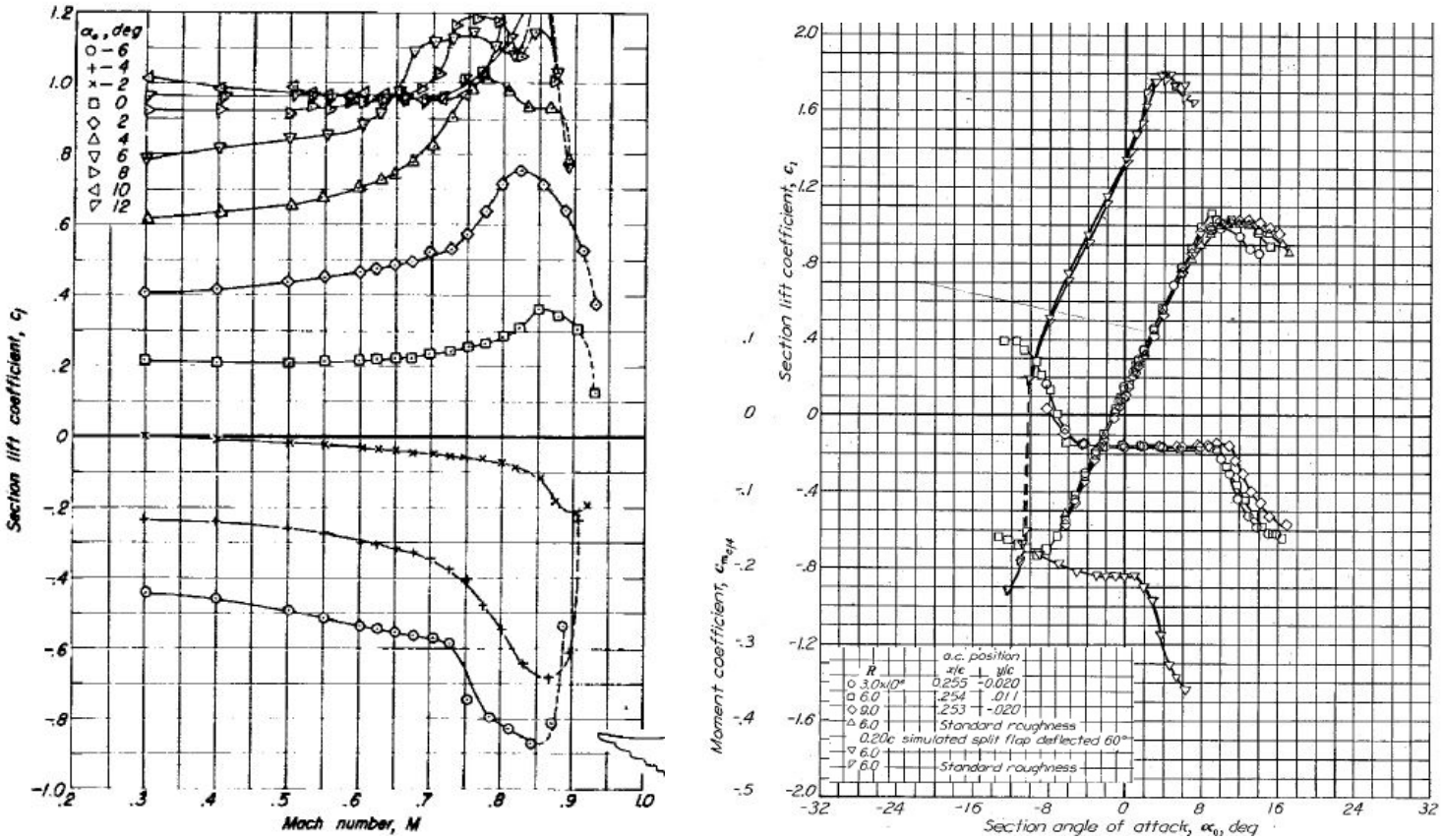

Figure 5: Airfoil data from experimental tests. On the left side, section lift coefficient of the NACA 64-206 with respect to the Mach number ([3], page 181). On the right side, section lift coefficient of the NACA 64-206 with a split flap at a deflection angle of 60 [°] with respect to the A.o.A. for different Reynolds number ([8], page 30).

to asses the drag coefficient for a given C_L as a first approximation:

$$C_{D,plane} = C_{D0} + \frac{C_{L,plane}^2}{e\pi AR}. \tag{5.7}$$

The zero lift drag C_{D0} and Oswald's factor are situated within the respective intervals $[0.14 - 0.20]$ and $[0.75 - 0.85]$ for high subsonic jet aircraft according to [17], chapter 5. Selecting the worst case values 0.20 and 0.75 respectively allows to stay conservative in this first drag assessment. In addition, compressibility effects for high speed cruise (0.8 M in this case) may also be accounted for by adding an extra 0.0020 to the zero lift coefficient, yielding as final values :

$$C_{D0} = 0.022 \quad \text{and} \quad e = 0.75. \tag{5.8}$$

The resulting drag polar is displayed in Fig. 6 (left).

The lift to drag ratio may then readily be calculated as a function of the lift coefficient, and is depicted in Fig. 6 (right). One may observe that an optimal lift to drag ratio of about 10 is achieved with a $C_{L,plane}$ in the interval $[0.4 - 0.6]$. Assuming that the required lift coefficient of the tail to ensure

equilibrium in pitch is small, Eq. 5.4 indicates that the optimal $C_{L,w}$ may be considered optimal in a similar interval. The bottom value of the interval is selected:

$$C_{L,w} = 0.40, \tag{5.9}$$

for the following reason. Thin airfoils such as that selected for this wing exhibit flow separation at relatively small A.o.A. (for the NACA 64-206, separation starts at 8 [deg] according to Fig. 5). Selecting a $C_{L,w}$ as high as 0.60 for cruise would thus likely push the wing dangerously close to stall for more demanding flight phases (mainly manoeuvres).

Since the cruise mach number is set at 0.8 M in the design objectives and a cruise altitude of $35,000$ [ft] has been selected, Eq. 5.4 allows to determine the required wing area to develop the design lift coefficient for the current iteration.

5.3.8 3D lift curve slope, zero-lift angle & incidence angle

3D lift curve slope As a first approximation, the 3D lift curve slope may be computed with the following formula from the DATCOM method ([17], page 273):

$$C_{L\alpha} = \frac{1}{\beta} \frac{2\pi}{\frac{2}{\beta AR} + \sqrt{\left(\frac{1}{k\ \cos(\Lambda_\beta)}\right)^2 + \left(\frac{2}{\beta AR}\right)^2}}, \tag{5.10}$$

with β, k and Λ_β:

$$\beta = \sqrt{1 - M^2}, \quad k = \frac{\beta C_{l\alpha}}{2\pi}, \quad \tan(\Lambda_\beta) = \frac{\tan(\Lambda_{1/4})}{\sqrt{1 - M^2}}.$$

The section lift curve slope may readily be computed using Fig. 5 (left) for 0.8 M. All the parameters in the equation are fixed, and the 3D lift curve slope at 0.8 M is then equal to 4.3 [rad^{-1}] for every iteration.

The A.o.A. associated to the wing lift coefficient of 0.40 is then equal to 4°, which is comfortably far from stall.

Wing zero-lift angle The zero lift A.o.A. of the airfoil selected for the Coyote is estimated from Fig. 5 (right) to be equal to -1.5 [°]. In addition, geometrical twist (there is no aerodynamic twist here) must be accounted for in the calculation of the zero-lift angle of the wing. The zero-lift A.o.A. at the root may then be computed with the following formula ([17], page 475):

$$\alpha_{0,L} = \alpha_{0,l} + \epsilon_{g_{tip}} \alpha_{inc}, \tag{5.11}$$

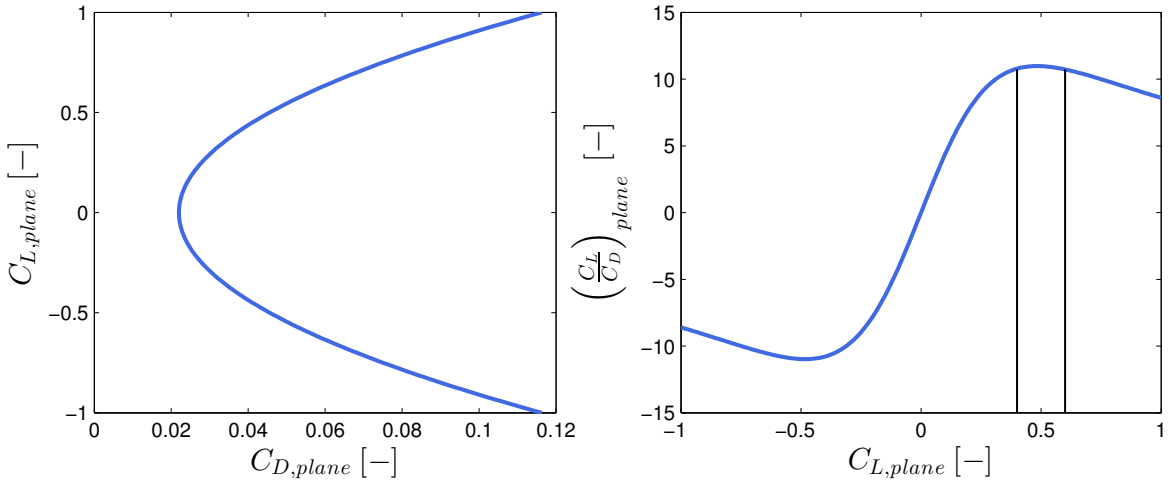

Figure 6: (Left) Initial drag polar estimate of the aircraft. (Right) Lift to drag ratio of the aircraft as a function of the lift coefficient. ($AR = 4.5$, $C_{D0} = 0.022$ and $e = 0.75$)

with $\epsilon_{g_{tip}}$ the geometrical twist and α_{inc} the zero-lift A.o.A. increment per unit of twist (taken from Fig. A.13). This results in a wing zero-lift A.o.A. at the root of -1.17 [°].

Wing root incidence angle The incidence angle of the wing on the fuselage is selected such that the A.o.A. of the fuselage is equal to zero for level flight at 50 % fuel in order to minimise drag. This value then depends on the weight and fuel consumption estimates of the current iteration. It may at first be assessed with the empirical lift curve slope and the zero-lift A.o.A. of the wing. Later on, it may be computed with the software Tranair, a potential flow solver.

5.3.9 Maximum lift coefficient

An important variable concerning the wing lift is the maximum lift coefficient $C_{Lw_{max}}$ it is able to generate. Computing it requires to study the flow around the wing close to stall conditions, and is beyond the scope of this design. The following empirical formula is used to assess it instead ([16], chapter 12, page 272):

$$C_{Lw_{max}} = C_{l_{max}} \left(\frac{C_{Lw_{max}}}{C_{l_{max}}} \right) + \Delta C_{Lw_{max}}. \tag{5.12}$$

In this expression, $C_{l_{max}}$ is the airfoil maximum lift coefficient at $M = 0.2$. The ratio may be approximated using Fig A.10 (in appendix) and the last term is a correction for higher Mach numbers (see Fig. A.11). The results depend thus on the Mach number and two cases have been studied: at $M = 0.6$ and at $M = 0.3$. Unfortunately, the limited empirical data from [16] (see the figures from Appendix A) do not allow to compute the $C_{l_{max}}$ at higher Mach number.

Additionaly, the corresponding stall A.o.A. may be computed with:

$$\alpha_{C_{Lw_{max}}} = \frac{C_{Lw_{max}}}{C_{l_{max}}} + \alpha_{0,L} + \Delta\alpha_{C_{Lw_{max}}}, \tag{5.13}$$

where the A.o.A. increment for subsonic maximum lift $\Delta\alpha_{C_{Lw_{max}}}$ is obtained from the appropriate figure (see appendix A.12) and $\alpha_{0,L}$ is the A.o.A. of zero lift of the wing. All the empirical quantities introduced here depend on geometric parameters of the wing that are fixed, and are thus independent on the iteration. Tab. 3 summarises the numerical values and the stall A.o.A. Notice that these values are rather small, which is a consequence of the thin and slightly cambered wing selected here. This maximum lift coefficient may be enhanced by implementing high-lift devices, which is the topic of the following section.

$C_{Lw_{max}}$ and their corresponding A.o.A. (flaps in)	
Mach 0.6	
$C_{Lw_{max}}$	0.84
A.o.A.	16.1 [°]
Mach 0.3	
$C_{Lw_{max}}$	0.94
A.o.A.	18.5 [°]

Table 3: $C_{L,w_{max}}$ and the corresponding angles of attack at different Mach numbers (flaps in).

5.3.10 Final geometry

The wing geometry of the final design is compiled in Tab. 4. Notice that the wing aera of the Coyote converged to a higher value that the average determined in the survey of Tab. 2 since it is also much heavier than the trainers included in it.

Wing parameters	
Surface: S	269 [ft^2] (25 [m^2])
Aspect ratio: AR_W	4.5
Taper ratio: λ_W	0.3
Sweep angle (LE): $\Lambda_{W,LE}$	35 [°]
Sweep angle (C/4): $\Lambda_{W,C/4}$	30,1 [°]
Span: b_W	34.8 [ft] (10.6 [m])
Chord at root: $C_{root,w}$	11.9 [ft] (3.6 [m])
Chord at tip: $C_{tip,w}$	3.6 [ft] (1.1 [m])
Dihedral angle: Γ_w	0 [°]
Incidence angle: i_W	3.0 [°]

Table 4: Numerical values of the wing parameters.

5.4 High-lift devices

Several high lift devices are implemented on the Coyote and are depicted schematically in Fig. 7: wing root leading edge extensions, flaperons and leading edge flaps. These devices are treated separately here below.

5.4.1 Leading edge extension

The sweptback configuration selected for the trainer necessitates the use of leading edge extensions (LEX). Their purpose is to provide additional lift at high A.o.A. by generating vortices. These vortices then re-energise the flow above the wing and delay stall.

The LEX allow for shorter turning radii and increase the intensity of the manoeuvres the trainer can perform by outstretching the C_{Lw_α} curve of the wings.

Quantifying the effect of LEX on the lift curve is complex, and cannot be done at this conceptual stage. It seems however reasonable to assume that they add around 0.4 to the lift coefficient[1] at high A.o.A. (an increase of about 50 %).

5.4.2 Flaperons

The maximum lift generated by the wing may be enhanced by implementing flaps on the trailing edge. It has been decided to install flaperons instead of flaps: this deflecting surfaces may serve as

[1]This value is given by D. Raymer in [16], chapter 12, page 279.

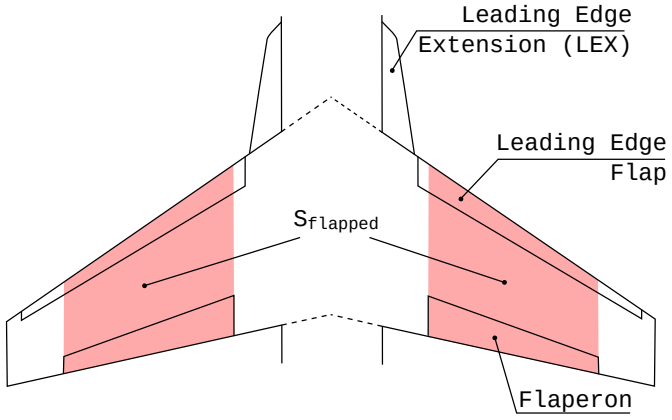

Figure 7: Schematic overview of the high lift devices implemented on the Coyote.

Flaperons deflection [°]	$C_{Lw_{max}}$
0	0.94
10	1.01
20	1.08
30	1.15
40	1.22
50	1.29
60	1.36

Table 5: $C_{Lw_{max}}$ at $M = 0.3$ for different flaperons deflections.

flaps as well as ailerons by deflecting in unison or in opposition respectively. This versatility for the trailing edge surface should allow for mass reduction since only one system of actuators is necessary. Note that most fighters (F-15, F-18 or F-22 to name a few) exhibit both flaperons on the inboard section and ailerons on the outboard section of the wing. The choice of implementing flaperons only is motivated by the fact that the moderate size and weight of the Coyote should imply a small inertia in roll. The F-16 (which is of similar weight and size than the Coyote) also exhibit flaperons only.

To compute the influence of the flaps deflection on the $C_{L,\max}$, the following formula is used ([16], chapter 12, page 279):

$$\Delta C_{L,w_{max}} = \Delta C_{l_{max}} \left(\frac{S_{flapped}}{S} \right) cos(\Lambda_{H.L.}), \tag{5.14}$$

where $\Lambda_{H.L.}$ is the angle of the hinge line of the high-lift surface and $S_{flapped}$ the surface if the flaps were extended along the entire chord (as depicted in Fig. 7).

The flaps are designed here to extend along 20 % of the chord. The surface ratio is set to 55 %. $\Delta C_{l_{max}}$ is taken from Fig. 5 (right) and corresponds to a split flap deflection of 60 [°]. This yields an increment of 0.45 between a flaps in and a flaps out (60 [°]) configuration. The increment in maximum lift coefficient for intermediate flaps deflection is then interpolated linearly.

Note that the only experimental values available concern split flaps. In practice, plain flaperons are implemented here. Tab. 5 compiles the influence of the flaperons deflection.

5.4.3 Leading edge flaps

Modern fighters exhibit leading edge flaps, allowing to adapt the camber of the wing. Their purpose is mainly to delay wing stall at high A.o.A. by aligning the leading edge with the incoming flow. Quantifying these effects is however beyond the scope of this preliminary design. They are thus not taken into account at this stage of the design.

5.5 Propulsion

The drag polar introduced in section 5.3 allows to estimate the drag for any value of the aircraft lift coefficient. It means that the maximum required thrust may be computed, allowing for the selection of an appropriate engine. The fuel consumption of each mission segment may now also be assessed.

5.5.1 Engine selection

The most demanding segment of the mission for the engine corresponds to manoeuvres. To determine the thrust required to maintain n g in a continuous manner, the drag polar given by Eq. 5.7 may be used with a lift coefficient of:

$$C_{L,plane} = \frac{nW}{\frac{1}{2}\rho V_0^2 S}. \tag{5.15}$$

In this expression, W is the mean weight of the aircraft during the manoeuvres segment and ρ is known since the altitude of this mission segment is fixed to $15,000$ [ft] in the request for proposal. To yield the shortest turning radius, the aircraft must fly just above the stall speed. The maximum value of $C_{L,plane}$ associated to this speed is chosen. However, it is important to note that the effect of the LEX has not been taken into account here and these values should thus be considered as approximations. One can then derive the expression of the thrust (which is equal to the drag):

$$T = nW\frac{C_D}{C_L}. \tag{5.16}$$

The design is here confronted to two alternatives: select an engine with an afterburner and use it during 20 minutes or prefer not to use the afterburner during the manoeuvres, requiring an engine with a large military thrust. In the first case, the engine is lighter but it consumes much more fuel due to an increased specific fuel consumption (more than a factor two compared to the SFC of the same engine without afterburner). In the second, the engine is much heavier, but a smaller volume (thus weight) of fuel must be embarked. The two options have been investigated and the latter has been retained (heavy engine - no need for A/B during manoeuvres) for the following reasons. The first reason is that using the afterburner during 20 minutes is certainly a very demanding operation

for the engine. It may significantly reduce the lifetime of many components, increasing maintenance cost. The second reason is that the design converges to a much heavier aircraft than if the second option is adopted (the required volume of fuel increases massively).
It is thus decided to select an engine with a sufficient military thrust to sustain 6g manoeuvres at constant speed. Although the afterburner is not used for the design mission considered here (cf. section 2), it is installed on the Coyote. It may indeed prove useful to reach the dash speed of 1.2 M (especially to go quickly through the transonic) or to complete other training missions.

In order to evaluate the required thrust at static sea level (SSL) (it is generally the only available data regarding engines thrust) to perform the manoeuvres, a corrective factor accounting for altitude and Mach number must be computed through the following formula [14]:

$$\frac{\text{Thrust}_{available}}{\text{Thrust}_{SSL}} = \Big(1 - \frac{0.45(1+BPR)}{\sqrt{(1+0.75BPR)G}}M + \Big(0.6 + \frac{0.11BPR}{G}\Big)M^2\Big)\frac{\rho}{1.225}, \tag{5.17}$$

where G is a constant equal to 0.9 for low bypass ratio engines. The thrust may then drop to almost half of the SSL specifications. The maximum thrust must be further decreased by 4 % to account for losses due to the installation of the engine.
Although it is also an iterative process, the engine selected for the final iteration of the design is given here for the sake of clarity. It is the F100-PW-229 engine, the one that currently powers some of the F-16s and the F-15Es. All the available specifications are summarised in Tab. 6 [13]. Moreover, a CAD representation of this engine is represented in Fig.8. Note that the SFC are given at SSL.

General characteristics	
Engine model	F100-PW-229
Manufacturer	Pratt & Whitney
Type	Afterburning turbofan
Length	191 inches (490 cm)
Diameter (inlet)	34.8 inches (88 cm)
Diameter (max. external)	46.5 inches (118 cm)
Dry weight	3,829 pounds (1,737 kg)
Bypass ratio (BPR)	0.36:1
Performance	
Military thrust	17,800 lbf (79 kN)
Thrust with full afterburner	29,160 lbf (129.7 kN)
SFC at military thrust	0.76 lb/(lbf·h) (77.5 kg/(kN·h))
SFC with full afterburner	1.94 lb/(lbf·h) (197.8 kg/(kN·h))
Thrust-to-weight ratio	7.8:1

Table 6: Specifications of the F100-PW-229 engine selected for the aircraft.

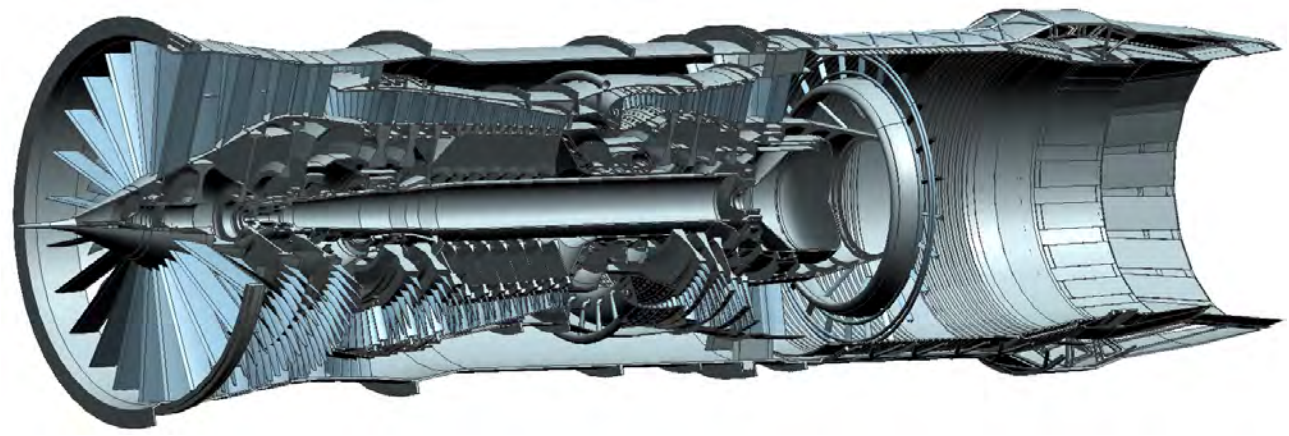

Figure 8: CAD model of the F100-PW-229 [9].

5.5.2 Fuel consumption and detailed description of the mission segments

In order to evaluate the overall fuel weight needed to complete the given mission with the chosen engine, the fuel consumption for each mission segment must be computed. This step is also required to evaluate the volume of the fuel tanks, witch will be discussed in section 5.6.2. Each mission segment will now be reviewed, and the methodology followed to find fuel consumption estimates will be exposed.

Ground operation This segment consists in start, warm-up and mil-power run-up. The associated fuel consumption is explicitly given in the request for proposal.

Cruise, tanker RDV & simulated refuel These segments correspond to steady and horizontal flight attitudes. In this configuration, the lift must be equal to the weight (taken as the mean weight during the segment) and the thrust must equate the drag. The latter may be evaluated with the drag polar with the appropriate lift coefficient. The fuel consumption can then be derived from:

$$Fuel\ Consumption = \int_{t_{ini}}^{t_{end}} SFC \cdot Thrust(t) \cdot dt, \tag{5.18}$$

where t_{ini} and t_{end} correspond respectively to the beginning and the end of the mission step, and where the SFC can be corrected for altitude and Mach number with graphs taken from [7]. Note that the required thrust varies in time since the weight of the aircraft decreases as fuel is consumed.

Climbs and descents The different climbs are considered as optimal climbs, meaning that the goal is to optimise the climb angle of the aircraft and thus the climb rate. Therefore, the engine must be set to full power (but without afterburner in order to limit the fuel consumption). After some calculations based on the force equilibrium acting on the plane when its velocity is constant, one finds the desired climb angle [16]. The rest of the analysis is then equivalent to the one carried out for cruise.
However, note that air density as well as the speed of sound change with altitude. Therefore, mean altitude values must be considered for each segment.
During the different descends, the fuel consumption is supposed to be equal to the consumption of the plane in cruise conditions, i.e. the same SFC and thrust are kept and introduced in Eq. 5.18. The descend time is evaluated by choosing the descend rate equal to the optimal climbing rate obtained for the climbs.
Note that even if an important approximation is made here, the fuel consumption associated to the descents is clearly negligible with respect to the one of the other mission segments. Even a large error on these consumption specifically would then not induce a significant error on the total consumption.

Manoeuvres The manoeuvre segment is assimilated to an horizontal circular path with an optimal turning radius at a constant load factor (the maximum the engine can sustain) [16]. Because the engine is operated at maximum rating during this 20-minute long segment, most of the necessary fuel is consumed here.

Reserves In the present case, because the whole mission only lasts around 110 minutes, fuel reserves have to be computed for 30 minutes at 10,000 feet and speed for maximum endurance. The speed of

the aircraft is assumed equal to the safety speed: 1.2 V_{stall}. This speed allows to reduce as much as possible the fuel consumption while keeping a security margin. From that, this segment is analysed exactly the same way as the other steady horizontal steps, i.e. cruise, tanker RDV and refuel.

Take-off & landing These segments will be described in details in section 10.3. The consumption related to the take-off segment may be computed once the time necessary to complete the segment is known by multiplying it by the take-off thrust (maximum military thrust) and the SFC. For the landing segment, a similar approach may be adopted with the exception that the engine rating is here idle. The idle thrust is taken as 0.4 the thrust in cruise.

5.5.3 Final fuel consumption estimates

The consumption of the different mission segments are represented in Fig.9. One can clearly notice that the manoeuvres account for a major part of the total consumption, as expected.

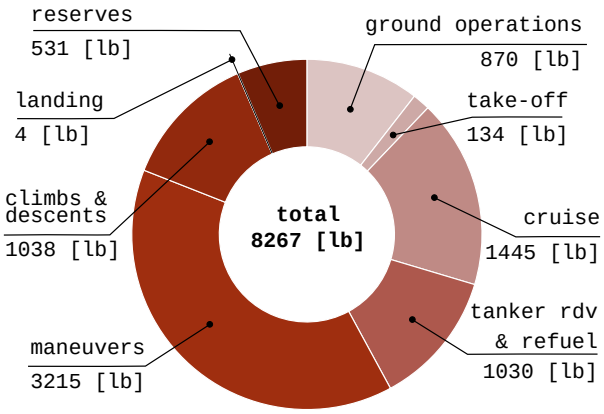

Figure 9: Estimates of the fuel consumption.

5.6 Fuselage, fuel tanks and general layout

Once the diameter of the engine and the total volume of fuel are known for the current design, the fuselage can be designed. In addition to the dimensions of it, the general layout of the aircraft must be selected. In particular, the fuel tanks must be defined and positioned, together with the list of pieces of equipment attached to the request for proposal.

5.6.1 Fuselage dimensions

The front section of the fuselage must provide sufficient space to accommodate the tandem cockpit. In order to have an idea of the length taken up by the nose and the cockpit, a mean value may be computed from measurements from 3 views drawings on a list of fighters and trainers. It reveals that about 16 to 20 [ft] are devoted to the nose and cockpit section. The length of the aft section housing

the engine is also known from the specifications of the engine of the current design. The middle section may then be devoted to house fuel, landing gears, and is traversed by the air intakes. In order to get a good airflow and not to impede on the visibility of the pilots, these are positioned below the wing at the two sides of the fuselage.
With these considerations, drawings may serve as guides to determine the dimensions (mainly length and width) of this middle section that *look* right as a starting point. In subsequent iterations, these dimensions may be adapted as the volume of fuel changes. The length of the fuselage also impacts on equilibrium and stability considerations through the moment arm of the tail.

5.6.2 General layout and fuel tanks locations

The general layout of the fuselage is depicted in Fig. 10. A convenient position for each piece of equipment in the list attached to the request for proposal has been selected. Regarding the position of components related to the engine, it makes sense to position them close to it, and the same applies for other kind of equipment. This is the reason why the APU is placed near the engine and why the OBIGGS is placed as close as possible to the fuel tanks; the MFDs, HUD and ejection seats share the same C.o.G. as the cockpit; OBOGS is located in the cockpit, etc.
In order to compute the C.o.G. position at any moment in flight, the fuel tanks layout must be designed. To minimise inertia loads during manoeuvres, it is a good practice to store fuel close to the C.o.G. of the empty trainer and close to the wing root for the wing tanks. Additionally, a slightly unstable configuration is attractive for enhanced manoeuvrability. For these reasons, a layout such that the C.o.G. of the fuel be ahead of that of the empty aircraft is selected. An additional constrain on the tanks layout is that the C.o.G. excursion should not exceed 7 % of the M.A.C.

Taking into account these considerations, the layout depicted in Fig. 10 is selected.
First, a small tank is fitted inside each half-wing. Notice that the tanks do not extend too close to the wing tips since these are prone to lightning bolts. Since the thickness ratio of the airfoil is small, only a small quantity of fuel may be stored there.
Second, a forward tank is fitted inside the fuselage in the free space between the engine and the cockpit. It is there that is stored the majority of the fuel.
At last, a rear tank is wrapped around the engine. This tank is necessary to avoid an excessive excursion of the C.o.G. Storing fuel so close to an heat source such as the engine may appear unreasonable. It probably induces additional considerations such as heat shielding. However, the F-16 attests the feasibility of this configuration. It is thus assumed here that such a fuel tank can be integrated.
The pumping sequence may be roughly described as follows:

- the forward and rear fuselage tanks are pumped simultaneously a trimmed rates to yield a gentle transition of the C.o.G. from the forward-most to the farthest aft configuration,
- the farthest aft configuration is reached once the forward tank is empty and the C.o.G. then translates forward as the remaining fuel in the rear tank is consumed,
- the wing tanks are then pumped last, so that they diminish the wing loading during most part of the flight.

5.6.3 Tanks capacity estimates

In order to ensure that a sufficient amount a fuel may be carried on board to complete the mission, an estimate of the volume of the fuel tanks must be computed. In the early stage of the design, as the trainer has not yet been modelled in a CAD software, this computation relies on drawings. First, the area of the fuel tanks at the successive longitudinal stations may be roughly estimated. Then, assuming a linear evolution of the tank area between two successive stations, an estimate of the volume of each tank may be computed. This method also allows to find an estimate of the C.o.G. of each fuel tank.
In the case of the wing tanks, the knowledge of the mathematical definition of the airfoil allows to easily estimate the internal volume. Since it is here more complex to assess the position of the C.o.G. of the tanks (due to internal structures), it was approximated by that of the entire wing in early C.o.G. assessments.
It is assumed that the loss of volume associated to the fuselage skin thickness and the internal structures (spars, ribs, longerons, etc.) amounts to 15 % of the total volume for fuselage tanks and 40 % for wing tanks (presence of flaperons and intricate fitting). In later staged of the design, the exact tanks volumes may be directly computed from the CAD model. In addition, Raymer advises to account for the tank walls thickness by considering another 8 % loss in volume for internal self-sealing tanks ([16], chapter 10, page 228). This figure amounts to 15 % in the case of tanks fitted inside the wings.

With these considerations, estimates of the capacity of each fuel tank and their respective C.o.G. may be computed for the current design. Fig. 11 depicts the volume estimates of the final iteration.

5.7 Centre of gravity estimates

The next step in the design process it to compute the centre of gravity of the aircraft at any moment in flight. It will allow to size the V-tail to reach manoeuvrability targets, to ensure equilibrium in pitch and to compute stability margins.

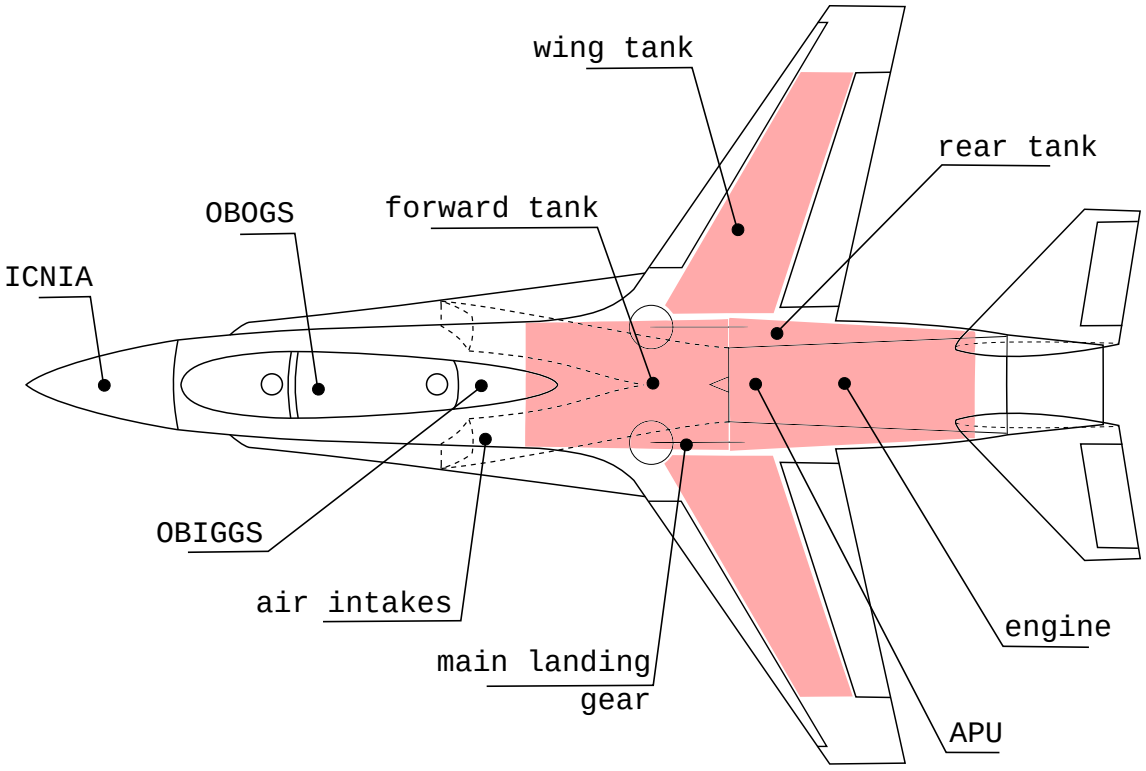

Figure 10: Schematic overview of the general layout.

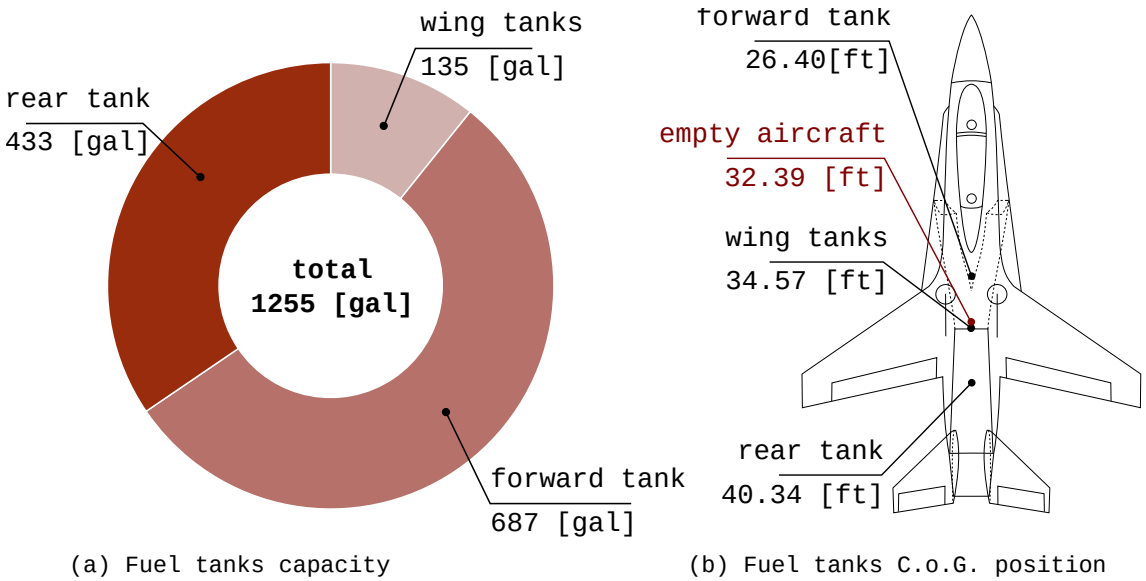

(a) Fuel tanks capacity

(b) Fuel tanks C.o.G. position

Figure 11: (a) Estimates of the fuel tanks capacity and (b) of their respective centre of gravity from the CAD model.

Early assessment of the C.o.G of the structure and the propulsion system requires to make a lot of assumptions. They are listed here below:

- C.o.G. of wing and tail is located at 30 % of their respective M.A.C.,
- C.o.G. of the fuselage is placed at 45 % of its length,
- C.o.G. of the cockpit is assumed to be at the middle of it,
- C.o.G. of gears are situated at the middle of their leg's length,
- C.o.G of the air intakes and the engine are located at 40 % of their respective length;
- C.o.G of payload is assumed to be the same as the wing since external stores are generally positioned below it.

In later stages of the design, the CAD model allows to determine the C.o.G. more accurately.

Note that the request for proposal is unclear about the question of payload. It specifies that the trainer should carry 1000 [lb] of payload, but does not detail the nature of it. Neither does it mention the necessity to install external stores, which are indeed an uncommon feature for a trainer. It is assumed here that 1000 [lb] of payload are indeed carried on board, but retained throughout the flight. Also notice that the electrical system's weight is spread across two locations (75 % of the weight in the cockpit and the rest in the engine) and the data bus is spread across the whole fuselage (its C.o.G. is thus at 50 % of the fuselage's length). The C.o.G. position of the empty aircraft for the current design may thus be estimated. Since the C.o.G. of the fuel may also be computed from the tanks layout described in section 5.6.2, the C.o.G. of the trainer may now be computed at any moment in flight.
In later stages of the design, it is possible to extract C.o.G. positions more accurately from the CAD model, along with inertia in rotation. The resulting positions are compiled in Tab. 7 with both the empirical estimates and the CAD model extraction. Notice that early estimates were fairly accurate.

	Empirical estimates [ft]	CAD model (x, y, z) [ft]	Inertia [slugs/ft^2]
Full fuel	31.90	(32.26, -6 10^{-3}, 2.78)	(9926, 74555, 81692)
50% of fuel	31.96	(32.41, -9 10^{-3}, 2.59)	(8428, 67005, 73003)
Farthest aft	32.13	(32.53, -9 10^{-3}, 2.36)	(7866, 61750, 68537)
Empty	32.09	(32.39, -0.01, 2.35)	(6792, 61601, 66319)
Max C.o.G. excursion in % of the M.A.C.	3.5	(4.1, 0, -6)	

Table 7: C.o.G. excursion assessed by both empirical estimates and CAD model (Fig. 34) and evolution of inertia.

5.8 V-tail design & imposing equilibrium

In the methodology followed here, the V-tail is sized to reach manoeuvrability targets. Now that the centre of gravity position of the current design is known, these manoeuvrability characteristics may be assessed. This aspect is treated here below. After that, the geometrical parameters and the airfoil are selected.

5.8.1 Sizing

The methodology is the following ([16], chapter 6, page 110-113):

- 1^{st} step : required horizontal and vertical tail sizes should be estimated thanks to the tail volume ratio which is a measure of the aerodynamic effectiveness of the tailplane.
- 2^{nd} step : V surfaces should be sized to provide the same total surface area as required for a conventional tail.
- 3^{rd} step : the dihedral angle should be set to the arctangent of the square root of the ratio between the required vertical and horizontal tail areas.

The tail volume coefficients of the current design are defined as follows:

$$c_{HT} = \frac{S_{HT}\ l_{HT}}{\bar{c}_w\ S}, \tag{5.19}$$

$$c_{VT} = \frac{S_{VT}\ l_{VT}}{b_w\ S}, \tag{5.20}$$

where, for a V-tail, one has

$$l_{HT} = l_{VT} = l_T. \tag{5.21}$$

Naturally, this moment arm depends on the position of the tailplane along the fuselage. As a starting point, this moment arm is assumed to be of 16.4 [ft] (45 % of the length of the fuselage for the first iteration).

It can be found in the literature ([16], chapter 6) that for a trainer these coefficients should be approximately the following ones:

Trainers	Fighters
$c_{HT} = 0.70$	$c_{HT} = 0.40$
$c_{VT} = 0.06$	$c_{VT} = 0.07$

Table 8: Typical tail volume ratios for trainers and fighters.

Notice that the value for c_{HT} is largely different for a trainer than for a fighter. Since the Coyote is an advanced trainer, it should probably exhibit an hybrid value between 0.5 and 0.6.
Knowing the wing surface area and an estimate of the moment arm l_T, one is able to compute the required horizontal and vertical tail surfaces for the current design. Thus, the total surface area of the V-tail can be found as well as the dihedral angle.

$$S_T = S_{HT} + S_{VT}, \tag{5.22}$$

$$\Gamma_T = \arctan\left(\sqrt{\frac{S_{VT}}{S_{HT}}}\right). \tag{5.23}$$

It should be mentioned that, for the sake of simplicity for subsequent iterations, the value of the moment arm will not be updated in this procedure. Consequently, the sizing of the tail only depends on the design of the wing. For each iteration however, it must be checked that the tail volume ratios lie within the intervals denoted in Tab. 8.

5.8.2 Aspect ratio, taper and sweep angle

First, the typical tail AR and taper ratios λ for fighters found in the literature ([16], chapter 4, page 76) are set up in Tab. 9.

Fighters	
Horizontal	Vertical
AR = 3-4	AR = 0.6-1.4
λ = 0.2-0.4	λ = 0.2-0.4

Table 9: Typical tail AR and taper ratios for jet fighters.

Because the V-tail is more similar to a horizontal tail than a vertical fin, it has been decided to chose an AR_T equal to 3.2 and a taper ratio λ_T of 0.3. Then, the sweep angle at leading-edge $\Lambda_{T,LE}$ is usually taken 5 degrees higher than the wing sweep in order to avoid shock waves. Thus, a leading-edge sweep angle of 40 degrees is selected.

5.8.3 Airfoil selection

It is naturally important to choose an airfoil profile for the empennage. Symmetric airfoil for the tail are generally selected for easier control (zero lift at zero A.o.A.). Thus, the airfoil will not present any camber. Although the airfoil for the tail is often selected smaller than that of the wing, experimental results could only be found about a 0.06 thickness ratio airfoil. Since the aircraft is likely to fly in supersonic regime, a NACA 6-series or 6A-series airfoil seems to be more adapted.
Finally, the NACA 64A006 airfoil is selected. Thanks to different documents ([2],[10]), it is possible to determine the lift curve slope of the airfoil (2D) and then to convert it in the 3D case by means of the same formulas used for the wing in section 5.3.

5.8.4 Aerodynamic coefficients for a V-tail configuration [15]

Due to the dihedral of the tail, some adaptations must be brought to the tail lift curve slope. What is given after the computation of the 3D lift curve slope is C_{LT,α_N}, which is the slope of the tail lift curve in pitch measured in the plane normal to each tail panel. It must be transformed into C_{LT,α_t} and C_{YT,β_t} which are respectively the slope of the tail lift curve in pitch measured in plane of symmetry and the slope of tail lateral force curve measured normal to plane of symmetry. Those coefficients are more relevant in order to perform the stability analysis.
Those are linked by the following equations:

$$C_{LT,\alpha_t} = C_{LT,\alpha_N} \cos^2\left(\Gamma_T\right), \tag{5.24}$$

$$C_{YT,\beta_t} = -KC_{LT,\alpha_N} \sin^2\left(\Gamma_T\right). \tag{5.25}$$

Note that K is the ratio of sum of lifts obtained by equal and opposite changes in angle of attack of two semispans of tail to lift obtained by an equal change in angle of attack for the complete tail. Indeed, when the tail is yawed, equal and opposite span load distributions overlap so that it decreases the lift coefficient.

5.8.5 Enforcing equilibrium

One of the purpose of the tail is to enforce equilibrium. Only the equilibrium in pitch is discussed in details here. Dividing the expression of the rotation balance in pitch by the dynamic pressure

times the surface of the wings allows to retrieve the overall non dimensional moment coefficient of the aircraft (nose-up moments are considered positive):

$$C_m = C_{m_0} + C_{Lw}\frac{x_{cg} - x_{ac,w}}{\bar{\bar{c}}} + C_{mT} - C_{LT}\frac{S_T l_T}{\bar{\bar{c}}S}. \tag{5.26}$$

In this equation, the position of the a.c. may be approximated at first as the quarter-chord of the M.A.C. at first in subsonic. It will be evaluated more accurately for different flow conditions in section 6. The longitudinal balance is ensured by specifying that this overall moment coefficient should be equal to zero. Note that the airfoil selected for the tail being symmetric, it induces no concentrated moment and C_{mT} is equal to zero in this equation. A large offset between the C.o.G. and the a.c. of the wing is not convenient for stability reasons. The wing lift induced moment is thus generally not large. The moment coefficient of the wing at the a.c. C_{m_0}, however, is of significant magnitude and is negative (nose down) for the wing design selected here. Since the same airfoil is used along the entire span, the moment coefficient of the wing is that of the airfoil. The latter may be approximated by the moment coefficient at the quarter chord (for subsonic flight) that may be measured on the curves in Fig. 5: C_{m_0} is approximately equal to -0.40 for A.o.A. in $[-4; 8]$ [deg]. Equilibrium may thus only be restored by a tail generating a down-force. The deflection angles of the control surfaces or the angle of incidence of the entire V-Tail must be adapted in unison to provide the required down-force.
This also impacts the design of the wing since it must be able to counter this additional down-force, on top of the weight (it may amount to about 10 % of the weight in cruise !).

5.8.6 Final geometry

Here is compiled the geometrical parameters of the V-tail. Note that the dihedral angle Γ_T has been increased from the 32 [°] predicted by Eq. 5.23 to 40 [°] by fear that yaw control could not be achieved with such a small value.

V-tail parameters	
Surface: S_T	113.9 [ft^2] (10.6 [m^2])
Aspect ratio: AR_T	3.2
Taper ratio: λ_T	0.3
Sweep angle (LE): $\Lambda_{T,LE}$	40 [°]
Span: b_T	19.10 [ft] (5.82 [m])
Chord at root: $c_{T,root}$	9.18 [ft] (2.80 [m])
Chord at tip: $c_{T,tip}$	2.75 [ft] (0.84 [m])
Dihedral angle: Γ_T	40 [°]
Moment arm of the tail: l_T	14.30 [ft] (4.36 [m])

Table 10: Numerical values of the V-tail parameters.

5.9 Landing gear design

A common trycicle configuration is selected here. According to [5], such a configuration allows easier manoeuvring on the ground, which is desirable for a jet fighter. It also provides good visibility and stability on the ground since the centre of gravity is ahead of the main wheels, which prevents the event of nosing over with more reliability.

Raymer provides guidelines for a correct positioning of the landing gear in [16], chapter 11. These are as follows, with the notation described in Fig. 12:

- The tipback angle θ (angle such that the tail of the static aircraft wound touch the ground) should allow for large A.o.A. amplitudes at take-off and landing. A deliberately large value of 15 [deg] is selected here.
- The angle of the line joining the main wheels to the farthest aft C.o.G. should be larger than the tipback angle.
- The nose strut should ideally have a 7 [deg] inclination.
- The following indicators may be used to ensure a proper fraction of the weight is supported by the nose wheel:

$$\frac{M_a}{W_{base}} > 0.05 \ (> 0.08 \text{ ideally}) \qquad \frac{M_f}{W_{base}} < 0.20 \ (< 0.15 \text{ ideally}). \tag{5.27}$$

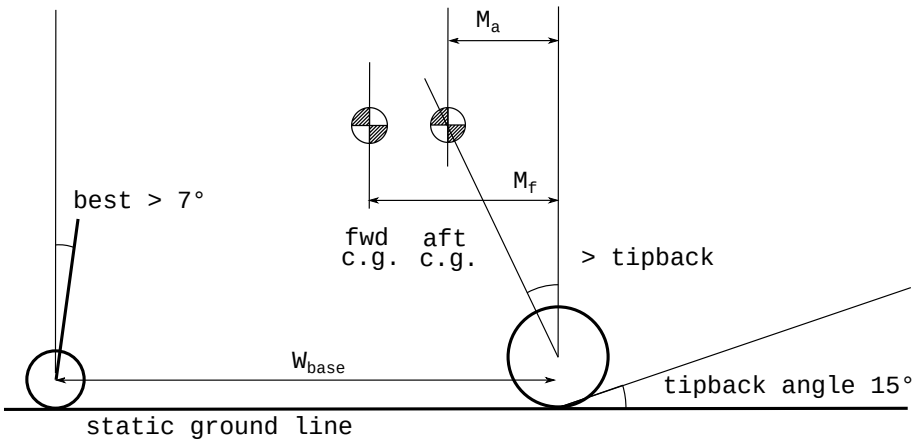

Figure 12: Tricycle wheels geometrical description (reproduced from [16], chapter 11).

The wheel track W_{track} may be selected such that the maximum roll angle ϕ (the roll angle at which the wing tip of the static aircraft touches the ground) is sufficiently large (25 [deg] is selected here).

Then, a proper design of the tires ensures that the wheels are able to carry the weight of the aircraft. The nose tire is set to carry about 10 % of the load while the main gear tires carry about 90 % of it. TYPE VII tires will be used, as they are widely used for jet aircraft. Those are high pressure tires, which is fitting for higher landing speeds. A quick design method based on statistics and the weight applied on each wheel provided in [16], chapter 11 allows to define the dimensions of tires. Their value for the final iteration are compiled in Tab. 11.

Tire sizing	
Main wheel diameter	31.69 [in] (0.8 [m])
Main wheel width	10.02 [in] (0.25 [m])
Nose wheel diameter	16.32 [in] (0.41 [m])
Nose wheel width	10.02 [in] (0.25 [m])

Table 11: Aircraft tire dimensions.

Geometry summary	
W_{track}	5.6 [ft]
W_{base}	17.2 [ft]
Max. roll angle ϕ	25 [°]
Tipback angle θ	15 [°]
Height of the wing h_w	5.6 [ft]

Table 12: landing gear geometry summary.

Rendered views of the nose and main landing gears in their deployed and retracted configurations are displayed in Fig. 13.

Figure 13: Rendered view of the nose and main landing gears in their deployed (left) and retracted (right) configurations.

6 Aerodynamic study

The aerodynamics of the Coyote have been crudely estimated with statistical methods in the early stage of the design. Once the geometry of the wing and of the tail are frozen, more advanced tools may be used to increase the accuracy of the aerodynamic study. In particular, two separate tools are used in this analysis:

- The **Component Buildup Method** (CBM) described by Raymer in [16], chapter 12: an empirical method that allows to estimate the individual participation of each component to the zero-lift drag of the aircraft.

- The software **Tranair**: a full potential equations solver over arbitrary 3D geometries. It has the capability to account for weak shocks and viscous effects by coupling the inviscid problem with the boundary layer equations (through the use of a blowing velocity). Tranair is then adapted to evaluate the forces and moments applied on the wing and on the tail of the trainer in subsonic and transonic conditions at moderate computation cost. This solver is however limited to attached flows and to subsonic to low supersonic free stream velocities ($M_{\text{inf}} < 1.3$).

6.1 Methodology

Three different flow conditions are studied in this analysis:

- Take-off & landing: 1,000 [ft] and 0.3 M,
- Cruise: 35,000 [ft] and 0.8 M,
- Dash: 35,000 [ft] and 1.2 M.

For each of these conditions, the lift and drag forces of the aircraft are investigated and the position of the a.c. of the wing together with the static stability margins are re-estimated.
In the characterisation of the lift force, only the wing is studied in Tranair. The participation of the tail is accounted for such that equilibrium is enforced but not actually simulated. The participation of the fuselage to the lift is here ignored.
In the study of the drag force, the complete (induced and parasite drag) participation of the wing is simulated with Tranair. The participation of the fuselage, the air intakes and the canopy to the parasite drag are assessed with the CBM. The participation of the tail to the parasite drag is estimated using Tranair but its induced drag is neglected (it is indeed small, and would necessitate to know the wing moment coefficient in pitch for any C_{Lw}).
Note that the aerodynamics of the Coyote during manoeuvres is not studied here because of the difficulty to deal with high A.o.A. (and thus partially separated flows) in Tranair. In addition, capturing the vortex flow induced by the LEX is beyond the scope of this analysis. The wing is thus modelled without LEX.

6.2 Component Buildup Method

The *Component Buildup Method* (CBM) is a method used to analytically determine the parasite drag of the aircraft. Described in [16] it is based on the addition of the participation to the drag of several parts of the aircraft. A friction coefficient may be associated to each component and then multiplied by its wetted area to yield the corresponding drag. Two additional factors will also appear as weight factors. The induced drag of the wing and of the tail must also be accounted for. A brief description of the method is detailed hereafter.
Three cases must be considered in terms of Mach number:

- Subsonic speed: M is equal to 0.8 or lower,
- Supersonic speed: M is equal to 1.2 or higher,
- Transonic speed: M is between 0.8 and 1.2.

The corresponding parasite drag is calculated in a different manner depending on the case.

6.2.1 Subsonic parasite drag

The CBM in subsonic is composed of three terms. The first one is the drag due to the flat-plate skin-fiction of each component of the aircraft. The second represents the miscellaneous drag $C_{D_{misc}}$ and the last one the drag due to leakages and protuberances $C_{D_{L\&P}}$.
The skin-friction term is simply the product of the friction coefficient of the component C_{f_c}, a form factor FF_c, an interference factor Q_c and the wetted area of the component S_{wet_c}. The subscript index $_c$ denotes the component. The whole term is then divided by S the reference area of the wing: 269 [ft^2].
The form factor approximates the pressure drag due to viscous separation and the interference factor represents the effect of the shape of the component on the drag or the mutual interference between components. The total flat-plate skin-friction drag is thus the addition of the drag of each components. Tab. 14 compiles all the factors used to computed the C_{D_0} at 0.8 M and 35000 [ft].

The components included in this analysis are the wing, the tail, the fuselage, the canopy and the inlets. The total parasite drag of the aircraft may then be calculated as:

$$C_{D_{0_{subsonic}}} = \frac{\sum_c (C_{f_c}\ FF_c\ Q_c\ S_{wet_c})}{S} + C_{D_{misc}} + C_{D_{L\&P}}, \tag{6.1}$$

where the subscript c spans the five components mentioned above.
The miscellaneous participation embodies the influence of flaps deflection, landings gears or any special features that could produce even more drag when the flow will encounter them. Note that it will be zero as neither flaps, neither landing gears nor any other special feature are out in cruise condition.
The leakage and protuberance drag is, as the name suggests, what a leak can produce or the effects of protuberances. As the air will flow through tiny holes inside the aircraft in high pressure zones and outside in low pressure zones the leaks will absorb some momentum by *inhaling* the air and generate more airflow separation by *exhaling* the air, both increase the drag.
The C_{f_c} of each component depends on many variables as the Reynolds number, the percentage of laminar flow, the characteristic length of the component, etc. For each part of the plane, a laminar and a turbulent skin-friction coefficient will be computed (see Eq. 6.2 from [16]) and C_{f_c} is then the weighted average between them. The weight is given by the percentage of laminar flow. This percentage is set to 10 [%], which is conservative (this value is given in [16]).

$$\text{Laminar:} \quad 1.328/\sqrt{R} \qquad \text{Turbulent:} \quad \frac{0.455}{(\log_{10} R)^{2.58}\ (1+0.144M^2)^{0.65}} \tag{6.2}$$

The Reynolds number in this formula is either the conventional Reynolds or a corrected version as calculated with Eq. 6.3 depending on which is the lowest. The corrected Reynolds attempts to represent as much as possible the effects of the skin-roughness of the component. The l stands for the characteristic length of the component and k the skin-roughness value taken from empirical data in Tab. 13. k is fixed to 1.33 10^{-5}, the value for a production sheet metal.

$$\text{Subsonic:} \quad R_{cutoff} = 38.21\ (l/k)^{1.053} \quad \text{Supersonic:} \quad R_{cutoff} = 44.62\ (l/k)^{1.053}\ M^{1.16} \tag{6.3}$$

Surface	k [ft]
Camouflage paint on aluminium	3.33 10^{-5}
Smooth paint	2.08 10^{-5}
Production sheet metal	1.33 10^{-5}
Polished sheet metal	0.50 10^{-5}
Smooth molded composite	0.17 10^{-5}

Table 13: Empirical values for the skin roughness value (taken from [16]).

	Q	FF	C_f
Wing	1	1.3602	0.002502
Tail	1.03	1.3505	0.002611
Fuselage	1	1.1172	0.001902
Inlets	1	1.1222	0.002358
Canopy	1	1.9030	0.002241

Table 14: Summary of the coefficients intervening in the computation of C_{D_0} for the different components of the aircraft.

Concerning the interference factor Q, one may observe that only the tail has a Q different of 1. This is a consequence of the V-tail configuration of the aircraft. When considering the form factor FF, there are three groups. The wing and the tail have both a coefficient around 1.35, the fuselage and the inlet around 1.12 but the canopy coefficient is much larger. The reason for this increase is the form of the canopy. As it is a two-seater, the Coyote has a two-pieces canopy with a fixed streamlined windshield which yields a greater FF than a one-piece canopy.
Indeed, the flow will follow the clean aircraft whitout facing more outgoing parts. Furthermore, $C_{D_{L\&P}}$ is approximated to 15 [%] of the total sum of the skin-friction drag of all the components.

The wetted area of each component is displayed in Fig. 14. The main term is the wetted surface of the fuselage closely followed by the wing. Yet, in Fig. 15 the major drag coefficient comes from the wing. This is due to the C_f and the FF of the wing that are respectively 131.58 % and 121.75 % of the C_f and FF of the fuselage (see Tab. 14). The C_{D_0} computed with this method for the fuselage, the canopy and the inlets can be found in Tab. 16 in column $C_{D0,others}$.

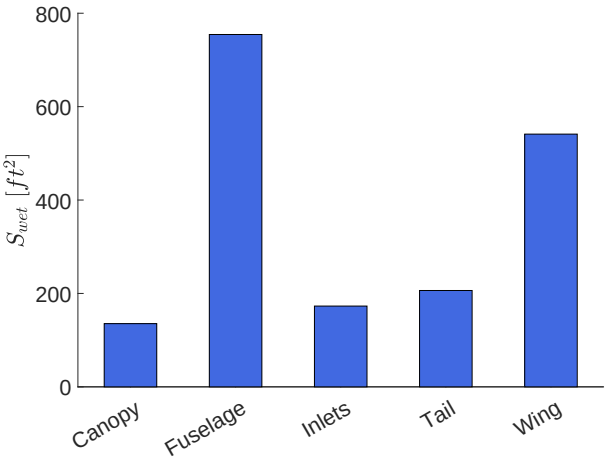

Figure 14: Distribution of the wetted area of each component.

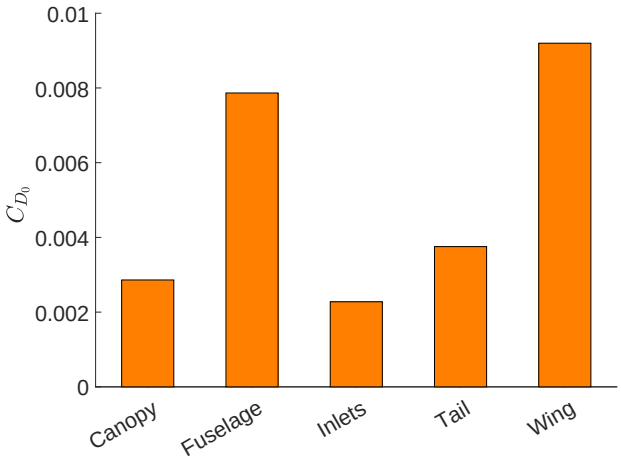

Figure 15: Distribution of the C_{D_0} of each component at 0.8 M and 35000 [ft].

6.2.2 Supersonic parasite drag

For the supersonic parasite drag, the procedure is identical with the exception that C_{D_0} is now computed using Eq. 6.4 i.e. without the FF nor the Q and with a wave-drag term, $C_{D_{wave}}$. Again, $C_{D_{misc}}$ is assumed to be zero.

$$C_{D_{0_{supersonic}}} = \frac{\sum_c \left(C_{f_c}\ S_{wet_c}\right)}{S} + C_{D_{misc}} + C_{D_{L\&P}} + C_{D_{wave}}. \tag{6.4}$$

The term $C_{D_{wave}}$ is computed using Eq. 6.5 where A_{max} is the maximal cross section area and l the length of the aircraft. E_{wd} is the empirical wave-drag efficiency factor set to 2 to be conservative (value taken from [16]).

$$C_{D_{wave}} = \frac{E_{wd}}{S}\left[1 - 0.386\ (M-1.2)^{0.57}\ \left(1 - \frac{\pi\Lambda_{LE}^{0.77}}{100}\right)\right]\ D_{SH}, \tag{6.5}$$

with

$$D_{SH} = \frac{9\pi}{2}\left(\frac{A_{max}}{l}\right)^2. \tag{6.6}$$

Again, the C_{D_0} computed with this method for the fuselage, the canopy and the inlets can be found in Tab. 16 in column $C_{D0,others}$.

6.2.3 Transonic parasite drag

Computing a C_{D_0} analytically in transonic is not possible. The graphical alternative proposed by Raymer in [16] is to connect the C_{D_0} at 0.8 M to the C_{D_0} at 1.2 M with the curve displayed in Fig. 16. This curve is drawn trough different key-points. The following simplifications are made: B is equal to A, C is 50 % of A and D is 0.002 by definition. E is zero at M_{cr} which is around M_{DD}-0.08.

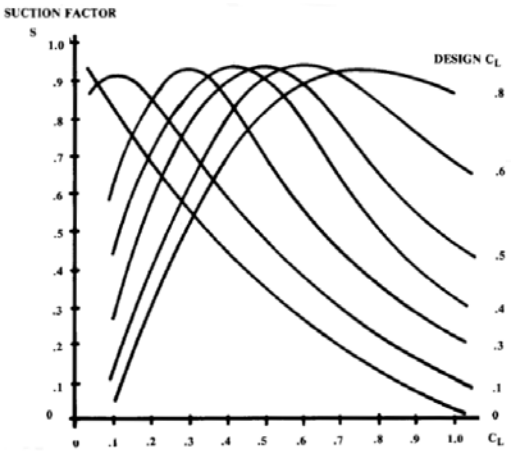

Figure 16: Leading edge suction factor for several C_L ([16], page 303).

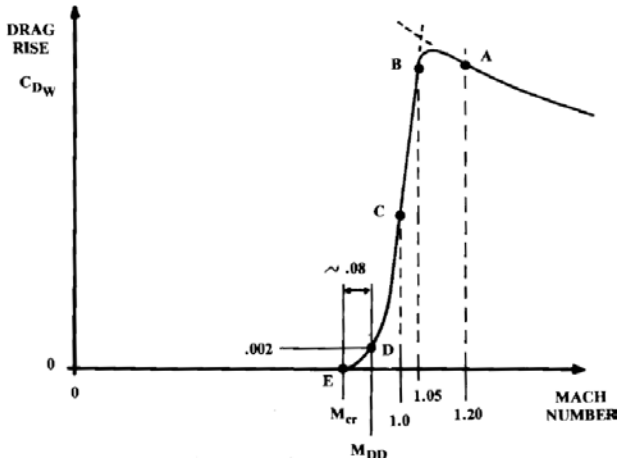

Figure 17: Transonic drag rise estimation ([16], page 296).

6.2.4 Induced drag

The induced drag of the wing and the tail may be computed with the Leading-Edge-Suction Method from [16] with Eq. 6.7.

$$C_{D_i} = K \cdot C_L{}^2. \tag{6.7}$$

The method is based on the *suction* generated by the pressure distribution on the wing. K is the drag due to lift factor and is computed as a weighted average of two extreme cases as:

$$K = Sp\ K_{100} + (1 - Sp)\ K_0. \tag{6.8}$$

If there is a 100 % leading-edge suction as in the d'Alembert's paradox, K will be equal to $K_{100} = \frac{1}{AR\ \pi}$. On the opposite if there is zero leading-edge suction K will be equal to $K_0 = \frac{1}{C_{L_\alpha}}$. Sp then represents this leading-edge suction percentage. This is a good approximation for subsonic speeds. Sp behaviour is described in Fig. 17 for a design $C_{L,w}$ of 0.4 for the wing and a design $C_{L,T}$ around 0.1 for the tail. At Mach number above 1.2, Sp will be 0 %. For the transonic regime, Sp will smoothly tend to 0 % from the value taken in the subsonic regime.

For level flight at 0.8 M at 35000 [ft] and at 50 [%] of fuel, the C_{D_i} of the wing and the tail are shown in Fig. 18 in orange. Note that the induced drag of the tail is so low because as only the necessary down-force to maintain equilibrium is small with respect to the lift force of the wing. Fig. 18 displays the participation of each component to the total drag coefficient of the aircraft in cruise conditions. For other Mach numbers or altitudes, exactly the same method may be used with some modifications in the parameters as the air density or the dynamic viscosity.

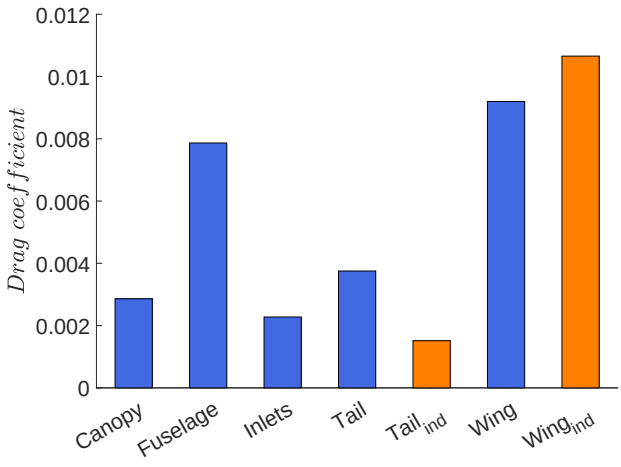

Figure 18: Contributions to the drag of each component at 0.8 M and 35000 [ft] at 50 [%] of fuel. The orange bars represents the induced drag participation.

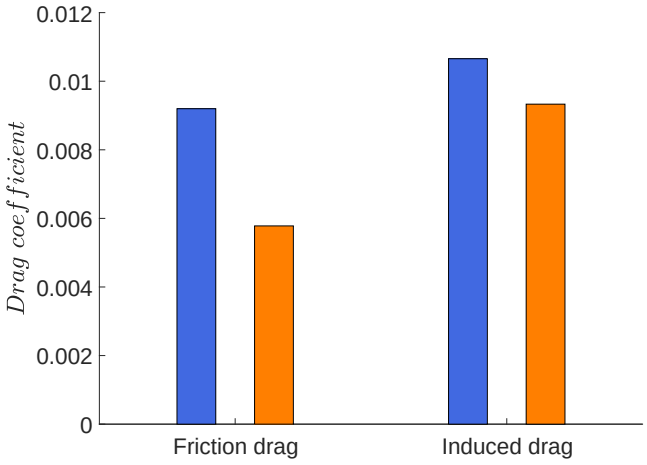

Figure 19: Comparison between the friction and induced drag of the wing calculated with the CBM method (in blue) and with Tranair (in orange) for 0.8 M, 35000 [ft] and 50 [%] fuel.

6.3 Tranair

6.3.1 Qualitative results

It may be interesting to first look at the solution computed with Tranair on a qualitative point of view. The pressure coefficient ($C_p = \frac{p-p_\infty}{\frac{1}{2}\rho_\infty V_\infty^2}$) distribution around the M.A.C. in cruise conditions at 50 % fuel is displayed in Fig. 20 (a). As expected, the pressure on the extrados is lower than on the intrados, resulting in a net lift force. One may also observe the presence of a typical suction peak at the leading edge. Fig. 20 (b) denotes the lift distribution along the half-span for level flight at 50 % fuel and three flow conditions. A usual elliptic-like distribution is obtained here. At high speed (dash), the position of maximum lift is shifted outboard.

The identification of shocks is also of primary importance. Tranair allows to compute the local Mach number distribution around the wing and the tail, as displayed in Fig. 21 for two free-stream Mach numbers (a) 1.2 M (b) 0.8 M, 35,000 [ft] and 2.5° A.o.A.

For the supersonic free-stream (Fig. (a)), one may notice that a bow shock develops upstream of the leading edge, which is expected for rounded leading edge such as that of the NACA64-206 selected for the wing. The flow then stagnates on the leading edge before accelerating (more moderately on the intrados than on the extrados). Two oblique shocks develop at last on the trailing edge in a usual

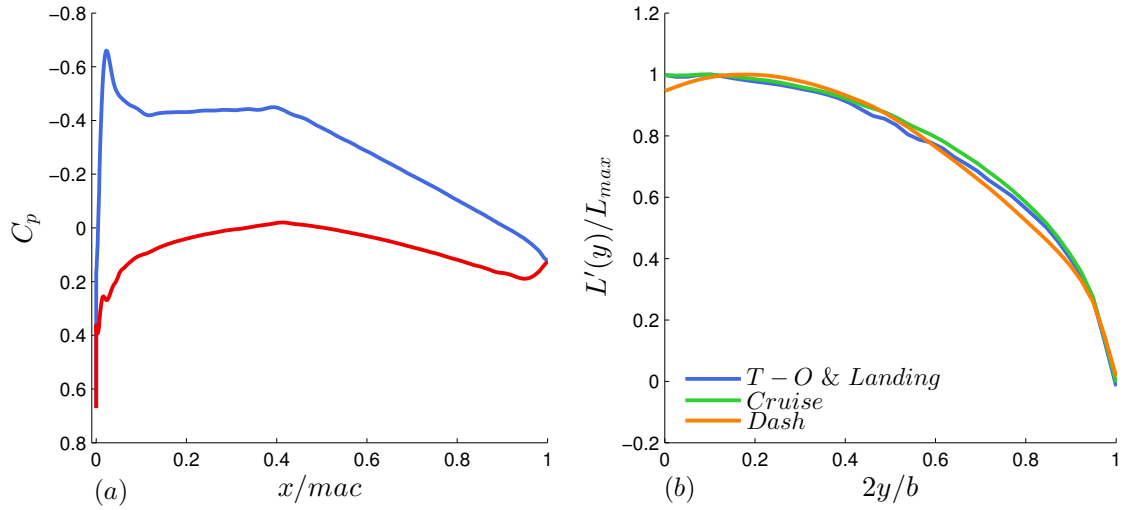

Figure 20: (a) Pressure coefficient distribution around the m.a.c for level flight at 50 % fuel, 0.8M and 35,000 [ft]. (b) Lift per unit span distribution along the half span for level flight at 50 % fuel and three flow conditions.

fishtail pattern. A bow shock also develops upstream of the tail, but only near the tail root. No shock seems to occur at the trailing edge of the wing.

For the subsonic free-stream, no shock develops on the wing nor on the tail. This is a consequence of the thin airfoils selected for the Coyote (6% thickness ratio).

6.3.2 Wing lift curve and drag polar

Two features of the wing are of primary interest and may be assessed with Tranair: the wing lift curve slope and the wing drag polar. As the wing is slightly cambered, these are defined as:

$$C_{Lw} = C_{Lw,\alpha}\left(\alpha - \alpha_0\right), \tag{6.9}$$

$$C_{Dw} = C_{D0,w} + \frac{\left(C_{Lw} - C_{Lw,min_D}\right)^2}{e\pi AR_w}. \tag{6.10}$$

Fitting the results obtained with Tranair with a linear and a quadratic polynomial respectively allows to retrieve estimates of the parameters intervening in these expressions. The numerical results together with the fits for the three different flow conditions are depicted in Fig. 22. One may observe that the fits seem to approximate accurately the numerical results. As expected, the lift curve slope is smaller at low speed than during cruise and the dash. Also notice the significant increase in parasite drag from subsonic to supersonic due to the development of shocks. The corresponding parameters are compiled in Tab. 16. Notice that the lift curve slope obtained with Tranair in cruise is higher than that calculated empirically with Eq. 5.10. This may result in a slight increase in $C_{Lw_{max}}$ compared to the value displayed in Tab. 3. The zero lift angle in cruise is also very close to that estimated in

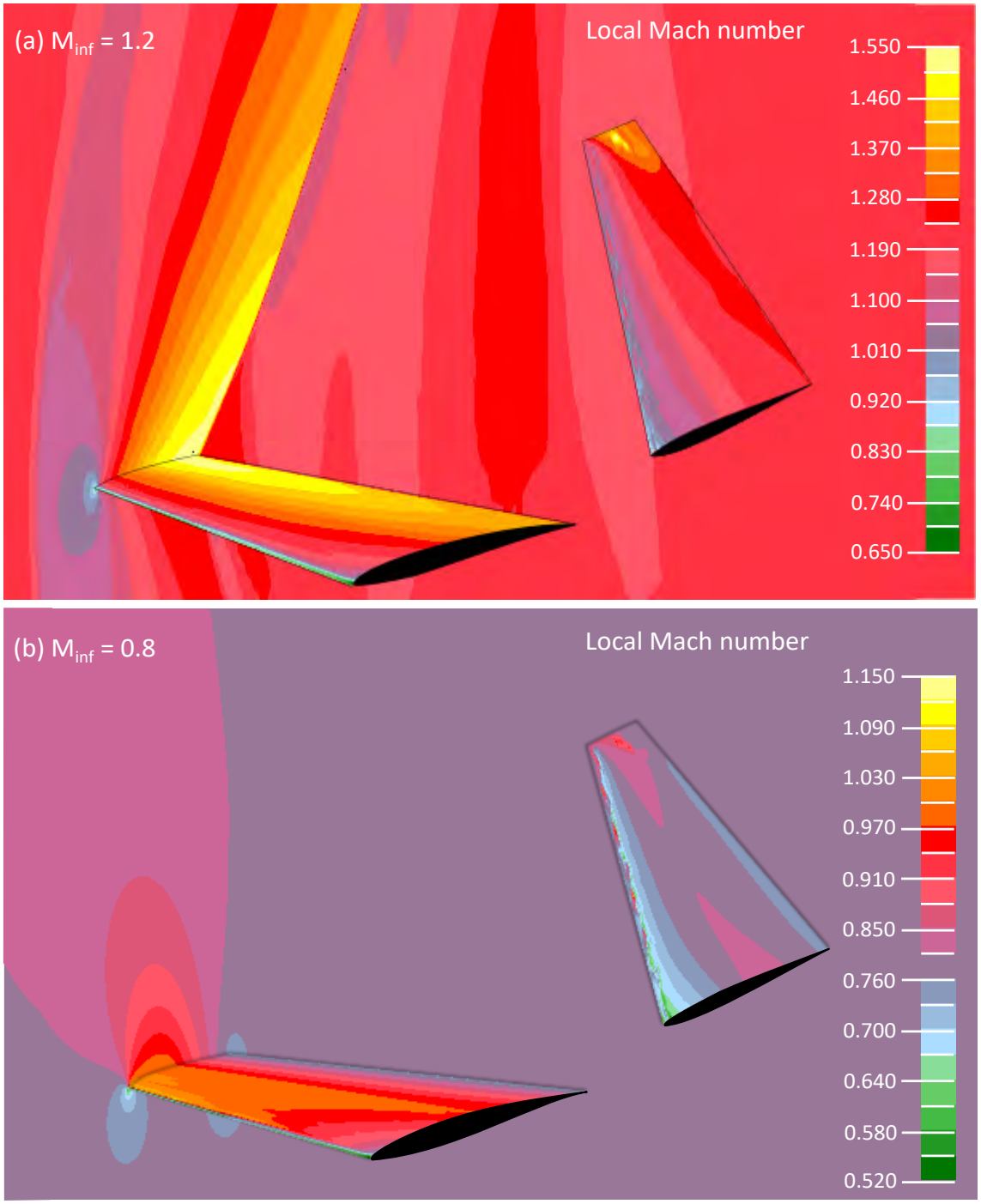

Figure 21: Mach number distribution obtained with Tranair on the wing and the tail for a free-stream Mach of (a) 1.2 (b) 0.8.

section 5.3 (-1.1 compared to -1.17 [°]).

Note that a similar approach for the V-tail allows to characterise its participation to the parasite drag. This participation is rendered non dimensional by dividing the tail parasite drag force by the dynamic pressure and the surface of the tail. If $C_{D0,T}$ is to be added to the rest of the parasite drag of the Coyote, it must then be multiplied by $\frac{S_T}{S}$.

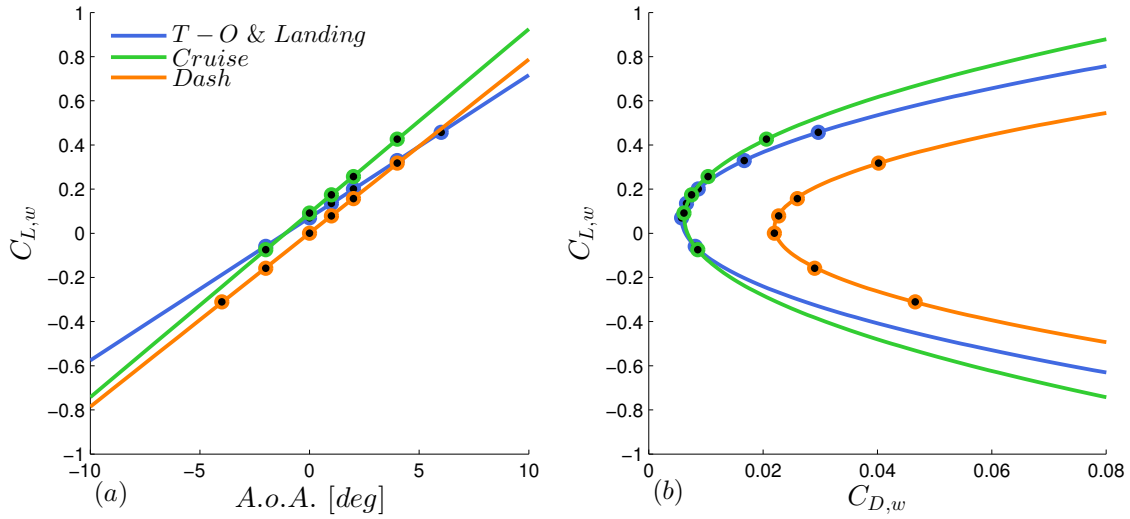

Figure 22: (a) Fit of the lift curve slope of the wing from Tranair cases for three flow conditions. (b) Fit of the drag polar of the wing from Tranair cases for three flow conditions.

6.4 Aerodynamic centre of the wing

The position of the a.c. of the wing plays a crucial role in the stability of the aircraft. It is thus interesting to assess its position with Tranair. It is defined as the point such that the pitching moment around it is constant with the A.o.A. A simple 2D formula may be obtained by first specifying that the overall moment around any point of the wing (here, the leading edge of the M.A.C.) is independent of the point of application selected for the lift force:

$$M_{ac} - x_{ac}L_w = M_{ref} - x_{ref}L_w \qquad \text{(nose up moments taken positive)}, \tag{6.11}$$

where x_{ref} is an arbitrary reference point. Dividing this expression by $qS\bar{\bar{c}}$, then differentiating it with respect to the A.o.A. and using the definition of the a.c. allows to write:

$$h_{ac} = h_{ref} - \frac{m_0}{a_0}, \tag{6.12}$$

where the positions are expressed as fractions of the M.A.C. and m_0 and a_0 are respectively the wing moment coefficient derivative around the reference point and the wing lift curve slope. The position of the a.c. of the wing may then be evaluating these derivatives with Tranair by finite difference

between two cases with a slightly different A.o.A. Note the fuselage exerts an influence on this a.c. and this effect is not captured in this analysis. The results for three flow conditions and level flight are compiled in Tab. 15. Several observation are worth noting. First, the a.c. position in subsonic appears to be aft of the quarter chord of the M.A.C., which is unusual. As Eq. 6.12 is only 2D, it may result from the fact that the M.A.C. is actually located outboard of that computed geometrically. No conclusion is however drawn here. It is indeed the absolute longitudinal position of the a.c. that is of interest for the stability analysis. Second, one may observe that the a.c. is shifted at about 50 % of the M.A.C. in supersonic conditions, which is a known phenomenon.

	T.-O. & L.	Cruise	Dash
A.c. position : $h_{ac,w}$	0.263	0.290	0.482

Table 15: Position of the aerodynamic centre of the wing (as a fraction of the M.A.C) for three flow conditions and for level flight. Assessed with Tranair viscous cases.

6.5 Tools comparison

It may be interesting to briefly compare the results obtained with the CBM and Tranair. Fig. 19 compares the friction and induced drag coefficient of the wing assessed with the CBM to those computed by Tranair. It clearly shows that the induced drag of the wing with the CBM is larger than that obtained with Tranair, as for the friction drag. A reason for the difference in friction drag may be explained by the conservative value selected for the percentage of laminar flow in the CBM or in the k value used to compute the C_f.

As the CBM is general and based on empirical relations, the results obtained with Tranair are likely more accurate. For the estimation of useful drag characteristics for the design of the Coyote, the CBM will only be used when necessary. The methodology followed here for the drag study of the complete aircraft is detailed in section 6.1.

6.6 Aircraft total drag

Assuming that only the wing participates to the lift induced drag, the drag polar of the entire aircraft may be obtained by adding the parasite drag of tail obtained with Tranair and that obtained with the CBM for the fuselage, the canopy and the inlets to the wing drag polar. The resulting drag polar is depicted in Fig. 23 and compared to the polar used in the pre-design ($e = 0.75$, $C_{D0} = 0.022$). One may observe in this figure and in Tab. 16 that the preliminary drag polar used for the early drag estimates was barely conservative for the subsonic parasite drag, and not conservative for Oswald's

factor e.

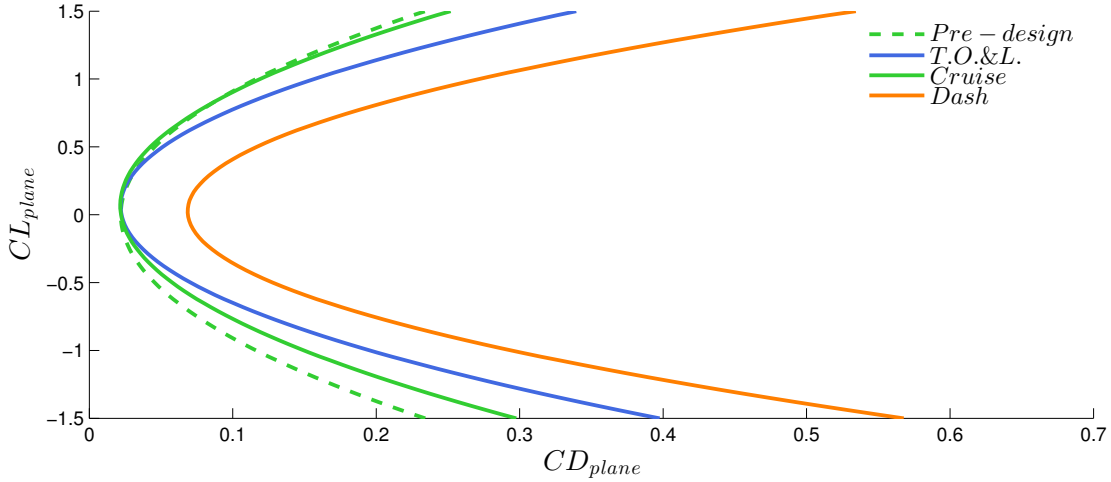

Figure 23: Total drag polar of the entire aircraft for three flow conditions. Reconstructed from results obtained with Tranair and the CBM. The dashed polar corresponds to that used during the pre-design.

	$C_{Lw,\alpha}$ [rad$^-$1]	α_0 [deg]	$C_{D0,w}$	e	C_{Lw,min_D}	$C_{D0,T}$	$C_{D0,others}$	$C_{D0,plane}$
T.-O. & Landing	3.70	-1.5	0.0058	0.46	0.063	0.0055	0.0137	0.0219
Cruise	4.78	-1.1	0.0063	0.63	0.068	0.0055	0.0130	0.0216
Dash	4.50	0.0	0.0220	0.33	0.026	0.0109	0.0420	0.0686

Table 16: Summary of the aerodynamic parameters of the wing, the Tail and of the rest of the Coyote obtained with Tranair and the CBM.

6.6.1 Maximum Mach and L/D diagram

The lift to drag ratio for level flight at 36,000 [ft] and 50 % fuel weight as a function of the Mach number may be assessed with Tranair and the CBM as displayed in Fig. 24 (b). Note that the stall line is here drawn for an approximate $C_{L,plane_{max}}$ of 1.2. Once again, the participation of the fuselage, the canopy and the inlets are assessed with the CBM. The methodology followed to assess the drag associated to the wing and the tail with Tranair is however worth detailing.

The total drag associated to the wing may be approximated with Tranair for level flight. Running then a case for the tail separately so that it produces the necessary down-force to maintain equilibrium allows to account for its participation to the total drag. Note that the down-force is here produced by varying the A.o.A. seen by the entire tail, not by deflecting the rudder as it is actually the case in subsonic. It seems reasonable to assume that it affects mostly the form drag, which is anyway small for streamlined bodies.

The total drag force experienced by the aircraft is then compared with the available thrust with full afterburner corrected for altitude and Mach number with Eq. 5.17. One may clearly notice in Fig. 24 (b) the drag rise starting at about 0.8 M. The maximum Mach number corresponds to the Mach number at which the excess thrust $(T - D)$ reaches zero:

$$M_{max} = 1.5, \text{ approximately (full A/B)}. \tag{6.13}$$

This is the maximum Mach number on a thrust point of view. The structure of the Coyote however will only be designed for the dash speed specified in the objectives: 1.2 M to avoid a costly over-design. In addition, it should be stressed that this result is only a rough approximation and should be regarded with the appropriate caution for the following reasons. First, the validity of the solution computed by Tranair is limited to weak shocks, which correspond to free stream velocities below 1.3 M approximately. Second, the range of validity in terms of Mach number of Eq. 5.17 is not known. Only manufacturers data-sheets may provide the necessary pieces of information for an accurate available thrust evaluation.
This analysis however shows that, with this current estimation, the Coyote is able to go through the transonic to reach the objective dash speed of 1.2 M.

Fig. 24 (a) denotes the evolution of the lift to drag ratio of the aircraft as a function of the Mach number for level flight at 36,000 [ft] and 50 % fuel weight. A maximum ratio of about 13 is reached a little bit before 0.7 M. At the cruise Mach number of 0.8, the ratio still reaches a descent value of 11. The ratio then drops abruptly when entering the transonic region before adopting a steady decrease rate above 1.1 M.

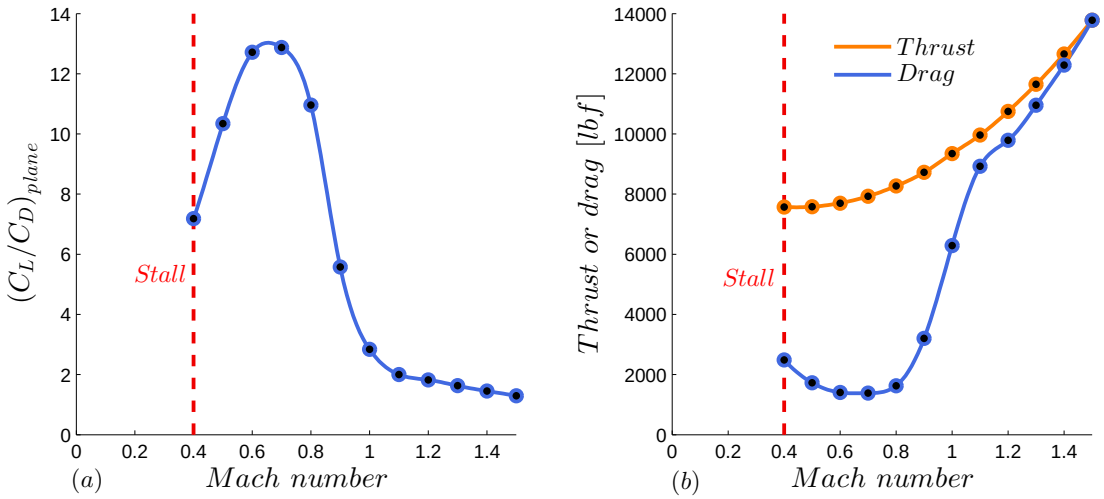

Figure 24: (a) Lift to drag ratio as a function of Mach number for level flight at 36,000 [ft] and 50 % fuel weight. (b) Total drag force and available thrust (full A/B) as functions of Mach number for level flight at 36,000 [ft] and 50 % fuel weight.

7 Structure design

At this stage, the integrity of the aircraft's structure for any flight conditions contained within the flight envelope must be verified. Within this frame, the critical flight conditions must first be determined and the loads applied on the plane must then be assessed for each case.

In this section, only the reaction stresses at the section of the fuselage just aft of the wing as well as the ones at the wing at the root are considered. Indeed, these sections are subjected to the largest reaction forces and moments due mainly to the weight of the engine and the aerodynamic loads acting on the tail for the fuselage section and due to the lift distribution for the wing root section. Therefore, if these sections withstand the applied loads, the rest of the aircraft should also resist.

7.1 Flight envelope

To begin with, the manoeuvre envelope is drawn in blue in Fig. 25. It depicts the load factor that can be safely reached by the aircraft as a function of the equivalent speed at the altitude of 15,000 ft during the mission (altitude of the manoeuvres - see the design mission in Fig. 1). The envelope was computed considering a maximum lift coefficient equal to 1.2 and a design mach number of 1.22. In this graph, one can read that the minimum equivalent speed to avoid the stall in cruise V_{s1} is 118 knots and the design cruise speed V_C is approximately 480 knots (it corresponds to a Mach number of 1.22 and it is computed considering the use of the afterburner). This large difference between these two speeds gives a large range of manoeuvrability which is clearly attractive. Moreover, the maximum

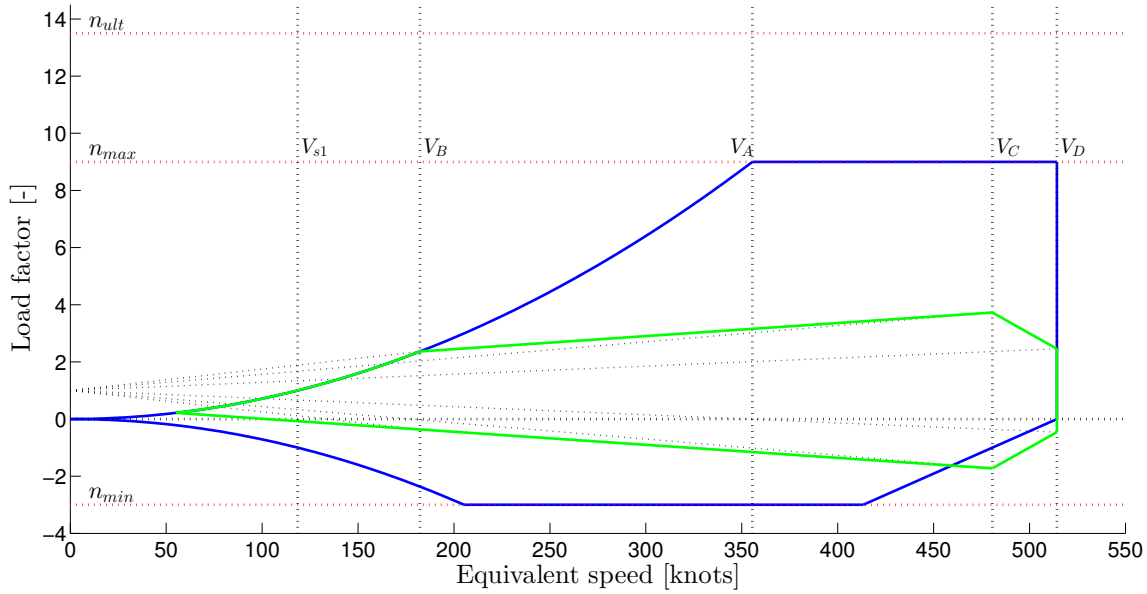

Figure 25: Manoeuvre envelope (blue) and gust envelope (green) at 15,000 ft during manoeuvres.

speed above which the use of control surfaces is no more allowed (depicted by V_A) is quite high (355 knots), meaning the aircraft remains manoeuvrable even at high speeds.

The envelope in response to a 30 [t/s] equivalent sharp-edged vertical gust is also drawn in Fig. 25, which permits to measure the reduction in manoeuvrability of the Coyote in case of a wind-blast. With this envelope, one assesses that the minimum speed the aircraft may safely enter a turbulent airflow (labelled by V_B) is 182 knots, which reduces by 16 % the range of speeds at which the aircraft can safely fly. To finish with, it is important to highlight gusts will not induce load factor higher than the maximum one for which the structure is designed.

The critical flight conditions of the flight envelope may now be determined. They are listed in Tab. 17.

Case	n	V_{eq} [knots]
A	9	355
C	9	480
D_1	9	515
D_2	0	515
E	-3	417
F	-3	210

Table 17: Critical flight conditions.

7.2 Aerodynamic and structural loading

7.2.1 Aerodynamic forces

Knowing the different critical cases of the flight envelope, an important step is to estimate the aerodynamic forces acting on the different parts of the aircraft. For those flight configurations, the plane should be able to perform a manoeuvre without the structure being overloaded. In order to represent this potential additional loading, an additional pitching acceleration $\ddot{\theta} = 2\pi$ [rad/s^2] and a side-slip angle $\beta = 10$ [°] are considered for each flight configuration. This last one can have different effects : an additional pitching moment and a resulting torque due to the asymmetry of the slipstream on the tailplane. However, these effects are difficult to evaluate (especially for a V-tail) and a CFD analysis of the plane should be performed. For that reason, those effects are neglected in our aerodynamic loads estimation in the framework of a preliminary study.

The loads are then evaluated through a vertical equilibrium and a moment equilibrium around the centre of gravity. The different forces are represented in Fig 26. For a flight configuration corresponding to a stall limit, the angle of attack α is known and the unknowns are thus the equivalent velocity, the lift generated by the wing L and the lift generated by the tail P. On the other hand, for the other flight configurations, it is the equivalent velocity which is known and the unknowns are the angle of attack α, the lift generated by the wing L and the lift generated by the tail P. The other forces are easily evaluated as functions of the angle of attack and/or the velocity.

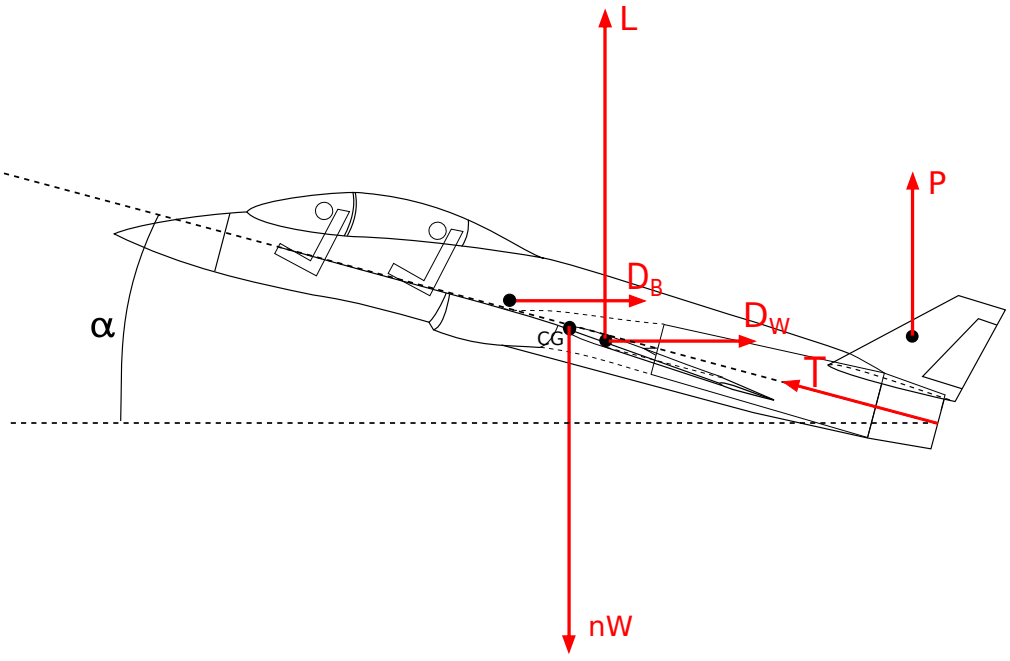

Figure 26: Summary of the aerodynamic forces acting on the aircraft.

The equilibrium equations are the following:

$$L + P + T.sin(\alpha) = nW, \tag{7.1}$$

$$l_L.L + l_{D_w}.D_w + l_{D_B}.D_B + l_P.P + l_T.T + M_w = I_\theta.\ddot{\theta}, \tag{7.2}$$

$$\frac{1}{2}\rho_0 V_{eq}^2 C_{L,\alpha}(\alpha + i_w - \alpha_{L,0})S_w = L. \tag{7.3}$$

The coefficients l_i corresponds to the moment arms of the different forces with respect to the centre of gravity. Note that those coefficients can be negative depending on the direction of the forces.
The results are compiled in Tab. 18. The value M_w corresponds to the pitching moment induced by the wing. D_w and D_B are the drag respectively of the wing and of the body. F_{fin} is the side-force generated by the tail and M_{fus} is the torque applied by the tail on the fuselage. Note that the value of I_θ comes from the CAD model.

Case	A	C	D_1	D_2	E	F
n	9	9	9	0	-3	-3
α [°]	14	3.6	2.7	-3.5	-6.4	-12
L [lbf]	220857	227508	229286	23092	-63955	-60922
P [lbf]	-26143	-31051	-32772	-22505	-661	-2754
F_{fin} [lbf]	-10555	-20811	-23826	-23826	-20811	-4205
M_{fus} [lbf.ft]	-66875	-131861	-150967	-150967	-131861	-26646
D_w [lbf]	23017	28588	25671	1655	3423	4596
M_w [lbf.ft]	-33442	-65940	-75496	-75496	-65940	-13326

Table 18: Aerodynamic loads for the different critical flight configurations at 15,000 ft.

7.2.2 Structural loads

The aerodynamic forces applied on the different parts of the aircraft are now known. The forces and moments induced by those forces in the structural parts have to be computed at points of interest in order to design the structure. Since the present stage is a preliminary design, the structural loading is evaluated at critical locations which are the fuselage section directly aft the wing for the rear fuselage structure and the wing root for the wing structure.
The forces and moments at those critical locations are put in equilibrium with:

- the self weights of the different components multiplied by the load factor,
- the aerodynamic forces computed in the previous section.

Fuselage section

Besides the aerodynamic forces computed at the previous step, additional loads are applied on the fuselage. Indeed, the self-weight of the fuselage and the V-tail as well as the weight of the engine, the rear fuel tank with its fuel and the electrical system must also be taken into account. Furthermore, the thrust developed by the engine will also influence the stress field. Considering all these parameters, the reaction forces and moments are as follows:

$$T_x = -T + \big(n.(W_{tail} + W_{fus} + W_{eng} + W_{elec} + W_{fuel}) - P\big).sin(\alpha), \tag{7.4}$$

$$T_y = -F_{fin}, \tag{7.5}$$

$$T_z = \big(n.(W_{tail} + W_{fus} + W_{eng} + W_{elec} + W_{fuel}) - P\big).cos(\alpha), \tag{7.6}$$

$$M_x = -M_{fus}, \tag{7.7}$$

$$M_y = n.cos(\alpha).(x_{tail}.W_{tail} + x_{fus}.W_{fus} + x_{eng}.W_{eng} + x_{elec}.W_{elec} + x_{fuel}.W_{fuel}) - P.x_{CP}.cos(\alpha), \tag{7.8}$$

$$M_z = -F_{fin}.x_{fin,CP}, \tag{7.9}$$

Note that the x-axis is chosen perpendicular to the considered section and passes through its centroïd, the y-axis is horizontal and the z-axis is perpendicular to both other axes and directed downward. The numerical results for the different critical flight conditions may be found in Tab. 19.

Case	A	C	D_1	D_2	E	F
T_x [lbf]	38795	16229	14626	8302	12287	14153
T_y [lbf]	10556	20811	23826	23826	20811	4205
T_z [lbf]	95311	103857	105669	22464	-23531	-21112
M_x [lbf.ft]	66883	131861	150967	150967	131861	26646
M_y [lbf.ft]	832952	928340	952290	302173	-160946	-130868
M_z [lbf.ft]	-141991	-279935	-320498	-320498	-279935	-56568

Table 19: Structural loads at the wing root for the different critical flight configurations.

One may conclude that the D_1 case is the most critical of all and therefore the subsequent analysis will be based on it.

Wing root

The self weight and the centre of gravity of the wing were evaluated from weight estimations conducted in section 5.7.

Then, the pressure distribution on the wing is modelled by applying the total lift, drag and moment generated by a halfspan wing at the aerodynamic center of the wing. Due to the fact that the lift distribution along the span is difficult to evaluate analytically, the span location of the aerodynamic centre was evaluated thanks the results obtained with Tranair.

Thus the structural loads at the wing root are calculated as followed:

$$T_x = \left(n.W_w - \frac{L}{2}\right) sin(\alpha + i_w) + \frac{D_w}{2} cos(\alpha + i_w), \tag{7.10}$$

$$T_z = \left(\frac{L}{2} - n.W_w\right) cos(\alpha + i_w) + \frac{D_w}{2} sin(\alpha + i_w), \tag{7.11}$$

$$M_x = -\left[\frac{L}{2} cos(\alpha + i_w) + \frac{D_w}{2} sin(\alpha + i_w)\right] y_{AC} + n.W_w.y_{CG}.cos(\alpha + i_w), \tag{7.12}$$

$$M_y = \frac{M_w}{2}, \tag{7.13}$$

$$M_z = \left[\frac{D_w}{2} cos(\alpha + i_w) - \frac{L}{2} sin(\alpha + i_w)\right] y_{AC} + n.W_w.y_{CG}.sin(\alpha + i_w). \tag{7.14}$$

Note that the same referential as the one presented for the fuselage section has been used here. The different numerical results are compiled in Tab. 20.

Case	A	C	D_1	D_2	E	F
T_x [lbf]	-26332	-1986	-18317	443	1023	-982
T_z [lbf]	78179	83239	83814	8908	-22958	-21759
M_x [lbf.ft]	-473553	-504305	-507862	-55500	138246	130825
M_y [lbf.ft]	-16723	-32970	-37748	-37748	-32970	-6663
M_z [lbf.ft]	-113191	10723	11464	4444	143	-9526

Table 20: Structural loads at the wing root for the different critical flight configurations.

7.3 Rear fuselage

The fuselage itself is composed of stringers and a skin. In addition, several frames are positioned in order to connect the stringers to the skin and thus to transmit the loads. Other less important components are also present but they will be neglected here in order to alleviate the complexity of the model.

7.3.1 Materials selection

All the geometrical parameters of the structural components of the fuselage highly depend on the materials used. The purpose of this section is thus to determine which material is the most suitable for the stringers, the skin and the frames of the fuselage. This selection will be performed with the software *CES EduPack* (Materials Selection software developed by Michael F. Ashby).

To begin with, the stringers' requirements are assessed. First, because one of the main goal in aeronautics is to minimise the overall mass of the structure, the density of the material must be limited. Moreover, a minimum yield strength, fatigue strength at 10^7 cycles and fracture toughness need to be fixed for obvious mechanical and safety reasons (300 [MPa], 200 [MPa] and 1 [MPa.m$^{0.5}$] respectively). Because of the engine proximity, the material should withstand high temperatures. Additionally, for safety reasons, the material should also be non-flammable or at least self-extinguishing. Finally, the fracture toughness must be optimised with respect to the Young's modulus and so should be done the yield strength with respect to the price per unit volume. After applying all these filters, it turned out that the *"Titanium, Ti-6Al-4V, aged"* suited the best the requirements. The stress associated to its elastic limit is then equal to 147,900 [psi].

Regarding the skin of the fuselage, similar filters have been applied. However, due to its contact with the outside, additional requirements have been set on the resistance against fresh and salted water. Eventually, the *"Titanium, alpha-beta alloy, Ti-6Al-2Sn-2Zr-2Mo, solution treated & aged"* whose yield strength is equal to 155,200 [psi] has been chosen here.
Finally, because the frames transmit relatively high loads, the *"Titanium, Ti-6Al-4V, aged"* has also been chosen as constitutive material for them.

7.3.2 Analytic study

First, an analytic preliminary study based on the loads obtained in Section 7.2.2 and on the materials chosen in Section 7.3.1 is performed in order to determine an approximation of the stress to which the section of interest is subjected. This first approximation will be used subsequently to verify finite element simulations of the structure.

In order to alleviate the complexity of this preliminary analysis, several assumptions have been set. Regarding the fuselage section, its shape has been assimilated to a perfectly circular section. Note that this simplification makes sense due to its likeness with the real section shape. Then, the stringers have been supposed to carry no shear stress while carrying the entire direct loading although a part of it is carried by the skin in reality. This last approximation makes sense due to its conservative aspect in the design of the stringers.

Stringers' section

To begin with, the direct stress induced by both moments M_z and M_y and by the engine thrust along the x-axis is considered. As mentioned previously, this stress is supposed to be only supported

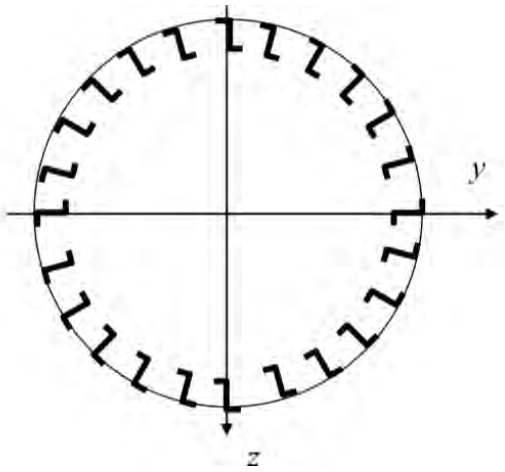

Figure 27: Scheme of the rear fuselage section of interest with an arbitrary number of stringers [12].

by the stringers and it will thus directly influence their section. Mathematically, if the reference frame is positoned at the the center of the circular simplified section as shown in Fig. 27, this direct stress can be expressed as:

$$\sigma_{xx}(y,z) = \frac{M_y}{I_{yy}}z - \frac{M_z}{I_{zz}}y - \frac{T_x}{Area}, \tag{7.15}$$

where $Area$ corresponds to the total area of the stringers, i.e. $Area = n_{st}B$ with B the area of a sole stringer (considered constant here) and where

$$I_{zz} = I_{yy} = \sum_{i=1}^{n_{st}} z_i^2 B = B\sum_{i=1}^{n_{st}} z_i^2, \tag{7.16}$$

with z_i the vertical location of the stringer i.

Therefore, a first guess on the stringers number needs to be done to be able to determine their section subsequently. From this guess and from Eq. 7.15, it is then possible to find the minimal required stringer section:

$$\sigma_{xx} = \frac{M_y}{B\sum_{i=1}^{n_{st}} z_i^2}z - \frac{M_z}{B\sum_{i=1}^{n_{st}} z_i^2}y + \frac{Thrust}{n_{st}B}, \tag{7.17}$$

$$B_{min} > \left(\frac{M_y}{\sum_{i=1}^{n_{st}} z_i^2}z - \frac{M_z}{\sum_{i=1}^{n_{st}} z_i^2}y + \frac{Thrust}{n_{st}}\right)\frac{1}{\sigma_{max}}, \tag{7.18}$$

where σ_{max} corresponds to the maximum stress allowed in each stringer. This value depends on the material the stringers are made of. Practically, it is equal to the theoretical 0.1 proof stress of the material divided by a safety factor equal to 1.5. As a first approximation, the maximum shear stress τ_{max} is simply equal to $0.6\sigma_{max}$. Note that this only holds for isotropic materials and it thus would be necessary to adapt these relations for composite materials.

Using $\sigma_{max} = \frac{147{,}900[\text{psi}]}{1.5}$, injecting this value in Eq. 7.18 and choosing a sufficient number of stringers to avoid any buckling of the skin (n_{st}=40 [-] here), one gets a minimal cross section B_{min}=0.174 [in^2].

Skin thickness

The skin thickness of the fuselage is now considered. It should be chosen such that the skin can resist the shear flow created by the torque M_x and the shear loads T_y and T_z that were computed earlier in Section 7.2. Therefore, the shear flow (set positive anti-clockwise) around the circular section has to be computed first. Because the number of stringers is relatively high, the shear stress between two successive stringers is considered as constant. In this case, each stringer is assimilated to a discontinuity. That way, the difference in shear flow on both side of a stringer due to the shear loads T_y and T_z becomes:

$$q^{i+1} - q^i = -\frac{T_z}{I_{yy}} B_i z_i - \frac{T_y}{I_{zz}} B_i y_i. \tag{7.19}$$

By applying this relation at each stringer all around the fuselage section, one gets a closed system of n_{st} equations and n_{st} unknowns.

Regarding the shear flow induced by the torque M_x, it is constant all around the section and it simply writes:

$$q_T = \frac{M_x}{2A}, \tag{7.20}$$

with A the fuselage cross section area.

By adding Eq. 7.19 and 7.20, one gets the total shear flow. The section undergoing the largest total shear flow q_{max} needs then to be determined. Indeed, the minimum thickness directly depends on the value of q_{max} as well as τ_{max}. The thickness t is then chosen such that:

$$\frac{q_{max}}{t} < \tau_{max} \quad \Longleftrightarrow \quad \frac{q_{max}}{\tau_{max}} < t. \tag{7.21}$$

Using τ_{max}=$0.6\frac{155{,}200[\text{psi}]}{1.5}$ and injecting it in Eq. 7.21, one gets as minimum skin thickness equal to 0.04 [in].

7.3.3 FEM study

In Fig. 28, the CAD as well as the finite element model of the rear fuselage obtained using the software *Siemens NX* are displayed.

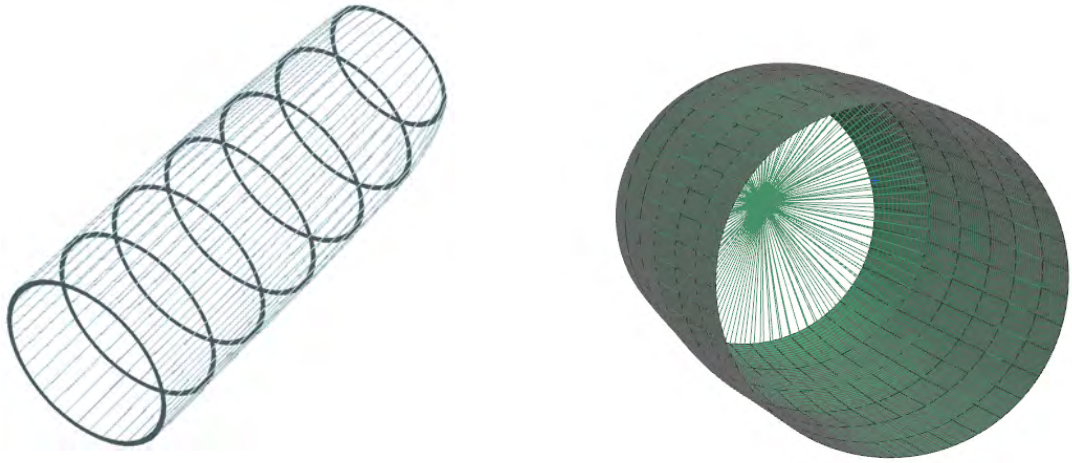

(a) CAD model of the rear fuselage.

(b) FE model of the rear fuselage.

Figure 28

The FEM internal structure of the fuselage part is shown in Fig 28b. Each longitudinal line corresponds to a stringer whilst each circle stands for a frame. Their respective section is chosen equal to 0.23 [in^2] and 0.85 [in^2] and the skin thickness is set to 0.06 [in] in order to keep a certain security margin with respect to the analytic results. In total, the rear fuselage is composed of 7 frames equally spaced from each other in order to keep its shape but also to fix the engine.
The green radii are assimilated to rigid links that connect a punctual mass related to the V-tail mass and located at the center of the fuselage. This point is also used as application point of the aerodynamic loads applied on the tail. Moreover, to account for the horizontal load applied on the tail, an additional torque is applied on the two last frames (where the tail is actually fixed). Note that because of the rigid links, the end segment of the fuselage is not able to deform. Therefore, it is not astonishing to observe a zero stress field in this portion of the structure, which is obviously not physic. However, because the prime interest of this simulation is the stress field at the left section of the fuselage, this approximation does not influence these results significantly.
Then, the mass of the engine, of the electrical system and of the full rear fuel tank is distributed on the corresponding frames. After that, the thrust developed by the engine is shared between all the frames. Eventually, a global acceleration corresponding to the 9 g is applied on the whole structure. As boundary condition, one chose to clamp the section of the fuselage near the wing.

Regarding the displacement, one gets a maximum deflection of almost 0.8 [in] at the free end of the fuselage, which is tolerable for a structure of this length (about 15[ft]). As expected, the fuselage deflection is a combination of a vertical motion with an horizontal component and with some twist.

These are mainly induced by the loading undergone by the V-tail.

Now, Von Mises stress field is considered. As it can be observed in Fig.29, the major stresses take place at the clamped end of the structure. Because of the mainly vertical deflection, the upper part of this section undergoes traction whilst the lower one carries compression. However, the maximum value of the Von Mises stress is about 34,800 [psi], which can be supported by the materials chosen in Section 7.3.1[2]. Note that one gets a substantial margin between these results and the ones obtained through the analytic study since the geometrical choices made in this simulation were rather conservative and also because the analytic study assumed that the sole stringers carried the direct stress whereas skin carries also a part of it.

Finally, note that the free end of the fuselage seems to carry no stress. As explained before, it is a consequence of the introduction of the rigid links shown in Fig.28b that keeps this section unstrained and thus stress free.

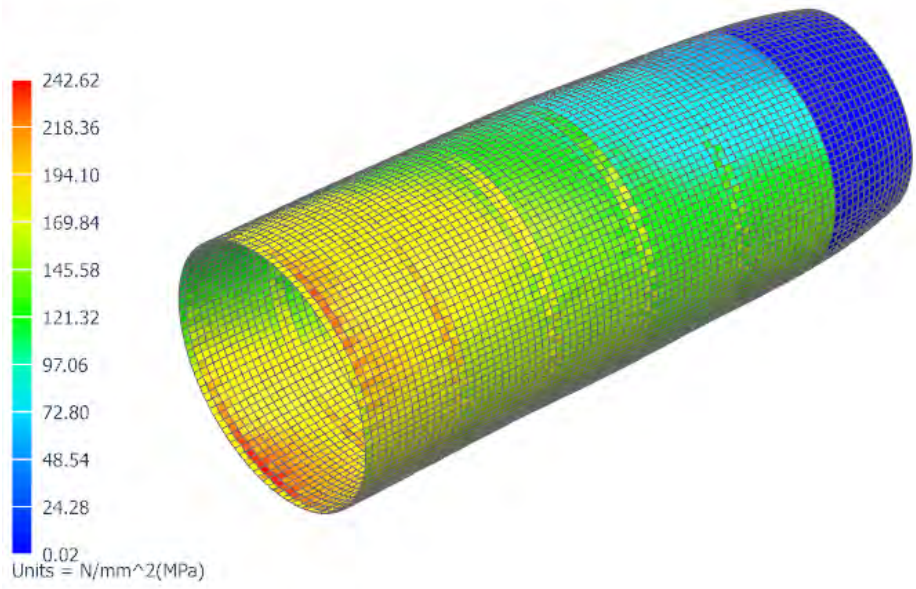

Figure 29: Von Mises stress field ([MPa].

7.4 Wing

As for the fuselage, the wing is composed of stringers and a skin. Additionally to those components, there are several spars which are beams in the spanwise direction of the wing and several ribs in the transverse direction. Moreover, there are also flanges between the spars and the skin in order to ensure the link between those two components. Once again, other components will be neglected to reduce

[2]The stress in the beams has also been checked and does not overpass the maximum allowed limit.

the complexity of the model.

7.4.1 Materials selection

As before, materials have to be assigned to the different structural parts of the wing in the purpose to design its structure. The different requirements which were mentioned for the materials selection of the fuselage structural parts are still valid except the fact that a high temperature resistivity is not needed anymore since the wing is not heated or very little.
The spars are withstanding more shear stresses than the skin panels. For that reason, a titanium alloy is used for the spars and an aluminium alloy for the skin. The titanium alloy that was retained is the *"Ti 6Al-4V"* which is a well-known material used in the aerospace industry with a better strength to density ratio than aluminium alloys and a good machinability and weldability. However, this material is much more expensive than aluminium alloys.
Then, the aluminium alloy that was chosen for the skin and the ribs at the same occasion is the *"Al-Li 2195"* which is used in the fuel and oxidizer tanks of SpaceX Launcher. This aluminium alloy provides a strong weight advantage while keeping good mechanical properties.
The stringers are also made of that aluminium alloy while the material assigned to the flanges is the titanium alloy *"Ti 6Al-4V"* in order to add flexural rigidity to the wing.

7.4.2 Analytic study

The first step of the preliminary design of the structure is to idealise the complex structure in order to perform an analytical study. This study allows to have a starting point before analysing the structure thanks to a finite element model by retrieving the section area of the stringers and the flanges and the thickness of the spars and the skin. Moreover, it helps the designer to choose a good configuration of the structure (i.e. number of stringers, number of spars,...). Ideally, the weight is optimised. After some tests, a configuration with 7 spars and 36 stringers has been chosen. This one is represented in Fig. 30. Note that this configuration is maybe not the optimised one. A deeper study should be performed. The front spar is set at 15% of the chord and the rear one at 75% because of the leading-edge and trailing-edge flaps.

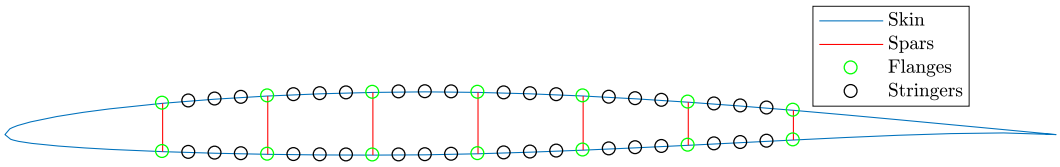

Figure 30: Model of the structural configuration of the wing at its root.

In our idealisation, the stringers and the flanges (booms) are assumed to carry all the direct stresses while the skin panels and the spars carry all the shear stresses. Then, the shear flow is considered constant between two booms as the distance between each of them is small. Through those assumptions the section area of the stringers should be over-evaluated. However, another severe assumption is set. It is the fact that the warping is allowed although the wing is clamped at its root. By doing that, the section area of the stringers and of the flanges are under-evaluated because the torsion of a beam which is clamped at one of its extremity induces direct stress in the longitudinal direction. Thus, a particular attention will be payed to this effect while performing the FEM analysis. Finally, the wing box (from front spar to rear spar) is assumed to carry all the loads because of the presence of the leading-edge and the trailing-edge flaps.

Bending

The biggest difficulty while performing an analytic study of the wing is that its section is not symmetric anymore. It implies that the expressions to evaluate the direct stresses in the booms have to be adapted. One has:

$$\sigma_{yy} = \frac{(I_{zz}M_x + I_{xz}M_z)z - (I_{xz}M_x + I_{xx}M_z)x}{I_{xx}I_{zz} - I_{xz}^2}. \tag{7.22}$$

The taper of each booms are then taken into account thanks to the following relation:

$$\sigma_{dir}^i = \sigma_{yy}^i \sqrt{1 + \left(\frac{\partial x}{\partial y}^i\right)^2 + \left(\frac{\partial z}{\partial y}^i\right)^2}. \tag{7.23}$$

This taper modifies the shear loads in the different panels which are adjacent to the booms. The corrected shear loads carried by the panels are then:

$$T_x^{pan} = T_x - \sum_i \sigma_{yy}^i A_i \frac{\partial x}{\partial y}^i, \tag{7.24}$$

$$T_z^{pan} = T_z - \sum_i \sigma_{yy}^i A_i \frac{\partial z}{\partial y}^i. \tag{7.25}$$

Shear flow

In order to evaluate the shear flow in the different panels, the shear flow is split into a shear flow induced by the torsion M_y and the shear flow induced by the shear loads T_x^{pan} and T_z^{pan}.
The shear flow induced by the torsion is constant in each cell and is computed thanks to the following equations:

$$M_y = \sum_i 2q^i A_h^i, \tag{7.26}$$

$$\frac{\partial \theta}{\partial x} = \frac{1}{2A_h^i \mu_{REF}} \big[-q^{i-1}\bar{l}_{i-1}^i + q^i \bar{l}^i - q^{i+1}\bar{l}_i^{i+1} \big], \tag{7.27}$$

with

- A_h^i the area of each cell,
- μ the shear modulus,
- $\bar{l}_{i-1}^i = \int_{(cell\ i \cap cell\ i-1)} \frac{ds}{t\frac{\mu}{\mu_{REF}}}$,
- $\bar{l}^i = \oint_{(cell\ i)} \frac{ds}{t\frac{\mu}{\mu_{REF}}}$.

The methodology to compute the shear flow induced by the shear loads is a bit longer. The first step is to make a cut in each cell and to compute the open flux of the whole beam section q_0 with the relation:

$$q_0^{i+1} - q_0^i = -\frac{I_{zz}T_z^{pan} - I_{xz}T_x^{pan}}{I_{xx}I_{zz} - I_{xz}^2} z_i A_i - \frac{I_{xx}T_x^{pan} - I_{xz}T_z^{pan}}{I_{xx}I_{zz} - I_{xz}^2} x_i A_i. \tag{7.28}$$

The next step is to compute the missing $q^i(0)$ at the cuts using compatibility of the twist rate. The equations are the following:

$$\frac{\partial \theta}{\partial x} = \frac{1}{2A_h^i \mu_{REF}} \big[-q^{i-1}(0)\bar{l}_{i-1}^i + q^i(0)\bar{l}^i - q^{i+1}(0)\bar{l}_i^{i+1} + \oint_{(cell\ i)} \frac{q_0}{t\frac{\mu}{\mu_{REF}}} ds \big], \tag{7.29}$$

$$x_T T_z - z_T T_x = \sum_i \int_{wall\ i} q_0 p ds + \sum_{cell\ i} 2A_h^i q^i(0) + \sum_{boom\ j} x^j \sigma_{yy}^j \frac{\partial z}{\partial x}^j A_j - \sum_{boom\ j} z^j \sigma_{yy}^j \frac{\partial y}{\partial x}^j A_j \tag{7.30}$$

Final results

The sizing of the structural elements is based on the elastic design approach. The different materials should deform in the elastic region and therefore the stresses must be lower than the elastic limit. Furthermore, a safety factor s equal to 1.5 is applied on those elastic limits. Thus, for each material, the maximum tensile and shear stresses are

$$\sigma_{max} = \frac{\sigma_{yield}}{s}, \tag{7.31}$$

$$\tau_{max} = \frac{\tau_{max}}{s}. \tag{7.32}$$

After the analytic study, the values in Tab. 21 for the different variables of the structure of the wing were obtained.

A_{str} [in^2]	0.85
A_{fl} [in^2]	0.93
t_{spars} [in]	0.0591
t_{skin} [in]	0.0787

Table 21: Values of the different variables of the structural parts of the wing obtained with the analytic study.

7.4.3 FEM Analysis

Once the analytic study is completed, a finite element verification has to be performed in order to ensure the structure integrity. Based on the CAD model which presented in Fig. 31, a finite element model is built using shell elements for the different panels and 1D beam elements for the stringers and flanges. This FE model is shown in Fig. 32. A particular attention had to be paid to ensure the links between the different parts of the structure.

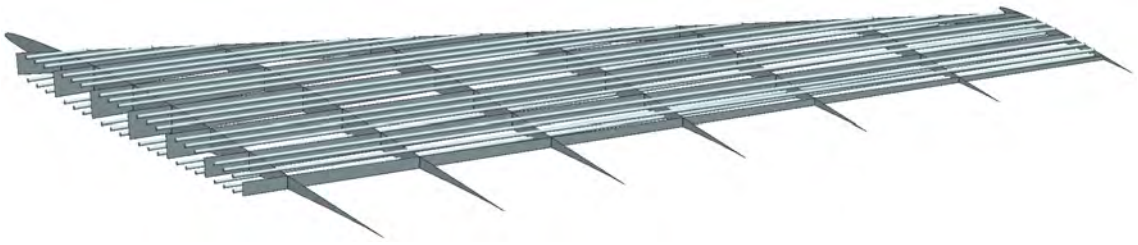

Figure 31: CAD model of the wing internal structure.

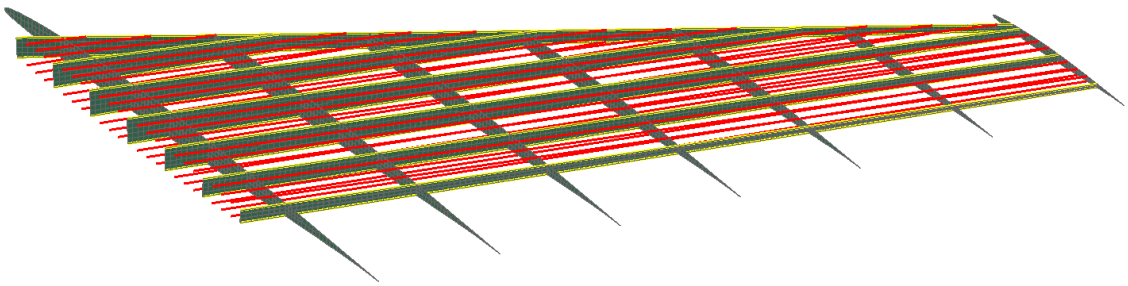

Figure 32: Finite element model of the wing internal structure.

Boundary conditions When the mesh collectors are realised, FEA parameters must be imposed on the structure. The first thing to impose is the clamping of the wing at its root.

Applied loads Then, the different loads have to be applied to the structure.
The first load is the gravity multiplied by the load factor. This was applied on the whole structure thanks to an acceleration by taking into account the angle of attack of the wing.
The other applied loads are the aerodynamic loads. In a first simulation, a uniform pressure distribution was applied on the intrados of the wing in order to verify if the finite element model was well defined. Once it was ensured, the actual pressure distribution computed with Tranair has been applied to the model. Note that only a little more than 6 g maneuvres could be simulated with Tranair at 1.3 M. The resulting pressure distribution has the been multiplied with the appropriate factor such that the resulting lift force is indeed $9W$. The effect of larger A.o.A. is thus here partially neglected. This apprixmation seems however staisfactory for a preliminary study.

Results When the simulation was realised with the parameters obtained with the analytic study, it came out huge shear stresses at the rear spar. This can be explained by the fact that this spar has to withstand a major part of the aerodynamic loads generated by the trailing-edge flap. A solution for that issue is to thicken the rear spar. Another issue was an exceed for the direct stresses at the rear booms. As mentioned during the analytic study, the assumption about allowing the warping due to torsion was a severe restriction for a wing. The direct stresses in the rear booms was actually under-estimated. Therefore, an additional area for the stringers and the flanges was added. We finally have a deflection at the wing tip around 17.5 [in]. The final values are set up in Tab. 22. Fig. 33 shows the distribution of stresses in the wing structural parts.

A_{str} [in^2]	1.01
A_{fl} [in^2]	1.31
t_{spars} [in]	0.0591
$t_{rear\ spars}$ [in]	0.236
t_{skin} [in]	0.0787

Table 22: Values of the different variables of the structural parts of the wing corrected by the FEA.

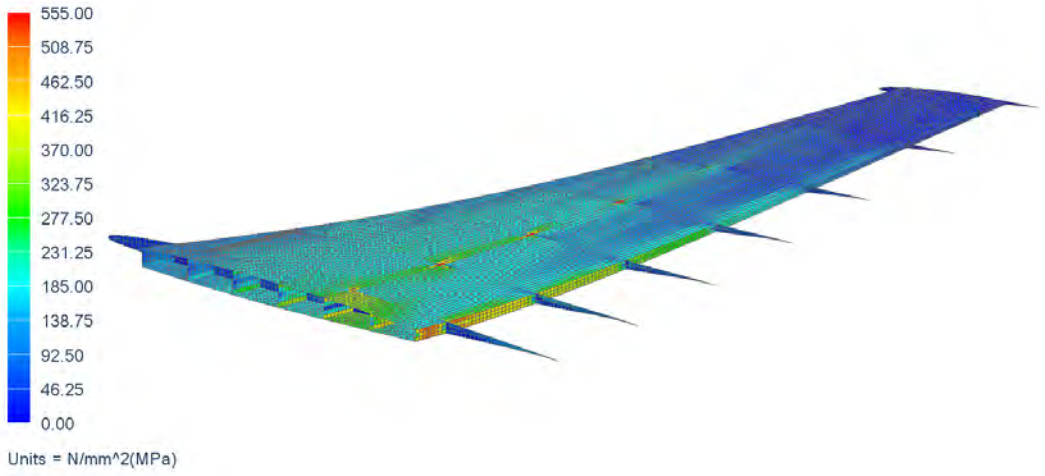

Figure 33: Von Mises stress distribution in the wing structural parts for the most critical flight configuration [MPa].

7.5 Further improvements

During this preliminary design of the structure, strong assumptions were made in order to alleviate the complexity of the reality. In more advanced design, the structure design should be made by performing a modal analysis, a buckling analysis and eventually a fatigue and crack propagation analysis.

In addition, it was assumed, for example, that the wing is made in one piece, disregarding the flaps, slats and ailerons which should also be designed and assembled to the wing box through mechanisms. Finally, the structure of the rest of the aircraft should also be considered. This last one is represented in Fig. 34.

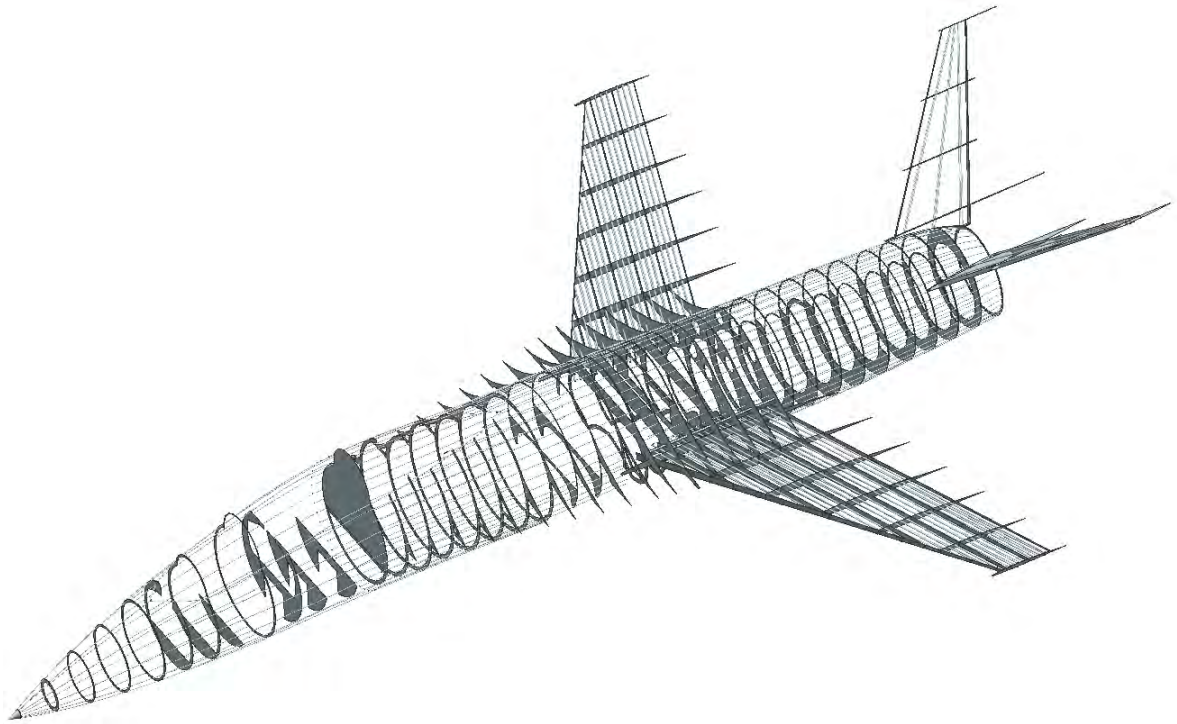

Figure 34: CAD model of the aircraft structure.

8 Static stability margins

The purpose of a static stability analysis is to assess the behaviour of the aircraft in response to a perturbation in the flight attitude (due to a gust for example). The stability margins are assessed by computing the derivative of the rotational moment with respect to the associated A.o.A. (or the associated lift force if one wishes to take compressibility effects into account). The sign of this derivative determines whether the current configuration is stable, unstable or neutrally stable. Note that only the controls fixed stability is investigated here, since most aircraft are more stable controls free than controls fixed.

8.1 Margins estimates

As mentioned previously, the stability is assessed by computing the derivative of the moment around the pitch axis with respect to the lift produced by the aircraft. In practice, it will be approximated by taking the derivative with respect to the lift produced by the wings only. It is common to specify the stability characteristics by computing the position of the neutral point h_n. It corresponds to the virtual position that the C.o.G. should have if the aircraft was to be neutrally stable. In other words, it denotes the position of the centre of gravity such that:

$$\frac{\partial C_m}{\partial C_{Lw}} = 0. \tag{8.1}$$

The difference between the position of the neutral point h_n and that of the actual C.o.G. h (both expressed as a fraction of the M.A.C.) then gives the stability margin. Taking the derivative of Eq. 5.26 with respect to the wing lift coefficient and equating it to zero allows to rearrange the terms as follows:

$$h_n = h_0 + \frac{dC_{LT}}{dC_{Lw}} \frac{l_T S_T}{\bar{\bar{c}} S} - \frac{dC_{m\text{fus}}}{dC_{Lw}}, \tag{8.2}$$

where h_0 denotes the position of the a.c., and is approximated by the quarter chord at subsonic speeds ($h_0 \approx 0.25$ since it is expressed as a fraction of $\bar{\bar{c}}$). Notice that the derivative of the wing moment coefficient C_{m0} is equal to zero since it is a constant. Also note that the effect of the fuselage must be accounted for, since it has a small moment but a high derivative. It was estimated using empirical formulas.

The computation of the derivative of the tail lift coefficient with respect to the the wing lift coefficient involves the known lift curve slopes of the wing and the tail. As the flow seen by the tail is perturbed by the wings, the effect of the downwash velocity must be estimated as well. In the early stages of the design, this effect, as well as the one coming from the fuselage, may be approximated by using empirical formulae ([17], appendix E). In addition, only cruise conditions (0.8 M) are investigated.

In later stages, Eq. 8.2 is estimated by modelling both the wing and the tail in Tranair (allowing to account for the downwash) for the three flow conditions studied in section 6. The derivatives intervening in this expression may be approximated by finite difference between two cases with a slightly different A.o.A. In addition, the derivative of the pitching moment of the fuselage must be included as well, using the same empirical formula than during the early estimates.

In subsonic conditions, the V-tail is locked and only the rudder is deflected. Before carrying out any stability estimations, its angle of incidence must thus be determined. The latter is selected such that equilibrium is ensured by the angle of incidence of the tail alone during cruise at 50 % fuel weight (no deflection of the rudder is required). Proceeding by trial and error with Tranair shows that an angle of incidence $i_T = -1.3$ [°] fulfils this objective. Note that the deflection of the rudder is not modelled in Tranair. In addition, although the V-tail is switched to all movable in supersonic conditions, $i_T = -1.3$ [°] is used to compute the stability margins for the dash segment.

Stability characteristics are then expressed in terms of stability margin:

$$K_n = h_n - h, \tag{8.3}$$

where h denotes the actual position of the C.o.G. It is specified in the request for proposal that this stability margin must remain within the interval $[-5; 15]$ % at every moment in flight.

Eq. 5.26 shows that there are two degrees of freedom one can manipulate to find a suitable configu-

ration: the respective surfaces of the wings and of the tail and the moment arm of the tail. Since the surface of the tail is estimated by a scaling of the surface of the wings here, there in fact only remains as degrees of freedom:

- the position of the wing
- the position of the tail (through the length of the fuselage).

These two positions must thus be selected so that the stability margins are within the admissible interval.

The single engine configuration chosen here for the fighter implies that C.o.G. of the empty aircraft is located far aft. As a consequence, the wings must be positioned far aft as well to avoid excessive instability. A wing positioned too far aft would induce a low tail volume ratio V_T (or c_{HT}), as it is proportional to the moment arm of the tail (C.o.G. would be shifted even further aft). In order to maintain a good manoeuvrability, the wing is thus positioned as close to the nose as possible, under the constrain that the stability margin remains within the admissible interval.
Notice that with a short fuselage (about 35 [ft]), it is impossible to find an admissible configuration in terms of stability margin while maintaining a decent tail volume ratio ($V_T \in [0.4, 0.7]$, cf. section 5.8). Only longer fuselages meet these two constraints. It should also be noted that the moment arm of the tail varies as fuel is burned since the C.o.G. of the aircraft translates. Consequently, the tail volume ratio varies as well. This variation is however negligible if the fuel tanks layout selection is such that the C.o.G. excursion is small.

8.2 Computation points

Note that the stability margin will vary throughout the mission: the neutral point depends on the free stream Mach number through the wing and tail lift curve slopes. Additionaly, the C.o.G. moves as fuel is consumed. Consequently, the stability margin must be estimated for several configurations (in terms of fuel weight), encompassing every configuration encountered during the mission. It was chosen here to compute the stability margin for the following cases:

- full fuel tanks,
- 50 % fuel weight,
- empty fuel tanks,
- farthest aft centre of gravity.

Note that the full fuel and the farthest aft configurations encompass all others. The two intermediate ones are estimated for information only. Notice that the margin would also change when payload is released, but the 1000 [lbs] of payload are assumed here to be retained throughout the flight.

Since the C.o.G. of the trainer may be estimated at any moment in flight, the stability margins of the current design may be assessed using Eq. 8.2 and 8.3. Note that these margins are computed with the assumption that the respective C.o.G. of the fuel tanks does not change as fuel is consumed. This assumption is only valid if some form of vertical partitioning is implemented inside the fuel tanks, which may further reduce the tanks capacities.

The stability margins are compiled in Tab. 23. Two sets of values are here compared. On the left are compiled the values obtained with the empirical relations for the downwash effect, the first rough C.o.G. estimates presented in Tab. 7 and the assumption that the a.c. of the wing is at the quarter chord of the M.A.C. for the only one flight condition: cruise. Since high manoeuvrability is desirable, a slightly unstable configuration was selected. On the right are listed the margins calculated with Tranair numerical results accounting for the downwash effect and the actual a.c. position together with the more accurate C.o.G. estimates performed on the CAD model for three flow conditions: take-off and landing (0.3 M - 1000 [ft]), cruise (0.8 M - 35,000 [ft]) and dash (1.2 M - 35,000 [ft]). Although the subsonic margins obtained here are well inside the admissible interval $[-5, 15]$, notice that they are larger than the slightly unstable configuration targeted in the pre-design (cf. first column of Tab. 23). It is resulting from the overestimation of the downwash effect with the empirical relation ([17], appendix E) during the pre-design together with the a.c. of the wing being aft of the quarter chord. If higher manoeuvrability is desired for the Coyote, the wing should be slightly translated forward, yielding an overall reduction of the margins.

Although no interval is provided for the supersonic margin, those obtained here are more than likely too large for the aircraft to operate in dash condition. This is a result of the shift of the a.c. of the wing to about the half chord in supersonic and of a significant reduction of the downwash effect compared to subsonic. The margin is however reduced to about 20 % if the remaining fuel at 35 % fuel weight is pumped into the rear fuel tank.

	Empirical	CAD + Tranair		
	Cruise	T-O & Landing	Cruise	Dash
Full fuel	-1.3	3.0	4.6	41.7
50 % fuel	-2.0	0.9	2.8	39.7
Farthest aft	-4.0	-1.3	1.3	37.7
Empty	-3.6	0.3	2.6	40.1
C.o.G. excursion (in % of the M.A.C.)	2.6	4.3		

Table 23: Stability margins estimates with empirical relations for cruise conditions and with Tranair simulations and CAD model C.o.G. for three flow conditions (expressed in %).

9 Dynamic stability and handling qualities

This section discusses the dynamic stability of the Coyote. In order to assess how manoeuvrable an aircraft is, one needs to find a mean to evaluate the aerodynamic stability derivatives and control derivatives of the said aircraft. The best way would be, of course, to measure those stability derivatives directly on the in-flight aircraft. For the preliminary design of the jet trainer, simplified methods stemming from the USAF DATCOM document will be used to estimate their values. Afterwards, the dynamic stability and flying qualities of the aircraft are to be evaluated against the Mil-F-8785c requirements in order to make sure the Coyote can be used by the U. S. Military.

The equations which describe the motion of a flight vehicle are nonlinear and thus difficult to solve. They will first be linearised. Then, in this case, the solutions to the linearised equations are approximated around small perturbations to an equilibrium flight condition, which would be the cruise flight condition (0.8 M, 35,000 [ft] and 50 % fuel) for starters. As for the static case, pitch stability usually is decoupled from yaw and roll stability which allows the study of two independent sets of equations of motion. In other words, perturbations in the longitudinal forces and moments do not depend on lateral perturbations and *vice versa*.

Once computed, the stability derivatives are injected into the linearised equations of motion in order to solve the system. The equations of motion can be rewritten in a standard compact state space form, which gives

$$\dot{\mathbf{x}} = \mathbf{A}\mathbf{x} + \mathbf{B}\mathbf{u}. \tag{9.1}$$

The space state form is convenient because it allows to represent the physical system as a set of inputs, outputs and state variables. Also, the dynamic stability depends on the complex eigenvalues of the matrix $\mathbf{A}$. In this case, $\mathbf{x} = \begin{bmatrix} u & v & w & p & q & r & \phi & \theta & \psi \end{bmatrix}^{\mathrm{T}}$ would be the system states regarding the

velocities and angular velocities relative to the aircraft's center of gravity and the aircraft geometrical axes. While $\mathbf{u} = \begin{bmatrix} \xi & \eta & \zeta & \tau \end{bmatrix}^{\mathrm{T}}$ are the system inputs where ξ, η, ζ are the deflection with respect to the trim position of the primary control surfaces, respectively the ailerons, the elevator and the rudder. For the Coyote, the computed eigenvalues all have a negative real parts, shows that the whole system is stable (i.e. perturbations are damped out over time). They are listed the Table 24 below for the longitudinal and lateral cases.

	Longitudinal	Lateral
Eigenvalues	$-0.4934 + 0.1244i$	$-0.0476 + 3.0129i$
	$-0.4934 - 0.1244i$	$-0.0476 - 3.0129i$
	$-0.003 + 0.0147i$	$-0.8183 + 0.0000i$
	$-0.003 + 0.0147i$	$-0.0746 + 0.0000i$
		$0.0000 + 0.0000i$

Table 24: Roots of the longitudinal and lateral characteristic polynomials.

9.1 Handling characteristics

The Coyote qualifies as a trainer for Class IV: high-manoeuvrability airplane, specifically a fighter. The missions the aircraft is expected to be able to handle are split into different categories (A, B and C) which comprise different flight phases. Likewise, range of values for the stability or control parameters are required to be met for the designed aircraft, according to Levels (1, 2 and 3) that relate to the ability to complete the mission.

When solving the equations of motion in the state space form, the system inputs are represented as elementary inputs functions : step, ramp and impulse. Put together, they put on the perturbations that can happen to the aircraft. Then, the full response of the aircraft can be studied. By doing so, the longitudinal and lateral results demonstrate several modes of vibration. Respectively, short-period oscillation and phugoïd in longitudinal and spiral mode, roll subsidence and dutch roll in lateral. The different modes can be found by inspection of the roots of the characteristic polynomials.

Phugoïd oscillations are the results of an elevator deflection around a trimmed position. This causes the aircraft to either nose up or nose down. The aircraft remaining tangent to the flight path, the angle of attack doesn't change during phugoïds. This type of oscillations have very low damping and a large period therefore can last for a very long time. By contrast, short-period oscillations are driven by the angle of attack and usually take place after steep input changes. The period usually decreases

with airspeed but the damping can either decrease or increase.

Spiral mode has very low damping and thus a high large time constant τ_{RS}. It is a non-oscillatory mode as the eigenvalue associated to be spiral mode has no imaginary part. Since this mode has a large time constant, this mode being either stable or unstable is not much of a concern. The roll mode is not a oscillatory one either, meaning that the aircraft will stop rolling after sufficient time. The last lateral mode is the Dutch Roll. It is displayed by having the centre of gravity remaining on the same flight path while the roll and yaw angles oscillate. It should be noted that the Dutch Roll damping increases with airspeed while its period first increase then decrease with respect to airspeed.

9.1.1 Longitudinal flying qualities

Using the values of the eigenvalues of the previously introduced matrices **A**, the frequency and the damping of both the short-period oscillation and phugoïd can be determined. Naturally, no damping would make the oscillations go on endlessly and too much damping would make the pilot feel all the bumps. With that in mind, from the longitudinal characteristic polynomial, the Coyote manifests:

	Short-period oscillations	Phugoid
Frequency [rad/s]	$\omega_s = 0.5088$	$\omega_p = 0.0147$
Damping ratio [-]	$\zeta_s = 0.9696$	$\zeta_p = 0.0189$

Table 25: Frequency and damping ratios for the short-period oscillation and phugoid modes

ζ_s	Category A and C		Category B	
Level	Minimum	Maximum	Minimum	Maximum
1	0.35	1.30	0.30	2.00
2	0.25	2.00	0.20	2.00
3	0.15	-	0.15	-

Table 26: Mil-F-8785c values for short-period damping ratio limits.

On the one hand, according to the computed value of ζ_s, the Coyote is within the required ranges of damping ratios, for all the levels and categories of flight phases. On the other hand, for the phugoïd stability, ζ_p is required to be greater than 0.04 for Level 1 qualification, and ζ_p at least of 0 for Level 2 qualification. That is, since the oscillation period can last for a long time and has a very low damping ratio. In this case, the value of ζ_p is smaller than the requirements to be Level-1 certified. This means

this mode needs special care in order to meet the desired airworthiness regulations. In that regard, an augmented stability system will be discussed in the next section. Finally, one can notice that phugoïd and short-period oscillation modes are well separated in frequency, such that $\frac{\omega_p}{\omega_s} << 0.1$.

9.1.2 Lateral flying qualities

Information about the stability of the system can be extracted by analysing the eigenvalues of the matrix **A** again. The null eigenvalue means that the aircraft has little to no restoring force in the roll direction.

For the lateral case, different modes are to be appraised. The values of the roots of the lateral characteristic polynomial tell that the small value is a low damping mode, associated to the spiral mode, the higher value of another root is a high damping mode, associated in this case to the roll subsidence. The last one, a complex root, involves the dutch roll mode. These three modes will be also assessed against the Mil-F-8785c requirements.

From the computations, one gets for the dutch roll:

$$\omega_{\text{nd}} = 3.0133 \text{ [rad/s]},$$

$$\zeta_d = 0.0158 \text{ [-]},$$

$$\zeta_d \omega_{\text{nd}} = 0.0476 \text{ [rad/s]}.$$

Comparing the values to the Mil requirements (see Tab. 27 below), it is clear that the damping ratio for this mode is inappropriate. This needs to be corrected through the stability augmentation in order to meet the requirements.

Level	Category	Class	Min ζ_d [-]	Min $\zeta_d\omega_{\text{nd}}$ [rad/s]	Min ω_{nd} [rad/s]
1	Air combat	IV	0.4	-	1.0
	A	I, IV	0.19	0.35	1.0
	B	All	0.08	0.15	0.4
	C	IV	0.08	0.15	1.0
2	All	All	0.02	0.05	0.4
3	All	All	0	0	0.4

Table 27: Mil-F-8786c values for minimum Dutch roll frequency and damping.

Concerning the roll-subsidence mode, the time constant τ_{R} is measured from the response to a step input. Actually, it is the time required to achieve 63% of the final roll rate. In other words, one gets:

$$\tau_{\mathrm{R}} = \frac{\ln 2}{-\zeta_R},$$
$$= 0.847 \text{ [s]}.$$

When compared to the Mil requirements (see Fig. 28), it is clear that the Coyote qualifies for all the categories and levels of flight.

Category	Class	Level		
		1	2	3
A	I, IV	1.0	1.4	-
B	All	1.4	3.0	10
C	I, II, IV	1.0	1.4	-

Table 28: Mil-F-8785c values for maximum roll-mode time constant in seconds.

Finally, the designed aircraft must be assessed in terms of spiral stability. The minimum time needed to double the amplitude is given by:

$$\tau_{\mathrm{RS}} = \frac{\ln 2}{-\zeta_{\mathrm{RS}}},$$
$$= 9.292 \text{ [s]}.$$

The value of τ_{RS} is too low to qualify the aircraft for a flight phase category A and C related to an ability to complete the mission of Level 1. This must be addressed in the augmented stability design.

Category	Level 1	Level 2	Level 3
A and C	12	8	4
B	20	8	4

Table 29: Mil-F-8785c values for spiral stability, in seconds

9.2 Stability Augmentation

The stability of a aircraft can be improved thanks to flight control systems. So as to meet the Mil-F-8785c requirements regarding the dynamic stability, the modification of some dynamic modes will be done by using the full state feedback. Just as a reminder, the damping of the phugoïd oscillations was not high enough for a Level 1 certification, as well as the damping of Dutch Roll oscillations. If

the damping is too low, it makes the oscillations go on for too long. Finally, the minimum time to double the amplitude for the spiral stability is also too low.

A flight control system can be seen as a closed loop where the pilot interacts with the controls to manoeuvre the aircraft and the aircraft responses are the outputs while the motions cues are the direct feedback to the pilot. Modern aircraft include many other instruments that are described in the request for proposal (see Attachment 3 and Attachment 5). An example of such a looped feedback system can be seen in Fig. 35 below.

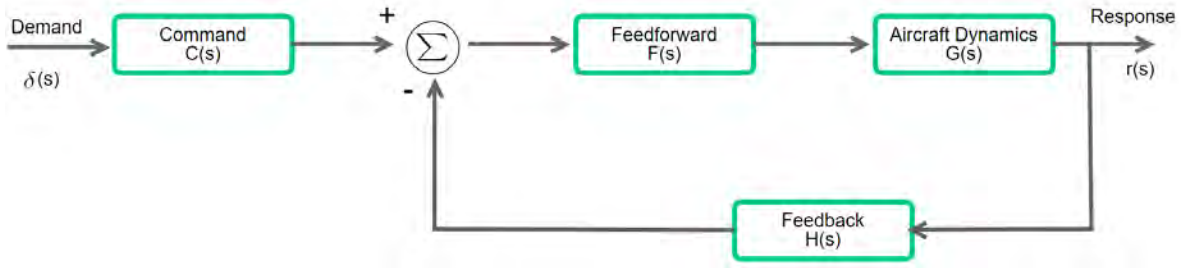

Figure 35: Inner loop diagram for the augmented stability shown in terms of transfer functions.

In this case, stability augmentation is going to be used in order to improve the flying qualities of the aircraft beyond what was possible during the aircraft design. The stability augmentation usually takes place in the inner loop of the state feedback.

Following the complete transfer function, one can obtain

$$\text{The output } r(s) = F(s)G(s)\varepsilon(s)$$

$$\text{The error signal } \varepsilon(s) = C(s)\delta(s) - H(s)r(s)$$

$$\text{The augmented transfer function } \frac{r(s)}{\delta(s)} = C(s)\left(\frac{F(s)G(s)}{1 + F(s)G(s)H(s)}\right)$$

$$\text{The new characteristic polynomial } \Delta_{\text{aug}} = 1 + F(s)G(s)H(s)$$

By choosing wisely the different transfer functions $C(s)$, $F(s)$ and $H(s)$, the eigenvalues of the matrices $\mathbf{A}$ can greatly change and thus enhance the stability of the aircraft. Moreover, it can be shown that the flight control system dynamics can become almost independent of the aircraft dynamics. If the product of the controls functions are much greater than one, it can be indeed approximated that:

$$\frac{r(s)}{\delta(s)} \approx \frac{C(s)}{H(s)}.$$

To simplify the feedback system, the FCS system will be assumed with a constant values of $C(s) = 1$, $F(s) = 1$ and $H(s) = K$.

In order to increase the damping ratio of the phugoïd mode, one has:

$$\begin{aligned}\Delta_{\text{aug}}(s) &= \Delta(s) + K_q N_\eta^q(s) \\ &= (21334258621.9s^4 + 21064285881.4s^3 + 5540129217.6s^2 + 7597805.4s + 1189883.6) \\ &- K_q\left(-s\left(72437507729.7s^2 + 37945805574.6s + 44094835.9\right)\right).\end{aligned}$$

It appears that a negative value for K_q is desirable in the case of phugoïd if the goal is to make the damping larger. If K_q is chosen at -0.2, it results that the augmented damping ratio is now $\zeta_{p,\text{aug}} = 0.0528$, which allows the aircraft to be qualified for any missions at Level 1 (see Table 26).

9.3 Future Work

For the purpose of meeting all the requirements of the Mil-F-8785c for all the different categories at Level 1, stability augmentation must be considered in the lateral case as well. As a matter of fact, the current design of the Coyote has a damping ratio below the specified value for the Dutch Roll mode. Finally, the augmented stability must increase the time constant of the spiral mode. This is done by another feedback loop that would lower the value of the spiral damping ratio.

10 Performance

Assessing some of the main performance characteristics of the current design is necessary to judge the compliance of the trainer with the objectives.

10.1 Level turn

A major measure of merit for fighter aircraft is their ability to perform short turning manoeuvres. It is possible to study the turning performance for a turn in the horizontal plane by writing the force equilibrium between the lift, the weight and the centrifugal force. In particular, it is possible to write the turn rate $\dot{\psi}$ as a function of the airspeed V and the turning radius R or the load factor $n = \frac{L}{W}$ as:

$$\begin{aligned}\dot{\psi} &= \frac{V}{R}, \\ \dot{\psi} &= \frac{g\sqrt{n^2-1}}{V}.\end{aligned} \tag{10.1}$$

Determining then whether the aircraft is able to sustain this turn rate is indicated by the specific excess power:

$$P_s = V\frac{(T-D)}{W}. \tag{10.2}$$

If P_s is equal to zero, the turn is operated at constant speed. If it is negative, the aircraft decelerates during the manoeuvre and *vice versa* if it is positive. The total drag force D may be estimated with the drag polar of the aircraft determined in section 6.
Turning performance may be summarised by the energy manoeuvrability diagram. It is displayed in Fig. 36 at $15,000$ [ft], 50 % fuel weight and maximum afterburner thrust. It plots contours of constant P_s on a map of the turn rate and the Mach number. Eq. 10.1 allows to draw curves of constant load factor or turn radius. The aerodynamic limit is drawn in red and corresponds to the curve to the left of which the aircraft would stall. A maximum lift coefficient of 1.2 is used here and the corresponding limit is approximate since the effect of the LEX has not been investigated. The diagram is also bounded by the maximum design load factor $n = 9$ and the maximum Mach number $M = 1.2$. Note that is has been shown in section 6 that the Coyote could potentially reach 1.5 M. Designing the structure of the aircraft for such a high Mach number would however be a costly over-design with regard to the dash speed objective of 1.2 M.

It should be mentioned that the P_s contours have been evaluated with the drag polar at $35,000$ [ft] and 0.8 M for all subsonic Mach numbers and at 1.2 M for the supersonic region, resulting in the strong discontinuity of the contours visible in the diagram. In the transonic region ranging from 0.9 M to 1.1 M approximately, only the general trend of the contours may be trusted. In addition, the Reynolds number is about two times larger at 15,000 [ft] than at 35,000 [ft]. Viscous effect have thus likely been over-estimated for airspeeds between 0.4 M and 1.2 M, but under-estimated below 0.4 M (region of lesser interest).

These turn performance estimates show that the Coyote is able to sustain 8 g turns without decelerating at about 0.8 M. As mentioned earlier, the performance objectives are unclear when specifying that the trainer should sustain 9 g manoeuvres. It is interpreted here as a requirement for instantaneous turn, i.e. with a deceleration. The diagram shows that the Coyote can perform 9 g turns with a moderately negative P_s of -200 [ft/s] at 0.8 M. The 20-minute long manoeuvre segment cannot however be performed with the afterburner. If the maximum military thrust is considered, the Coyote may only sustain 6 g at 0.85 M with a constant speed and 7 g 0.8 M and a P_s of -200 [ft/s]. This is about the limit that human body can sustain with a g-suit (especially during 20 minutes!) and the objective is considered achieved.
The corner speed (top corner of the envelope) is here equal to 400 [KCAS] which is rather large compared to most fighters (it results from the low maximum lift coefficient considered here). A minimum turning radius of about 2300 [ft] is achieved at this point (corner speed and 9 g).

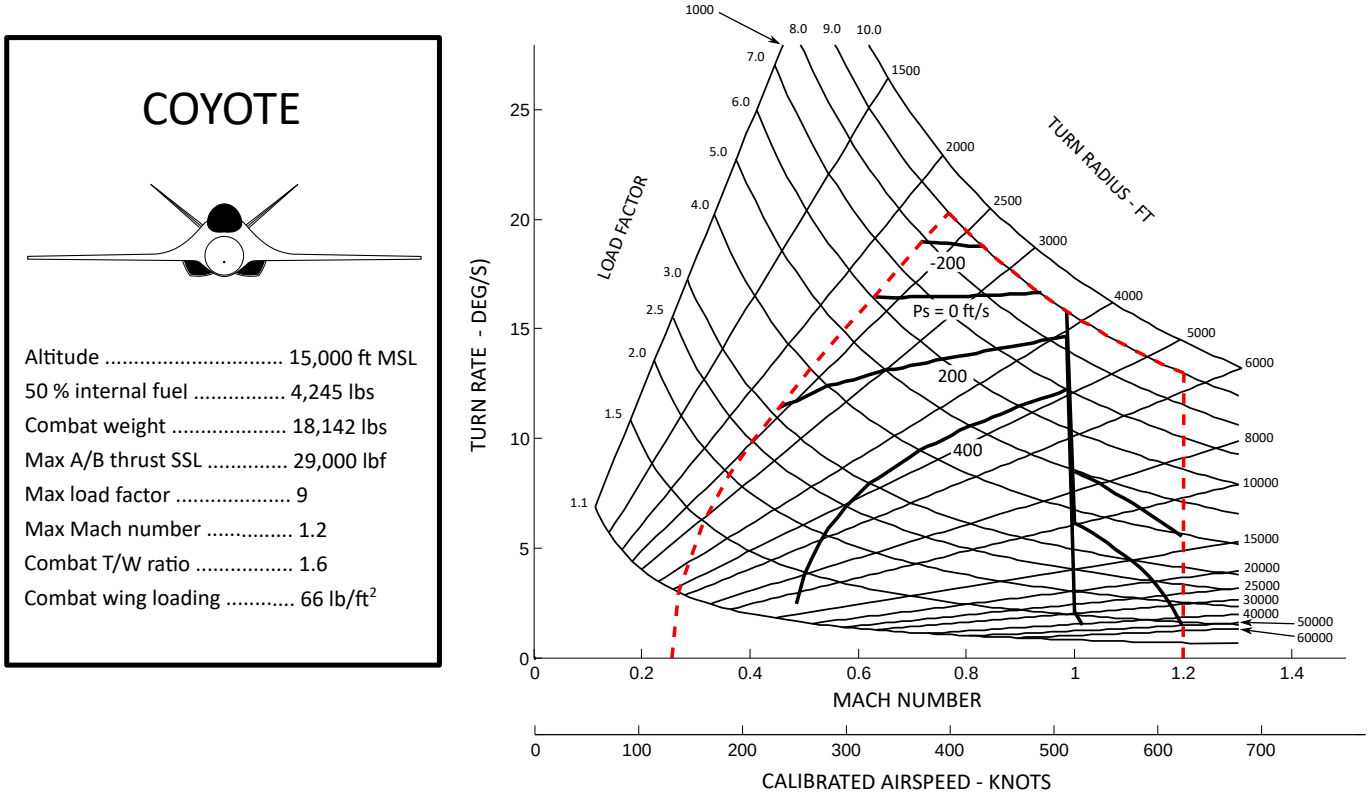

Figure 36: Energy manoeuvrability diagram of the Coyote at 15,000 [ft] MSL, 50 % fuel weight and maximum afterburner thrust.

An additional envelope may bring insight about the evolution of the performance of the Coyote with respect to the altitude. Fig. 37 displays constant P_s contours on a map of the altitude and Mach number for 1 and 5-g, 50 % fuel weight and maximum afterburner thrust. Envelope (a) shows that the Coyote is able to cover altitudes from see level to more that 60,000 [ft] for subsonic level flight (1 g) with a positive P_s (power in excess). As it is the case for the energy manoeuvrability diagram, P_s contours drop abruptly when traversing the transonic region. Once again, the drag polars at 35,000 [ft] 0.8 M and 1.2 M have been used to characterise the entire flight envelope (subsonic and supersonic contours have here been connected artificially for aesthetic purposes). Viscous effects have thus been over- or under-estimated away from these Mach numbers and this altitude. A descent altitude of 50,000 [ft] is however still reached in transonic.

Envelope (b) shows that the contours shrink significantly when the aircraft must sustain 5-g manoeuvres. The subsonic operational flight envelope is also reduced by the aerodynamic limit and the Coyote may cover the entirety of if with a P_s of at least -100 [ft/s]. The supersonic region however is barely accessible, and at the cost of a negative P_s.

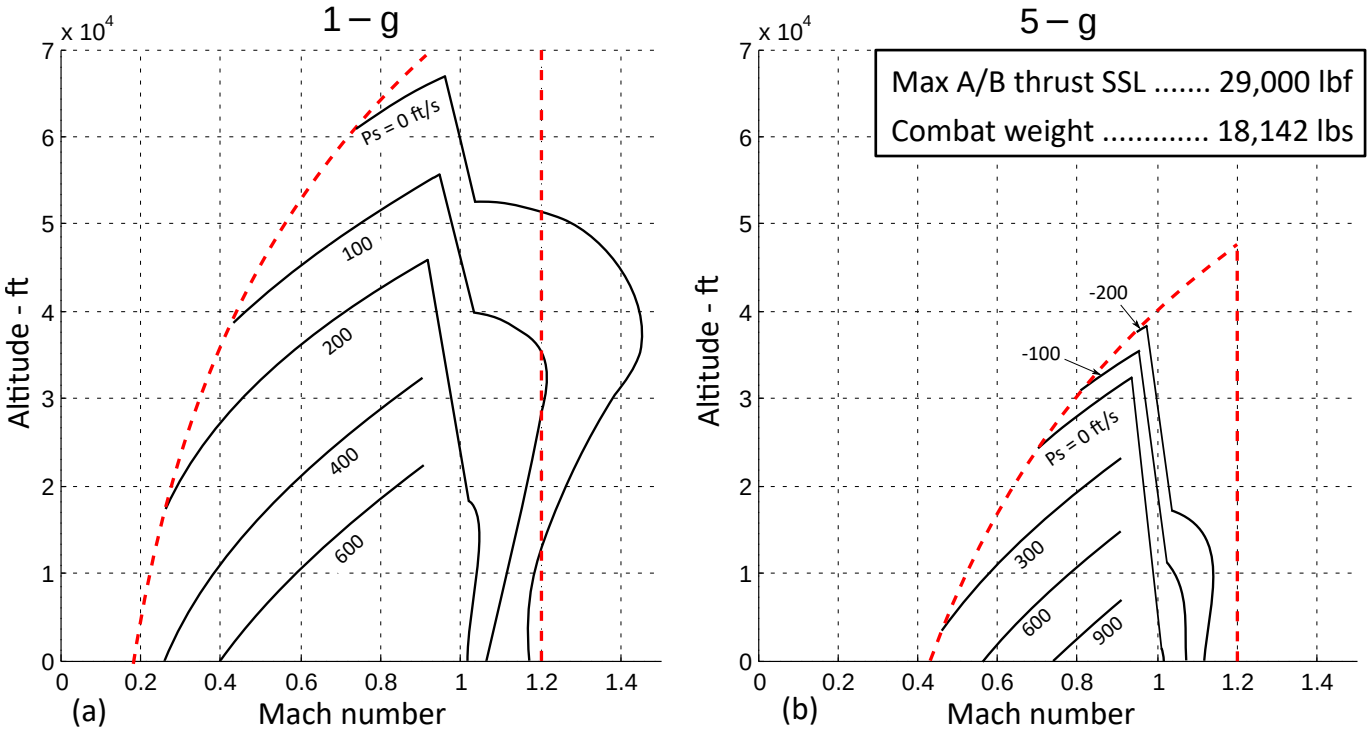

Figure 37: Specific excess power envelope at 1 and 5 - g, 50 % fuel weight and maximum afterburner thrust.

10.2 Climb & ceiling

Another major measure of merit of the aircraft is how it performs in climb. Denoting the climb angle (angle with the horizon) by γ, the force balance of the aircraft writes:

$$\begin{aligned} L &= W\cos\gamma, \\ T &= D + W\sin\gamma \Rightarrow \gamma = \arcsin\left(\frac{T-D}{W}\right). \end{aligned} \tag{10.3}$$

The total drag force may be evaluated with the drag polar of the aircraft. As the lift coefficient depends on the angle of climb itself, it is necessary to iterate for γ. The rate of climb is then simply equal to:

$$V_z = V\sin\gamma, \tag{10.4}$$

where V is the airspeed.

A convenient way to summarise climb performance of the aircraft is to draw a map of the rate of climb as a function of the altitude and Mach number, as depicted in Fig. 38. The map is bounded by the aerodynamic and thrust limits ($P_s = 0$). Notice once more the significant drop in rate of climb when reaching supersonic conditions. There exist a region below 10,000 [ft] approximately where the available maximum thrust is larger than the weight of the aircraft itself: the climb is vertical.

Fig. 38 may also be used to assess the surface ceiling of the aircraft. For jets it is defined as the altitude at which the maximum rate of climb goes below 500 [ft/min] or 8.33 [ft/s]. Since the results presented here are not reliable in the vicinity of 1.0 M, the service ceiling is evaluated at 0.8 M and is equal to:

$$h_{ceiling} = 61,000\ [ft] \quad \text{approximately.} \tag{10.5}$$

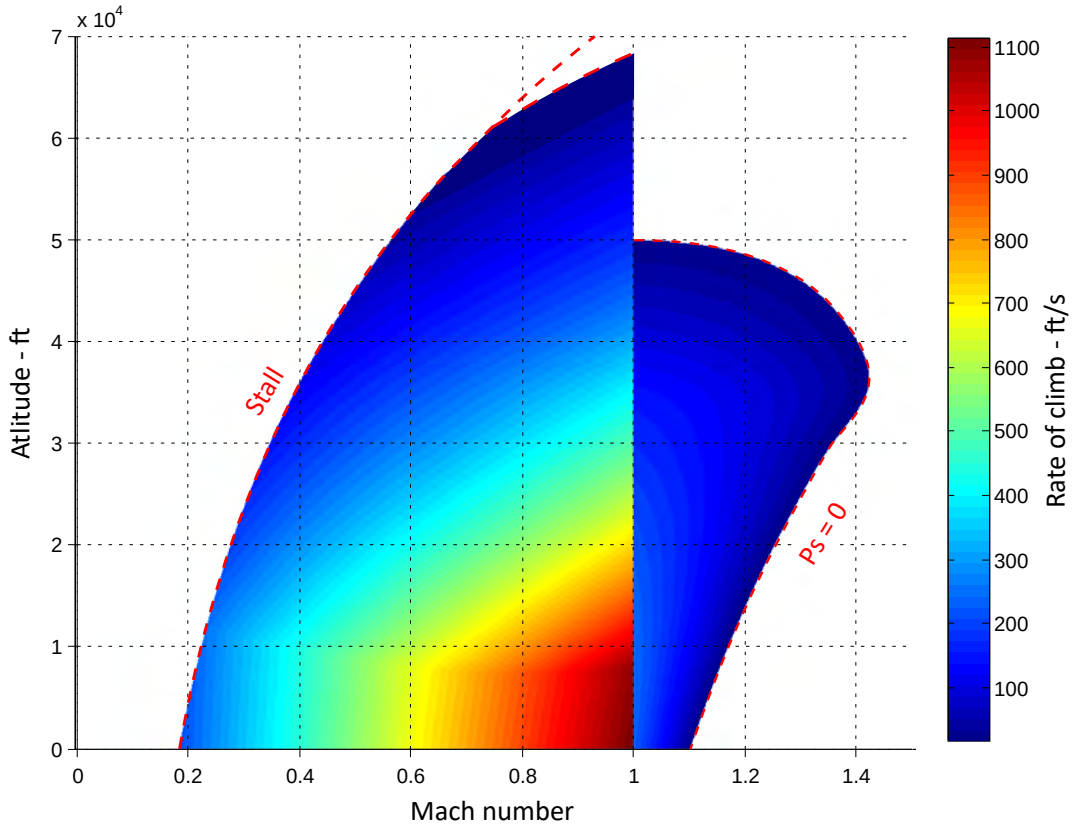

Figure 38: Map of the rate of climb as a function of the altitude and Mach number at 50 % fuel weight and maximum afterburner thrust.

It should be stressed that the diagrams presented here all seem rather optimistic. It should be kept in mind that they resulted from many approximations: point mass force equilibrium, approximate thrust correction for altitude and Mach number, approximate drag polars, etc.
Utlimately, only in flight measurements may bring a reliable performance assessment.

10.3 Minimum runway length

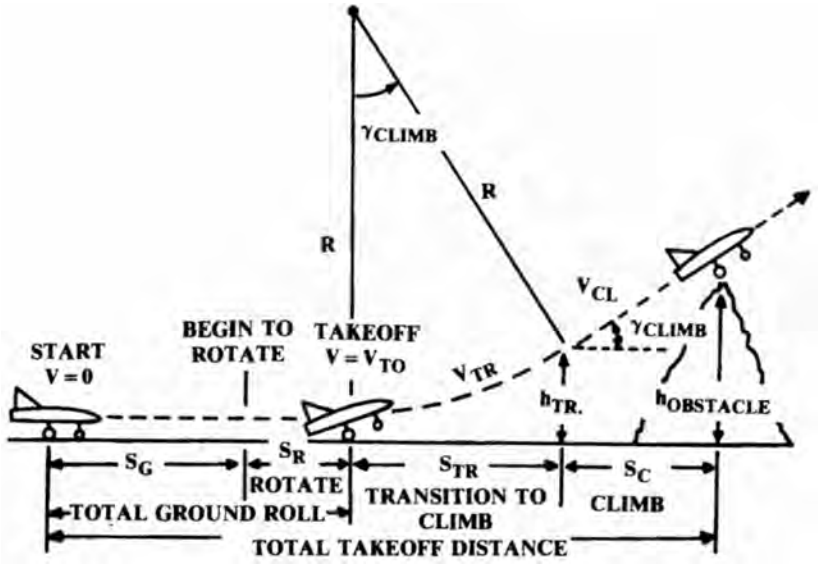

Figure 39: Schematic division of take-off into a ground roll, a transition and a climb.[16]

Take-off The take-off analysis can be divided in segments, as shown in Fig. 39. The total take-off distance is composed by the ground roll, the transition to climb and the climb itself.

During the ground roll, the plane is subjected to forces coming from the thrust, the drag and the rolling friction of the wheels. The value taken for the rolling resistance correspond to the case of highest resistance (wet concrete) (given in the tabular [16], chapter 17, page 486). The acceleration of the plane can be expressed in terms of the aerodynamic coefficients, calculated when the flaps are in take-off position (deflection angle of 30 degrees).

The ground roll distance is then obtained via integration of the velocity divided by the acceleration. The initial velocity is of course zero and the final velocity (V_{TO}) is equal to 1.1 times the stall speed. The thrust used for the calculations is an average, since it can vary during the ground roll. Because the integration has been done with respect to the velocity squared, one can choose to take as an average the thrust at about 70 % of V_{TO} ([16], chapter 17, page 487).

The plane will then spend 1 second nose up, still on the ground. The distance covered by the aircraft is easily calculated knowing that the aircraft is at V_{TO}. In the transition phase, the aircraft accelerates to reach the climb speed, equal to 1.2 V_{stall}. Because the initial velocity is 1.1 V_{stall}, the average velocity taken for the calculations is then 1.15 V_{stall}. The transition trajectory is a circular arc, coming from the load factor equal to 1 and the centripetal acceleration. Take-off is completed once the aircraft reaches the required obstacle clearance which amounts to 50 [ft] for trainers. This height is cleared before the end of the transition segment.

The distance as well as the fuel consumption associated to each step may then readily be computed.

Landing Landing contains quite the same steps than take-off, but backwards. The trainer first approaches, then flares before rolling on the ground. Those 3 steps determine the landing distance. The approach phase begins when the plane gets an obstacle clearance over a 50-ft object. The approach speed for a fighter is 1.2 V_{stall}. The steepest angle at which the aircraft approaches is calculated with full flaps deflection (60 degrees) and idle thrust. The latter is 0.4 times the cruise thrust, known as the "minimum" thrust. The approach distance is finally calculated knowing the flare height.
The aircraft touches the ground at a speed equal to 1.1 V_{stall} (V_{TD}), so the aircraft has to decelerate in order to reach this velocity. To do so, a flare distance is computed using the average flare velocity, 1.15 V_{stall} (because the initial speed is the approach speed).
The radius of the flare circular arc is found in the same way as for the transition phase. The flare height and the distance covered during flare can then be calculated. The ground roll is divided in two parts. The aircraft first rolls free on the ground for approximately 2 seconds and then brakes. The free roll distance is easily found taking the V_{TD}. The braking distance is found by taking the same loads as for the ground roll at takeoff, but with an initial velocity equal to V_{TD} and a final velocity equal to zero. The rolling resistance is here taken for the critical case of icy concrete (given by the table in ([16], chapter 17, page 486)).

The distances associated to each step of the take-off and the landing procedures are compiled in Tab. 30 and 31 respectively.
As the Coyote is a one-engine aircraft, the minimum runway length requirement may be approximated by adding take-off and landing distances together:

$$\text{Minimum runway length:} \qquad 4800 \text{ [ft]}, \tag{10.6}$$

which clearly complies with the objective of 6000 [ft].

Step	Take-off segment	Distance [ft]
1	Ground roll	800
2	"Nose up"	264
3	Transition	599
Total		1663

Table 30: Take-off distances corresponding to each segment.

Step	Landing segment	Distance [ft]
1	Approach	129
2	Flare	317
3	Free roll	378
4	Brake	2267
Total		3091

Table 31: Landing distances corresponding to each segment.

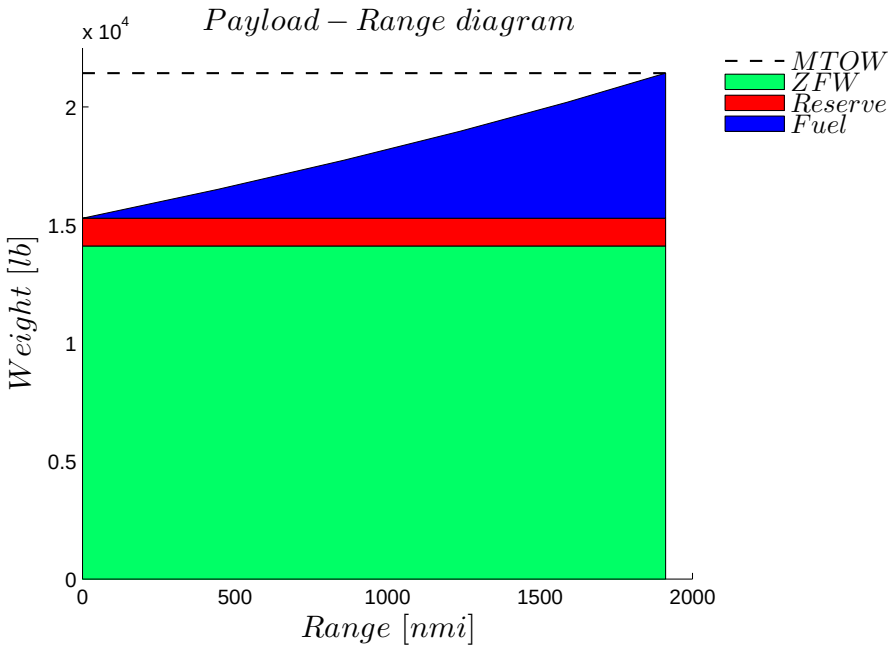

Figure 40: Range diagram in cruise conditions (M=0,8 and 35,000 [ft]).

10.4 Range

The payload-range diagram illustrates the trade-off relationship between the payload and the range of the aircraft. It is given in Fig. 40. The green part represents the sum of the manufacturer empty weight and the payload of 1000 [lb] given in the request for proposal, assumed here retained throughout the mission. The red part is the additional weight of the reserve of fuel. Finally, the blue is the weight of fuel, which allows to compute the range with Breguet range equation :

$$Range = \frac{L}{D}\,\frac{V}{SFC}\,\ln\left(\frac{W_i}{W_f}\right), \tag{10.7}$$

with $\frac{L}{D}$ the lift to drag coefficient, V the velocity, W_i and W_f the initial and final weight of the aircraft.

Here, the $MTOW$ achieved corresponds to the weight of the aircraft when its tanks are full of fuel, i.e. no additional weight can be added. Therefore, the maximal distance the Coyote can reach in cruise is given by the diagram and is about 3541 [km] or 1912 [nmi].

10.5 Compliance with the objectives

Tab. 32 compiles the performance characteristics of the Coyote and compares them to the objectives. One may notice that it does comply with every objective, with a comfortable margin that should cover for the unavoidable uncertainties associated to a preliminary design.

	Coyote	Threshold	Objective
Sustained g at 15 000 [ft] - max A/B			
$P_s = 0$ [ft/s]	8	-	-
$P_s = -200$ [ft/s]	9	8	9
Sustained g at 15 000 [ft] - no A/B			
$P_s = 0$ [ft/s]	6	-	6 (set by the team)
$P_s = -200$ [ft/s]	7	-	-
Shortest turning radius [ft] - full A/B	2,300	-	-
Minimum Runway Length [ft] - no A/B	4,800	8,000	6,000
Payload [lb]	1000	500	1,000
Range (Unrefueled) [nmi]	1,900	1,000	1,500
Max. climb rates [ft/min] - full A/B			
SL	54,000	-	-
15,000 [ft]	42,000	-	-
35,000 [ft]	21,000	-	-
Service ceiling [ft] - full A/B	61,000	40,000	50,000
Cruise Speed	0.8 M	0.7 M	0.8 M
Maximum Speed - full A/B (thrust limit)	1.5 M	-	-
Dash speed	1.2 M	0.95 M	1.2 M

Table 32: Comparison of the main performance characteristics with the design objectives.

11 Trade-off study

The purpose of the trade-off studies is to show that the retained configuration is optimal by varying some of the main parameters by 10 %. The characteristics of the trainer are then reassessed and compared to those of the retained configuration, called the *reference*, in Tab. 33.
It has been decided to vary the following parameters: the wing surface, the wing aspect ratio and the length of the fuselage. Additionally, a configuration with a smaller engine is also studied.

Length of the fuselage On the one hand, increasing the length of the fuselage improves the manoeuvrability of the trainer through an increase in V_T. It comes with the price of a slight increment in empty weight and fuel weight. Consequently, for the same wings area, the trainer must fly at higher $C_{l,w}$, bringing it closer to stall and increasing drag. Additionally, the increment in weight lowers the maximum g that the trainer can sustain continuously during maneuvres. Another factor that is not depicted in the table is that additional volume inside the fuselage can be dedicated to fuel storage.
Since the intensity of the manoeuvres that the trainer can perform is one of the main measure of merit of the design, increasing the length of the fuselage is not considered as an option.
On the other hand, a shorter fuselage allows to decrease the empty weight and fuel weight. This implies a slight increment in the maximum g sustained during maneuvres, which is attractive. The manoeuvrability of the trainer is however lowered. An additional drawback is that the volume inside the fuselage is no longer sufficient to store the fuel required for the mission. Consequently, an increase in the fuselage width must be considered, impacting on both the weight and the drag of the trainer. In the end, this would probably negate a good part of the gain in maximum sustained g discussed earlier. For these two reasons, the reference configuration is retained.

Smaller engine: the F414-GE-400 Selecting a smaller engine is motivated by the hope that the reduction in empty weight and fuel weight may compensate the decrease in thrust that the engine can deliver. The F414-400 from General Electrics delivers about 25 % less (military) thrust than the F100-229 from Pratt & Whitney selected for the trainer, but is about 35 % lighter. It benefits thus from a higher thrust-to-weight ratio. The configuration depicted in Tab. 33 was achieved by targeting a minimum overall mass (smaller wings and shorter fuselage). This results in a significant decrease in empty weight and fuel weight. The C.o.G. is also less aft than in the reference configuration (because of the lighter engine), improving on V_T. The reduction in weight comes however with a moderate hit to the maximum g sustained during manoeuvres at constant speed. Selecting this engine could thus be a cheaper and lighter alternative to the current design, with a moderate performance reduction. Since the performance are a major measure of merit of the design, the F100 is preferred.

Area of the wing Increasing the wing area by 10 % results in an overproduction of lift if one keeps the same $C_{L,w}$ as in the reference configuration. Therefore, one is allowed to reduce the A.o.A which will also decrease the drag. This leads to a reduction of the fuel consumed by the engine since it has to produce less thrust. However, increasing the wing area has some important drawbacks: it increases the structural weight of the aircraft and mostly, it reduces the manoeuvrability (as it can be seen with the decrease in V_T) and the maximum g the trainer can sustain continuously during manoeuvres.
On the other hand, a smaller wing reduces the weight of the aircraft and of the fuel. With a smaller span, the trainers gains in manoeuvrability and sustains more g in manoeuvres. However, the $C_{L,w}$ needs to be increased drastically and thus, the trainers is more prone to stall. In conclusion, the surface area of the reference configuration is held.

Aspect ratio of the wing By increasing the AR, one can see that the trainer gains in manoeuvrability, which is attractive, and can withstand higher g in manoeuvres. Moreover, the $C_{L,w}$ is reduced which is also another great argument in the balance. However, the wing's span must be increased, impinging on the stiffness of the wing. Knowing that the trainer must sustain high g manoeuvres, high AR wings should be avoided.
The other possibility is to reduce the AR but this is not an option since manoeuvrability and sustained g will both be reduced. The A.o.A. should also be increased but this is not of interest. To conclude, there is no great improvements earned by changing the AR, and thus, the one of the reference configuration is maintained.

	Reference	l_{fus} +10 %	l_{fus} -10 %	F414-GE	S +10 %	S -10 %	AR +10 %	AR -10 %
W_0 [lb]	14,357	+1.2	−1.5	−19.4	+2.2	−4.4	−0.6	−1.9
W_{fuel} [lb]	8,267	+0.3	−2.0	−21.2	−0.45	−4.9	−3	−2.3
$C_{L,w}$	4.1	+2.4	-	-	−4.9	+12.2	−2.4	+7.3
V_T	0.608	+9.0	−9.0	+4.3	−2.82	+1.6	+0.17	−1.5
Sustained g	6.0	−0.9	+1.7	−7.0	-8.6	+1.7	+0.17	−8.6

Table 33: Comparison between 7 trade-off configurations and the configuration selected for the trainer (called reference here) in terms of some main characteristics. Note that the differences are given in %!

12 Cost estimates

Once the main features of the aircraft are determined, a cost analysis must be carried out in order to determine whether the Coyote is competitive in the market. The latter will consist in three different parts:

- the non-recurring development and production costs, consisting in engineering, production tooling, labor and the testing part,
- the recurring production costs, representing the average incremental cost for an additional aircraft,
- the operation and maintenance costs, giving the direct operating cost per flight hour.

The methodology followed here to estimate these costs is the RAND DAPCA IV Model, which is the latest version of the Development and Procurement Costs of Aircraft (DAPCA) model. It provides cost estimating relationships via analyses using curve-fit programs of the cost data of numerous aircraft. The quantity of produced aircraft will be fixed to 100.

12.1 Non-recurring costs

The non-recurring costs (NRE) can be divided in two parts: the development NRE which is a fixed cost, representing the flight tests and development support costs, and the production NRE, which depends on the number of aircraft produced and contains the production tooling and engineering effort.

Flight-test cost A number of eight aircraft will be built for test purposes, and the cost of these tests include planning, instrumentation, flight operations, engineering and manufacturing support of flight testing.
It is given by the equation:

$$C_F = 2498 W_e^{0.325} V^{0.822} FTA^{1.21} 1.32 = 213\ 318\ 300 \text{ USD}, \tag{12.1}$$

with W_e the empty weight equals 12 807 [lbs](from Fig. 4), V the maximum velocity equals 793 knots, and FTA is the number of flight test aicraft (8). Since the coefficients of this equation were determined for a 2012 dollar, an inflation of 1.32 is considered for conversion to 2018 dollars.

Development support cost The development support cost represents all the expenses of the management and marketing posts. This is represented by the equation (11.2):

$$C_D = 91.3 W_e^{0.630} V^{1.3} 1.32 = 274\ 026\ 000 \text{ USD}. \tag{12.2}$$

Tooling production This cost takes into account the design and manufacturing of the tools used for the Coyote. First, the tooling man-hours are computed:

$$H_T = 5.99 W_e^{0.777} V^{0.696} Q^{0.236} = 3\ 256\ 900 \text{ man-hours}. \tag{12.3}$$

These hours are then multiplied by the appropriate hourly rates in order to calculate the labour costs. The tooling wrap rate is given by M.Raymer[16] with a value of 118 USD. After applying an inflation of 1.32, it is converted to the value of 151.8 USD.

Engineering effort The engineering hours contains mainly the airframe development and the system engineering. Those are given by the following equation :

$$H_e = 4.86 W_e^{0.777} V^{0.894} Q^{0.136} = 6\ 252\ 800 \text{ man-hours}. \tag{12.4}$$

The engineering wrap rate is 155.76 USD with the inflation.

12.2 Recurring costs

The recurring cost represents the average incremental cost for an additional aircraft. It is composed of the manufacturing, the quality control, the engine and the avionic cost. This is a production cost.

Manufacturing labor It represents the fabrication and assembly of the aircraft. The manufacturing hours are given by the equation

$$H_M = 7.37 W_e^{0.82} V^{0.484} Q^{0.641} = 8\ 333\ 400 \text{ man-hours}. \tag{12.5}$$

The manufacturing wrap rate is of 129.36 in 2018 USD.

Quality control An important aspect of the production is the quality control. The tools as well as the aircraft have to be checked in order to ensure the quality standards are met (both for safety and performance). The hours depends on the manufacturing hours and follow the equation:

$$H_Q = 0.133 H_M = 1\ 108\ 300 \text{ man-hours}. \tag{12.6}$$

The quality control hourly rate is 142.56 USD.

Manufacturing materials cost This cost includes the structural raw cost (mostly aluminium) plus the different hydraulic, electrical and pneumatic systems. The equation (11.7) gives the cost in 2018 USD.

$$C_M = 31.2 W_e^{0.921} V^{0.621} Q^{0.799} 1.32 = 625\ 368\ 800 \text{ USD}. \tag{12.7}$$

Engine cost In the absence of known price about the engine, the equation (11.8) is given[16] to estimate the unit price.

$$C_{eng} = 3112\,(0.043\ T_{max} + 243.25\ M_{max} + 0.969\ T_{turbine,inlet} - 2228)\,1.32 = 2\ 593\ 500 \text{ USD}. \tag{12.8}$$

Avionics cost The cost of the avionics is given in the request for proposal and amounts to 937200 USD per unit.

12.3 Operations and maintenance costs

The operations and maintenance costs describe the hourly cost of the Coyote for the design mission. Its represents the fuel and oil costs as well as the maintenance expenses.

Fuel and oil costs The average fuel burned per hour is simply computed with the mission duration and total fuel burned, as done in the following equation:

$$\text{Fuel consumption per hour} = \frac{8299.33}{2.0019} = 4\ 145.55 \text{ [lb/h]}. \tag{12.9}$$

This value is then multiplied by the current fuel price, which is of 0.562 [USD/lb][1]. This finally gives a fuel cost per hour of 2333.42 [USD/h] The oil cost represents less than 1% of the fuel cost and is here neglected.

Maintenance expenses The maintenance man-hours per hour of flight depend on the type of aircraft, and its value for a jet trainer is 6 to 10 [16]. The maintenance labour cost can then be obtained by multiplying it by the corresponding wrap rate, but the latter could not be found in the literature. As an approximation, the manufacturing wrap-rate mentioned earlier is here used.

$$\text{Maintenance cost per hour} = 6 \cdot 129.36 = 776.16 \text{ [USD/h]}. \tag{12.10}$$

The total cost per hour is then estimated as $776.16 + 4145.55 = 4921.71$ [USD/h]

12.4 Detailed cost and unit price

The non-recurring costs estimate is described in Tab. 34. The total production cost for 100 aircraft is then described in Tab. 35.

Flight test	213.32 M$
Devel. support	274.025 M$
Tooling production	507.298 M$
Engineering	949.171 M$
Total NRE cost	1 943.8 M$

Table 34: Details of the NRE costs.

Manufacturing	1 078.009 M$
Quality control	119.701 M$
Manufacturing materials	625.368 M$
Engine	259.35 M$
Avionics	93.72 M$
Total production cost	2 173.098 M$
Unit cost	21.73 M$

Table 35: Details of the recurring costs.

The total NRE cost exceeds the threshold of 1 B$ and the unit price is slightly higher that the threshold of 20 M$. Note that these cost approximations are likely overestimated since components such as avionics or the engine are considered bought one buy one. Buying in bulk could significantly lower the aircraft production price. In addition, the price lowers with the number of aircraft produced because of the "learning curve", as shown in Fig. 41.

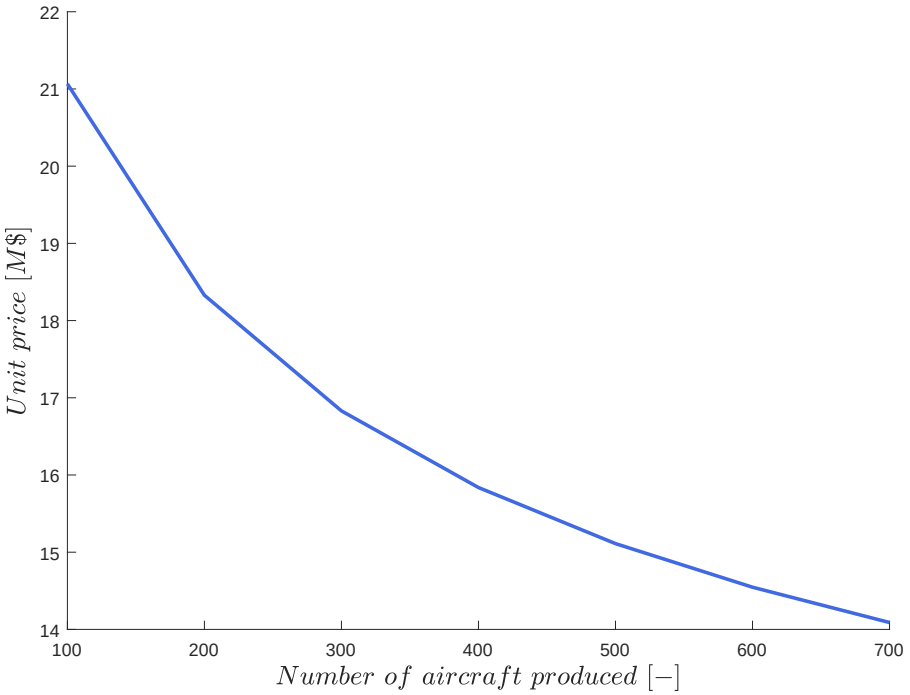

Figure 41: Unit cost in M$ for a production of 100 to 700 units.

13 Conclusion

In answer to the request for proposal issued by the U.S.A.F. about the introduction of a new pilot training aircraft, the preliminary design of the Coyote, a V-tail trainer has been carried out.
To begin with, the design objectives in terms of performance and the mission have been described. Then, a general configuration was selected based on qualitative discussion of different alternatives. The highly iterative design process of the main components has then been described and the methodology clearly defined. Interactions between each aspects of the design have been highlighted. In early stages of the project, empirical relations have been used extensively to provide first approximations. In later stages, detailed analyses have been carried out with more advanced tools. In particular, the subsonic and supersonic aerodynamics of the Coyote have been studied with a full potential flow solver, finite elements analyses of the internal structures have been conducted and the handling qualities have been evaluated with the DATCOM method. The cost associated to the development and the production of the Coyote have also been evaluated. Finally, a preliminary performance assessment has been conducted. Finally, a brief trade-off study has been carried out by varying the main parameters of the design by 10 % to ensure the selected configuration is optimal.
The final design of the Coyote has proven to meet all the performance objective with a comfortable margin.

Appendix A

1 Aesthetic views

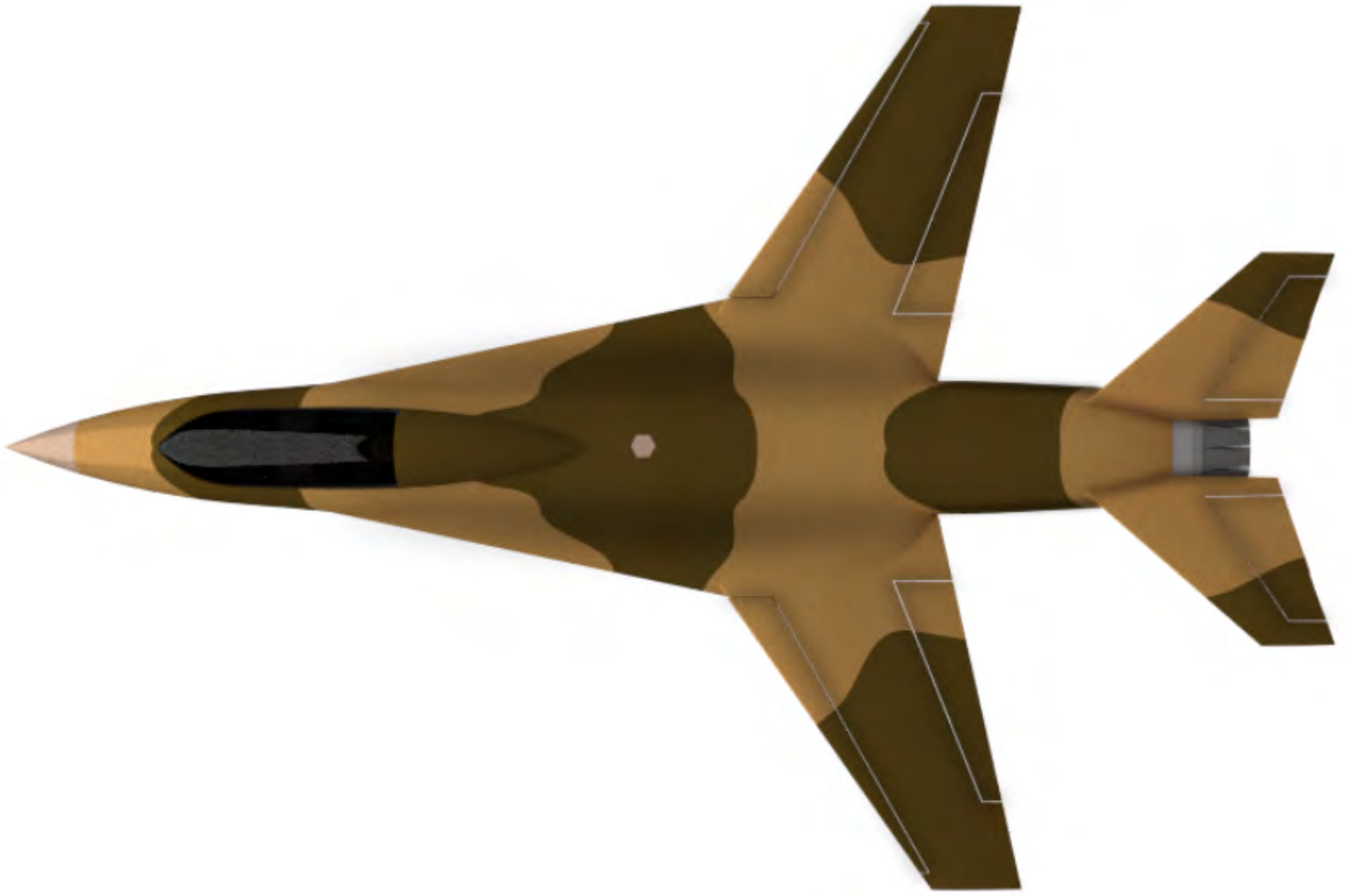

Figure A.1: Top view of the Coyote.

Figure A.2: Side view of the Coyote.

Figure A.3: Front view of the Coyote.

Figure A.4: Global view of the Coyote with the refuel hookup and the cockpit access ladder.

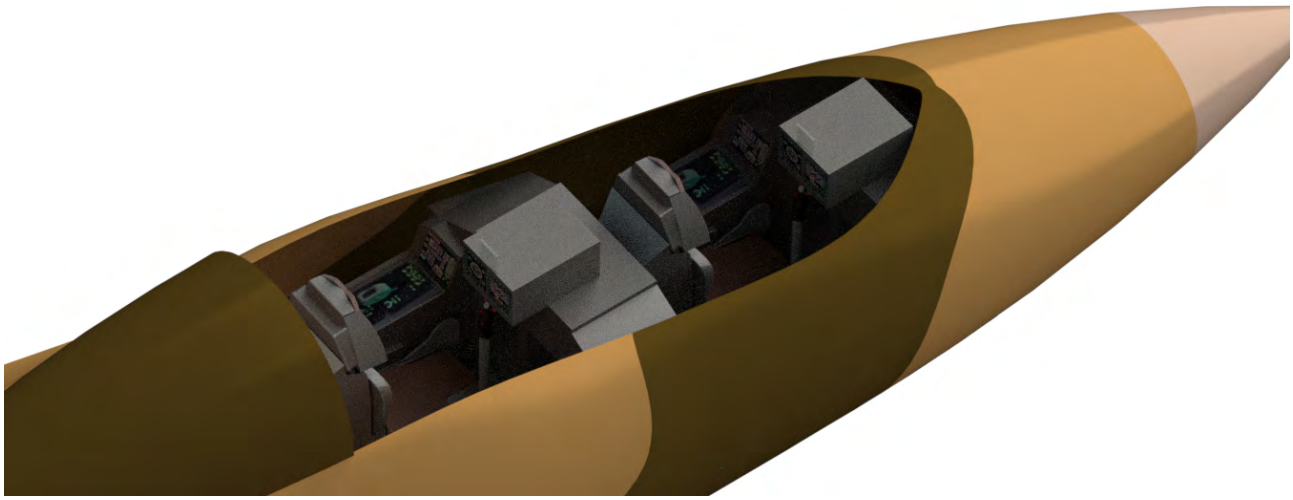

Figure A.5: Details of the cockpit.

Figure A.6

Figure A.7

Figure A.8

Figure A.9

2 Additional figures

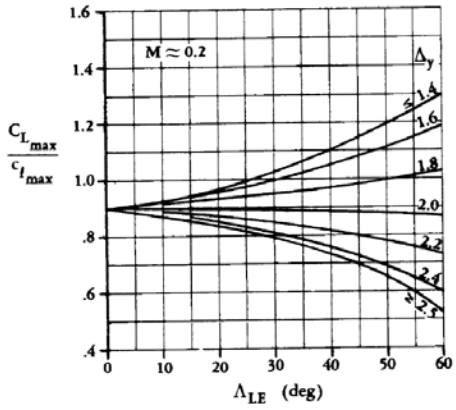

Figure A.10: The $\frac{C_{L_{max}}}{C_{l_{max}}}$ ratio with respect to the leading edge sweep angle for several sharpness parameters.

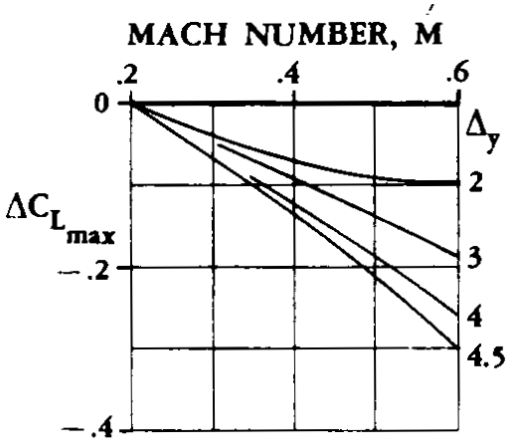

Figure A.11: The $\Delta_{L_{max}}$ with respect to the Mach number for different sharpness parameters (from [16]).

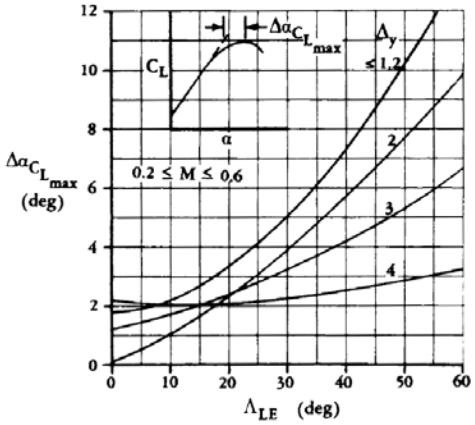

Figure A.12: $\Delta_{C_{L_{max}}}$ with respect to the sweep angle of the leading edge for different sharpness parameters at speeds between M0.2 and M0.6 (from [16]).

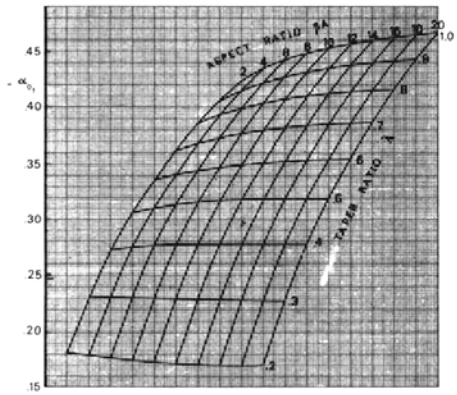

Figure A.13: Zero-lift A.o.A. increment per unit of twist for straight wings (from [17]).

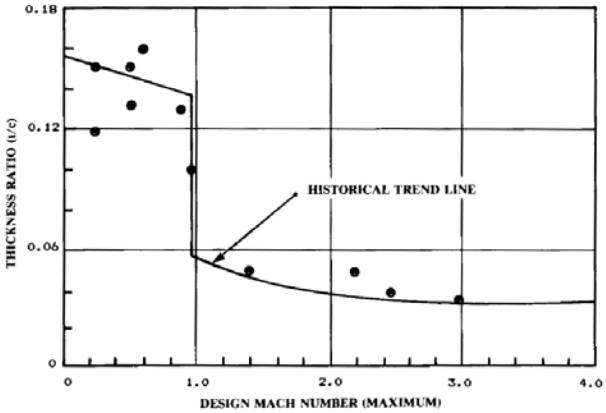

Figure A.14: Thickness ratio historical trend with respect to the maximum design Mach number.

3 Summary table

Parameter	SI	US/Imp
Fuselage		
Height: **Height**$_{fus}$	1.7 [m]	5.6 [ft]
Width: **Width**$_{fus}$	1.7 [m]	5.6 [ft]
Length: **Lenght**$_{fus}$	15.4 [m]	49.2 [ft]
A.o.A. of the fuselage at 100 [%] of fuel	1 [°]	
Wing		
Span: b_w	10.6 [m]	34.8 [ft]
Aspect Ratio: AR_w	4.5	

Surface: **S**	25 [m^2]	269 [ft^2]
Taper Ratio: λ_w	0.3	
Chord at root: C_{root_w}	3.6 [m]	11.9 [ft]
Chord at tip: C_{tip_w}	1.1 [m]	3.6 [ft]
Sweep angle LE: Λ_{LE}	35 [°]	
Sweep angle at 1/4 chord: $\Lambda_{1/4}$	30.14 [°]	
Geometric twist: ϵ_{gtip}	-2 [°]	
Mean Aerodynamic Chord: **MAC**	2.58 [m]	8.46 [ft]
X coordinate of the Aerodynamic center: $\mathbf{X}_{ac}$	0.82 [m]	2.69 [ft]
Y coordinate of the Aerodynamic center: $\mathbf{Y}_{ac}$	2.18 [m]	7.15 [ft]
Compressibility parameter: β	0.6	
Cruise Mach number: M_{cruise}	0.8	
Cruise altitude: H_{cruise}	11 10^3 [m]	36000 [ft]
Reynolds number at the MAC at M0.8 at 35000 [ft]: **Re**	4.9494 10^6	
Fuel volume: $\mathbf{V}_{fuel}$	0.5 [m^3]	135 [gal]
Wetted surface: $\mathbf{S}_{wet_W}$	50.28 [m^2]	541.18 [ft^2]
Wing lift coefficient in cruise at 50 [%] of fuel: C_{L_W}	0.1886	
Wing lift curve slope at M0.8: C_{L_α}	4.776 [1/rad]	
Incidence angle: i_w	3 [°]	
A.o.A. at root (cruise) at 100 [%] of fuel: α_{root}	4 [°]	
Zero-lift A.o.A. at root (wing): $\alpha_{L,0}$	-1.17 [°]	
Local aerodynamic twist: $\epsilon_{a_{tip}}$	-0.23	
Maximum lift coefficient (flaps in) at M0.3: $\mathbf{C}_{L_{max}}$	0.94	
Airfoil thickness ratio: $\mathbf{t/c}_w$	0.06	
Airfoil Zero-lift A.o.A.: $\alpha_{l,0}$	-1.6 [°]	
Airfoil lift curve slope at M0.8: C_{l_α}	0.1710 [1/°]	
Maximum camber (situated at 50 [%] of the chord): $\mathbf{camb}_{max}$	1.1 [%]	

Stability

Plane lift coefficient (cruise - full weight): C_L	0.36	
Empennage lift coefficient (cruise - full weight): C_{L_T}	-0.13	
Surface of empennage: S_T	10.58 [m^2]	107.6 [ft^2]
Fuselage A.o.A. (cruise - full weight): α_{fus}	1 [°]	
Fuselage zero-lift A.o.A.: $\alpha_{fus,0}$	-4.1 [°]	

Non-dimensional centre of gravity position (full weight): h_{CG}	0.25	
Non-dimensional aerodynamic centre position (cruise - full weight): h_{AC}	0.27	
Incidence angle of the wing on the fuselage: i_w	3 [°]	
Plane lift coefficient slope (cruise): $C_{L_{plane_\alpha}}$	4.71 [rad$^-$1]	
Empennage A.o.A. (cruise - full weight): α_T	-3.5 [°]	
Downwash (cruise - full weight): E_{ps}	2.8 [°]	
Vertical distance between wing and empennage: **m**	0.6 [m]	1.97 [ft]
Incidence angle of the empennage on the fuselage: i_T	-1.3 [°]	
V-Tail		
Span (2 fins): b_T	5.82 [m]	19.10 [ft]
Aspect Ratio: AR_T	3.2	
Taper ratio: λ_T	0.3	
Sweep angle at LE: Λ_{LE_T}	40 [°]	
Chord at root: C_{root_T}	2.80 [m]	9.18 [ft]
Chord at tip: C_{tip_T}	0.84 [m]	2.75 [ft]
Dihedral angle: Γ_T	40 [°]	
Surface: S_T	10.6 [m^2]	113.9 [ft^2]
V-Tail lift coefficient in cruise at 50 [%] of fuel: C_{L_T}	-0.1278	
V-Tail lift curve slope at M0.8: $C_{L_{\alpha_T}}$	2.38 [1/rad]	
Moment arm of the tail: l_T	4.36 [m]	14.30 [ft]
Airfoil thickness ratio: t/c_t	0.06	
Airfoil Zero-lift A.o.A.: $\alpha_{l,0}$	0 [°]	
Drag		
Drag (cruise - 50 % fuel): **D**	36,800 [N]	8100 [lbf]
Drag coefficient (cruise - 50 % fuel): C_D	0.028	
Zero-lift drag coefficient (cruise): C_{D_0}	0.0063	
e-factor (cruise): **e**	0.63	
Engine		
Military thrust:	79,000 [N]	17,800 [lbf]
Max A/B thrust:	129,700 [N]	29,160 [lbf]
Cruise thrust:	8,690 [N]	1,950 [lbf]
Weight		

Wing: W_w	1,007 [kg]	2,222 [lb]
Ultimate load factor: n_{ult}	13.5	
Limit load factor: n_{lim}	9	
Fuselage weight: W_{fus}	955 [kg]	2,105 [lb]
Gear weight: W_{gear}	508 [kg]	1,120 [lb]
Propulsion dry weight: W_{prop}	1,737 [kg]	3,830 [lbs]
Payload: $W_{payload}$	453.6 [kg]	1000 [lbs]
Fuel weight at TO: $W_{F_{TO}}$	3765 [kg]	8300 [lbs]
Fuel weight at landing: $W_{F_{land}}$	241 [kg]	531 [lbs]
Zero-fuel weight: W_{ZF}	6520 [kg]	14,370 [lbs]
TO weight: W_{TO}	10,260 [kg]	22,624 [lbs]
Wing loading (100 % fuel): W/S	4026 [N/m^2]	84.1 [lbs/ft^2]
Thrust to weight (full A/B and 100 % fuel): T/W	1.28	
Fuel ratio: W_F/W_{TO}	0.377	
Range at maximum payload: d_{PayMax}	3520 [km]	1900 [nmi]

Landing gear

Maximum pitch angle: θ_{max}	15 [°]	
Maximum roll angle: ϕ_{max}	25 [°]	
Height of the wing: H_w	1.7 [m]	5.6 [ft]
Wheel base: W_{base}	5.24 [m]	17.2 [ft]
Wheel track: W_{track}	1.7 [m]	5.6 [ft]
Lift-off speed: V_{TO}	84.0 [m/s]	163.3 [knots]
Distance between aft C.o.G. and aft landing gear: l_m	0.42 [m]	1.38 [ft]
Plane gravity centre height (100 % fuel): Z_{CG}	2.13 [m]	6.99 [ft]

Bibliography

[1] *Aviation Fuel Prices.* http://www.100ll.com/. Accessed: 2018-04-16.

[2] Bernard N. Daley and Richard S. Dick. *NACA RM-L52G31a. Effect of thickness, camber, and thickness distribution on airfoil characteristics at Mach numbers up to 1.0.* 1952.

[3] Milton D. Van Dyke. *NACA technical note 2670. High-speed subsonic characteristics of 16 NACA 6-series airfoil sections.* 1952.

[4] *General Dynamics F-16 Fighting Falcon.* https://en.wikipedia.org/wiki/General_Dynamics_F-16_Fighting_Falcon. Accessed: 2018-02-11.

[5] S. Gudmundsson. *General Aviation Aircraft Design.* 1st ed. Elsevier, 2014.

[6] Ir. P. Hendrick. "Propulsion aérienne". Lecture notes for students at the Royale Ecole Militaire de Belgique. 2016.

[7] *Introduction to Air Breathing Engines.* https://www.aircraftenginedesign.com/custom.html4.html. Accessed: 2018-02-11.

[8] Albert E. von Doenhoff Ira H. Abbott and Jr. Louis S. Stivers. *NACA Report No 824. Summary of airfoil data.* 1945.

[9] "Low Bypass Turbofan (Pratt & Whitney F100)". https://grabcad.com/library/low-bypass-turbofan-pratt-whitney-f100. Accessed: 2018-04-29.

[10] Georges B. McCullough and Donald E. Gault. *NACA TN-1923. Boundary-layer and stalling characteristics of the NACA 64A006 airfoil section.* 1949.

[11] L. Noels. "Lecture Slides: Conceptual Design". pages 45 and 46. 2017.

[12] L. Noels. "Lecture Slides: Design Examples of Aircraft Structures". page 42. 2017.

[13] *Pratt & Whitney F100.* https://en.wikipedia.org/wiki/Pratt_%26_Whitney_F100. Accessed: 2018-02-11.

[14] R. Princivalle. "Lecture Slides: Propulsion". http://www.ltas-cm3.ulg.ac.be/AERO0023-1/ConceptionAeroPropulsion.pdf. Accessed: 2018-04-12.

[15] Paul E. Purser and John P. Campbell. *NACA Report No 823. Experimental verification of a simplified Vee-tail theory and analysis of available data on complete models with Vee-tails.* 1944.

[16] P. Raymer. *Aircraft Design: A Conceptual Approach.* 2nd ed. American Institute of Aeronautics and Astronautics, 1989.

[17] E. Torenbeek. *Synthesis of subsonic airplane design.* Delft University Press, 1976.